

OKINAWA INSTITUTE OF SCIENCE AND TECHNOLOGY
GRADUATE UNIVERSITY

Thesis submitted for the degree of

Doctor of Philosophy

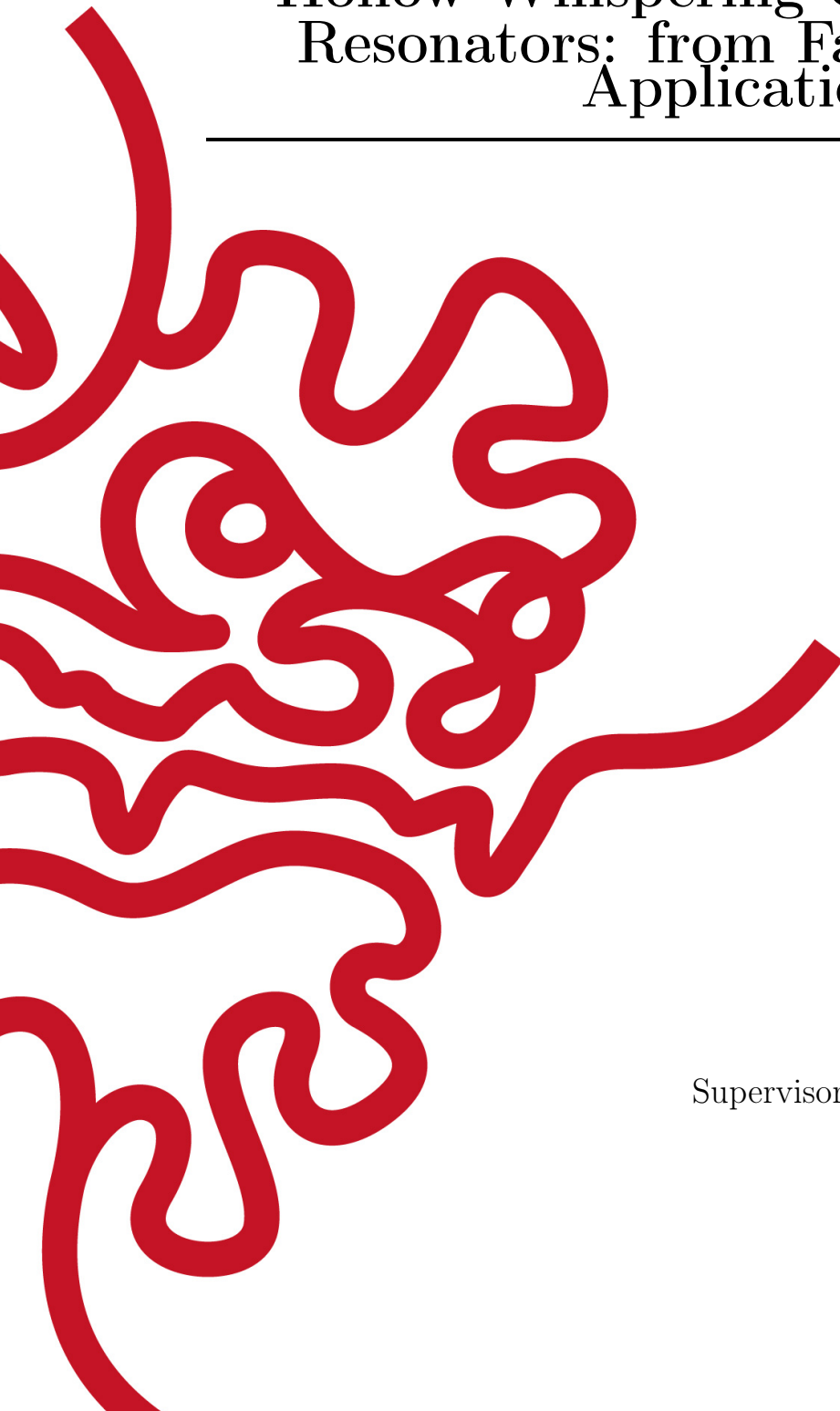
Hollow Whispering Gallery Mode
Resonators: from Fabrication to
Application

by

Sho Kasumie

Supervisor: **Prof. Síle Nic Chormaic**

September, 2019



Declaration of Original and Sole Authorship

I, Sho Kasumie, declare that this thesis entitled *Hollow Whispering Gallery Mode Resonators: from Fabrication to Application* and the data presented in it are original and my own work.

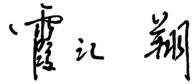
I confirm that:

- No part of this work has previously been submitted for a degree at this or any other university.
- References to the work of others have been clearly acknowledged. Quotations from the work of others have been clearly indicated, and attributed to them.
- In cases where others have contributed to part of this work, such contribution has been clearly acknowledged and distinguished from my own work.
- None of this work has been previously published elsewhere, with the exception of the following:
 - Y. Yang, R. Madugani, S. Kasumie, J. M. Ward, and S. Nic Chormaic, "Cavity ring-up spectroscopy for dissipative and dispersive sensing in a whispering gallery mode resonator", *Appl. Phys. B* **122**, 291 (2016) [77]
 - Y. Yang, R. Madugani, S. Kasumie, J. M. Ward and S. Nic Chormaic "Cavity Ring-Up Spectroscopy for Dissipative and Dispersive Sensing in a Whispering Gallery Mode Resonator" in "Exploring the World with the Laser", D. Meschede, T. Udem and T. Esslinger (eds), Springer, Cham (2018) [165]
 - Y. Yang, F. Lei, S. Kasumie, L. Xu, J. M. Ward, L. Yang and S. Nic Chormaic "Tunable erbium-doped microbubble laser fabricated by sol-gel coating", *Opt. Express* **25**, 1308-1313 (2017) [14]
 - Y. Yang, X. Jiang, S. Kasumie, G. Zhao, L. Xu, J. M. Ward, L. Yang, and S. Nic Chormaic, "Four-wave mixing parametric oscillation and frequency comb generation at visible wavelengths in a silica microbubble resonator", *Opt. Lett.* **41**, 5266-5269 (2016) [173]
 - S. Kasumie, Y. Yang J. M. Ward, and S. Nic Chormaic, "Toward visible frequency comb generation using a hollow WGM resonator", *Rev. Las. Eng.* **46**, 92 (2018) [50]

- S. Kasumie, F. Lei, J. M. Ward, X. Jiang, L. Yang, and S. Nic Chormaic
"Raman laser switching induced by cascaded light scattering", accepted by
Laser & Photonics Reviews, arXiv:1902.02487 (2019)
- J. M. Ward, S. Kasumie, Y. Yang, F. Lei, R. Madugani and S. Nic Chormaic
"Hollow whispering gallery resonators", Laser Resonators, Microresonators,
and Beam Control XX; 1051805 (2018)
- R. Madugani, S. Kasumie, Y. Yang, J. Ward, F. Lei and S. Nic Chormaic
"Whispering gallery resonators for optical sensing", International Confer-
ence on Optical Fiber Sensors; 103231B (2017)

Date: September, 2019

Signature:



Abstract

Whispering gallery mode resonators (WGMRs) are ultrahigh quality optical resonators, where Q-factors higher than 10^7 are easily achieved. They can be used as compact optical sensors, laser sources, and experimental platforms to study optomechanics and nonlinear optics, for example. A type of WGMR with a hollow structure first appeared in the literature in 2010. Such a WGMR is called a microbubble resonator (MBR) named after its geometrical structure. The wall thickness of an MBR is, typically, quite thin and this leads to several interesting properties: (i) the resonant frequency can be tuned by inserting air pressure, (ii) geometrical dispersion is changed from normal bulk WGMRs, and (iii) when the bubble is filled with water (or other liquids), the resonant optical field can be distributed within, and have an interaction with, the liquid core. In this thesis, we discuss the fabrication method for MBRs and their application in a coupled cavity system, as a tunable laser, and for frequency comb generation at near visible wavelengths. In future, transient sensing may be achieved in a liquid core MBR and different patterns of cascaded Raman scattering may be controlled by inserting air pressure into the MBR. Preliminary work on these topics is also included in this dissertation.

Acknowledgments

First of all, I would like to thank all of the unit members in LMI-QT unit, past and present, Aili, Mark, Thomas, Peter, Krishnapriya, Xue, Metin, Aysen, Prescila, Kristofer, Giang, Tridib, Stephy, Rafino, Ratnesh, Cindy, Ivan, Sahar, Vikraman, Georgiy, Jesse, Maki, Theo and Jean-Baptiste, for welcoming me, a difficult person, and helping me all the time through this PhD. The cheerful working space is owing to all of the unit members and Prof. Síle Nic Chormaic to always be tolerant and working hard for unit members, and for me. It is also due to Emi Nakamura, the administrator of our unit, who supported us so we are able to concentrate on our research. I would like to thank Dr. Jonathan Ward, Dr. Fuchuan Lei, Dr. Yong Yang and Dr. Ramgopal Madugani who worked closely with me and gave valuable advice and suggestions all the time.

I also need like to thank members in the Micro/Nano Photonics Laboratory, Department of Electrical and Systems Engineering, Washington University in St. Louis, during my 3-month research visit. Linhua, Steven, Guangming, Weijian, Xiangyi, Dr. Xuefeng Jiang, Prof. Sahin K. Ozdemir and Prof. Lan Yang who welcomed me, technically supported my research and helped me through an unfortunate incident.

Finally, I would like to thank OIST and all the Japanese taxpayers who supported the research funding. My family over Japan, China, USA and New Zealand, friends and a retired professor in Tokyo are also to be thanked for getting me where I am. Also the forest, the ocean, birds, insects, wind and sky, none of them should be missing.

Abbreviations

WGM	whispering gallery mode
WGMR	whispering gallery mode resonator
MBR	microbubble resonator
FFT	fast Fourier transform
FWHM	full width at half maximum
FSR	free spectral range
ZDW	zero dispersion wavelength
GVD	group velocity dispersion
EIT	electromagnetically induced transparency
ATS	Autler-Townes splitting
CRUS	cavity ring-up spectroscopy
TE mode	transverse electric mode
TM mode	transverse magnetic mode
EMI	electromagnetic interference
MIR	mid-infrared
MIR	near-infrared
FWM	four-wave mixing
SRS	stimulated Raman scattering
SBS	stimulated Brillouin scattering
CLS	cascaded light scattering
SHG	second harmonic generation
THG	third harmonic generation
SPM	self-phase modulation
XPM	cross-phase modulation
SFG	sum-frequency generation
DFG	difference-frequency generation
SPDC	spontaneous parametric down conversion
DSO	digital storage oscilloscope
OSA	optical spectrum analyzer
SEM	scanning electron microscopy
BS	beam splitter
FPC	fiber polarization controller
PD	photodetector
TLS	tunable laser source
PR	photoresist
HDMS	Hexamethyldisilazane

BSA bovine serum albumin
cQED cavity quantum electrodynamics

Nomenclature

c	Speed of light ($2.997\,924\,58 \times 10^8$ [m/s])
μ	Permeability
ϵ	Permittivity
\mathbf{E}	3-dimensional electrical field
E	1-dimensional electrical field
\mathbf{B}	Magnetic field
\mathbf{H}	Magnetic field intensity
\mathbf{D}	Electric displacement field
r	Radial distance
λ	Wavelength [m]
k	Wavenumber [rad/m]
f	Frequency of light
ω	Angular frequency of light ($\omega = 2\pi f$)
$\Delta\omega$	Angular frequency detuning
γ	Decay rate [rad/s]
γ_{in}	Intrinsic decay rate
γ_{ex}	External decay rate
κ	Coupling strength [rad/s]
τ	Intracavity lifetime [s]
P	Laser power [J/s]
U	Energy of light field [J]
A, a	Light field amplitude ($[A ^2] = [U]$, $[\gamma A ^2] = [P] = [\text{J/s}]$)
S, s	Input power amplitude ($[S ^2] = [P] = [\text{J/s}]$)
Q	Quality factor
ξ	Susceptibility

Contents

Declaration of Original and Sole Authorship	iii
Abstract	v
Acknowledgments	vii
Abbreviations	ix
Nomenclature	xi
Contents	xiii
List of Figures	xvii
1 Introduction	1
1.1 Whispering Gallery Mode Resonators	1
1.1.1 Hollow Whispering Gallery Mode Resonators	2
1.2 Whispering Gallery Mode Sensors	2
1.2.1 Cavity Ring-Up Spectroscopy Sensing	3
1.2.2 Optical Trapping with Whispering Gallery Mode Resonators . .	5
1.2.3 Microbubble Lasers for Pressure Sensing	8
1.3 Nonlinear Optics with Whispering Gallery Mode Resonators	9
1.3.1 Frequency Comb Generation in a Microbubble Resonator	10
1.3.2 Intrinsic Raman Mode Switching Process with Whispering Gallery Mode Resonators	13
1.4 Motivation	14
2 Wave Theory of Whispering Gallery Mode Cavities	15
2.1 Introduction	15
2.2 Field Distribution in a Microsphere	15
2.2.1 Maxwell's Equations in Spherical Coordinates	16
2.2.2 Characteristic Equation	17
2.2.3 Free Spectral Range (FSR)	19
2.3 Optical Field Distribution in a Microbubble Resonator	19
2.4 Optical Coupling through a Waveguide	21

2.4.1	Transmission Spectrum	22
2.4.2	Q-Factor	22
2.5	Conclusion	23
3	Experimental Methods	25
3.1	Tapered Optical Fiber Coupling System	25
3.1.1	Transmission Spectrum and Q-Factor Measurement	26
3.2	Whispering Gallery Mode Resonators	27
3.2.1	Silica Microspheres and Micropendulums	27
3.2.2	Silica Microbottle and Microbubble Fabrication	28
3.2.3	Microtoroid Fabrication	31
3.3	Conclusion	31
4	Cavity Ring-Up Spectroscopy	33
4.1	Introduction	33
4.2	Coupled-Mode Theory	33
4.2.1	A Simple Model: Large Spectral Broadening Bandwidth	34
4.2.2	Analytical Solution	36
4.2.3	The Mode Mixing Case	40
4.3	Numerical Methods	41
4.4	Experiment	44
4.5	Discussion	50
4.6	Conclusion	51
5	Optical Force Between Coupled Whispering Gallery Mode Resonators	53
5.1	Introduction	53
5.2	Theory of Coupled Resonators	53
5.2.1	Coupled-Mode Induced Transparency	54
5.2.2	Autler-Townes Splitting	55
5.2.3	Intermediate Regime	55
5.3	Optomechanical Spectrum in the Coupled Resonators Structure	55
5.4	Experimental Implementation with an MBR	58
5.5	Conclusion	60
6	Microbubble Lasers for Pressure Sensing	63
6.1	Introduction	63
6.2	Fabrication	63
6.3	Aero-pressure tuning of the MBR laser	64
6.3.1	Experimental Setup	64
6.3.2	Experimental Results	65
6.4	Conclusion	67
7	Frequency Comb Generation in a Microbubble Resonator	69
7.1	Introduction	69
7.2	Theory	69
7.2.1	Four-Wave Mixing	69
7.3	Experiment	72

7.4	Improvement to the Frequency Comb	74
7.5	Conclusion	76
8	Raman Laser Switching Induced by Cascaded Light Scattering	79
8.1	Introduction	79
8.2	Theory	82
8.3	Experiment	85
8.4	Conclusion	87
9	Conclusion	89
A	Appendix A: MATLAB Code for Field Distribution in a Microsphere	91
B	Appendix B: MATLAB Code for Cavity Ring-Up Spectroscopy	99
C	Appendix C: MATLAB code for Raman Switching Model	105
	Bibliography	111

List of Figures

1.1	(a) Input laser frequency is scanned by a laser controller. The laser light couples into the WGM cavity through the evanescent field of a tapered optical fiber. When an optical mode exists, a transmission dip can be seen on a digital storage oscilloscope (DSO). (b) Frequency shift, linewidth broadening, or mode splitting happens when the resonant condition is changed: for example, deformation of the cavity geometry, refractive index change or or perturbation by a nanoparticle.	4
1.2	(a) Two WGM cavities are coupled to each other while the system is coupled to a tapered optical fiber. (b) One cavity could be a microbubble resonator and the other could be a micropendulum resonator. (c) The symmetric supermode is excited, generating an attractive optical force, when the displacement of the two cavities is large. (d) The symmetric supermode is excited, generating a repulsive force, when the displacement of the two cavities is small.	7
1.3	(a) Energy diagram representing hyper-parametric oscillation. Two pump photons are converted to an idler-signal photon pair. (b) The cascaded hyper-parametric oscillation process. (c) Comb lines in the frequency domain. (d) A Fourier transformation of the frequency comb, in the time domain.	11
1.4	The energy diagram of (a) Stokes SRS and (b) anti-Stokes SRS. (a) Stokes SRS is described by $\omega_S = \omega_p - \omega_s$, where ω_p and ω_s are the frequencies of the pump field and Stokes field. The phase-matching condition is not required. (b) In contrast, anti-Stokes SRS is described by $\omega_A = \omega_p + \omega_s$, where ω_A represents the frequency of the anti-Stokes light field. The phase-matching condition must be satisfied between three frequencies.	13

2.1	Resonant modes obtained by solving the characteristic equation in MATLAB (see Appendix A for details). The diameter of the microsphere is $25 \mu\text{m}$ for all plots. (a)-(d): The resonant wavenumber, k_0 , is 4.04×10^6 rad/m, where $n = 1$ and $l = 136$ is decided by the value of k_0 . (e)-(h): $k_0 = 3.99 \times 10^6$ rad/m, $n = 2$ and $l = 127$. The azimuthal mode number, m , can take any integer between $-l$ and l , including 0. The total number of field amplitude maxima is $n \times (l - m + 1) \times m $. The blue lines in (a) and (e) are norms of the corresponding spherical Bessel functions that describe the intracavity field amplitude and the red lines are norms of the corresponding spherical Hankel functions that describe the evanescent field amplitude.	18
2.2	Simulated optical field of an MBR for different conditions. (a) The fundamental optical mode and (b) a higher order optical mode in an MBR. The intracavity and surrounding media are simply air. (c) The core of the MBR is filled with ethanol. The resonant optical field can be pushed into the core to form the quasi-droplet regime. The simulation is done in COMSOL.	21
2.3	The transmission spectra for the three different coupling regimes.	23
3.1	(a) Exponential tapered fiber; (b) Linear tapered fiber.	26
3.2	Plot of transmission through a tapered fiber as a function of laser frequency. The FWHM is used to determine the Q-factor.	27
3.3	Microsphere and micropendulum fabrication process. (a) The sphere fabrication setup. The focal length of the ZnSe lens is ~ 60 mm. (b) A optical fiber is melted and transformed to a microsphere or a micropendulum by following step (i) to (iv).	28
3.4	Fabricated microsphere (a) and micropendulum (b). The typical diameter of a microsphere fabricated in our laboratory ranges from $40 \mu\text{m}$ to $200 \mu\text{m}$. The typical diameter of a micropendulum diameter ranges from $80 \mu\text{m}$ to $120 \mu\text{m}$, with a stem length and stem thickness from $100 \mu\text{m}$ to $500 \mu\text{m}$ and $1 \mu\text{m}$ to $3 \mu\text{m}$, respectively.	29
3.5	Microbubble and microbottle fabrication process. (a) The setup with CO_2 laser for the fabrication. (b) A microbubble and a microbottle fabricated from a tapered silica capillary following steps (i) to (iii).	30
3.6	Fabricated microbubble (a) and microbottle resonator (b). The diameter of a microbubble resonator fabricated in our setup ranges from $100 \mu\text{m}$ to $200 \mu\text{m}$ and the wall thickness is between $0.5 \mu\text{m}$ to $2 \mu\text{m}$. The typical diameter of a microbottle resonator is between $30 \mu\text{m}$ and $120 \mu\text{m}$	30
3.7	Microtoroid fabrication process is illustrated in panels (i)-(viii). Panel (a) shows a fabricated microtoroid resonator. A microtoroid is fabricated from a silica-silicon wafer by photolithography. The diameter of the toroids are typically $100 \mu\text{m}$ and the minor diameter is $10 \mu\text{m}$ depend on the mask plate and XeF_2 etching time.	32

-
- 4.1 (a) Schematic of a taper coupled WGR system for transient sensing using CRUS. A pump laser of frequency ω_L , far off resonance with the WGM, ω_0 , is coupled through the tapered fiber with a temporal profile, $S_{in}(t)$. The pulse profile is depicted in (b); the laser pulse starts at a time t_0 and rises up to its maximum within a time t_r . The mathematical description of the pulse is given in Eq. (4.3). (c)-(e) Transient frequency of the laser pulse for different time intervals. (c): $t = [0, t_0]$; (d): $t = [t_0, t_0 + t_r]$; (e): $t = [t_0 + t_r, +\infty)$. At the rising edge of the pulse, the laser source is transiently broadened (d), so a fraction of the pump signal couples to the WGM and contributes to a beat signal between it and the pump source (e). 35
- 4.2 (a). A typical CRUS signal. The beating happens according to the second term and third term of Eq.(4.24). This is due to the frequency broadening at the rising edge of the input signal. We can treat the WGM as an ultra-narrow filter; therefore, only the on-resonance, $\omega = \omega_0$, component in the broadened pump laser signal can be stored in the WGM as shown in (c). (b) The CRUS signal when there is modal coupling with coupling strength, g . The beating is modulated by a trigonometric envelope of period $(2g)^{-1}$. (d) On the other hand, the modulation also happens when there are two cavity modes separated by $2g$ 39
- 4.3 (a). The transient response of a pulse detuned to the high Q WGM. The legend shows the detuning (normalized to γ) for different curves. (b) The peak heights (less-sharp peak), for different detunings in (a). The peak height decreases when the detuning is smaller than 4γ . If this is the case, the evaluation of the peak height for sensing loses its validity. (c) The peak heights at different coupling conditions, γ_{ex}/γ . (d) Peak heights as a function of detuning for certain coupling conditions with different pulse rise-up times, t_r . (e) A comprehensive simulation of the peak height showing that evaluation of the peak height is valid when the detuning is between 5γ and 20γ in a high Q cavity. 43
- 4.4 Numerical simulation results when the photon lifetime is 3 ns. (a) CRUS signal with different detunings. The external decay rate, γ_{ex} , is set to be 0.5γ . (b) CRUS signal with different external decays. The frequency detuning, $\Delta\omega$, is set to be 0.5γ 45
- 4.5 The experimental setup used for cavity ring-up spectroscopy. A 1550 nm laser is intensity modulated and coupled to the microsphere cavity and the transmitted light pulses are detected using a fast detector, with the signals recorded on a fast digital storage oscilloscope (DSO). 46
- 4.6 (a) The transmission spectrum of the microsphere which has an ultrahigh Q WGM. (b) The peak height measured at different laser detunings simulating a dispersive shift of the microsphere. The red curve is the theoretical fitting based on the published theory. (c)The peak satisfies a linear relationship to γ_{ex}/γ . The inset shows the external coupling coefficient as an exponential function of the coupling gap. 47

4.7	Normalized transmittance signal of CRUS. (a) When the detuning is relatively large, a small sharp peak can be seen following the rising up. (b) When the detuning is decreased, the ringing frequency decreases and the sharp peak become more pronounced.	48
4.8	Transient signal of CRUS in a low Q ($\sim 10^6$) cavity with different detuning. (a) When the frequency is far detuned, the sharp peak cannot be seen clearly. (b)-(d) As the detuning become smaller, the equilibrium transmission level decreases, and the sharp peak become obvious.	49
5.1	(a) The transmission spectrum in the EIT regime; the dashed window is shown in (d). (b) The transmission spectrum in the intermediate regime. (c) The transmission spectrum in the ATS regime. Parameters used are $\gamma_2 = 1.2 \times 10^7$, $\gamma_1 = 100\gamma_2$ and $\gamma_{ex} = \gamma_1/3$; $\kappa = 10\gamma_2$ for the EIT regime, $\kappa = \gamma_1 - \gamma_2$ for the intermediate regime, and $\kappa = 10(\gamma_1 - \gamma_2)$ for the ATS regime.	56
5.2	(a) Transduction noise spectrum (red solid line) and the corresponding transmission spectrum (blue dashed line) when the system is in the EIT regime. (b) A zoom-in window of (a) when the detuning is small. (c) Transduction noise spectrum (red solid line) and the corresponding transmission spectrum (blue dashed line) when the system is in the ATS regime. (d) A zoom-in window of (c) when the detuning is around one of the Lorentzian dips. The theoretical plot was generated by Dr. R. Madugani.	57
5.3	(a) Experimental setup for transduction measurement. (b) Fabricated microbubble and (c) microsphere.	59
5.4	The normalized transmission spectrum of the coupled resonators when the two cavities are tuned into resonance. The spectrum shows the transition from the EIT-like to the ATS-like state.	60
5.5	(a) The normalized optical transmission spectrum of the coupled cavities in the intermediate regime. (b) The normalized optomechanical transduction spectrum in the optical frequency domain in the coupled system in the intermediate regime. The theoretical fitting was done by Dr. Y. Yang.	61
6.1	Schematic of the fabrication process for a sol-gel coated MBR using CO ₂ laser heating. (a) A capillary is tapered using a CO ₂ laser heat source. (b) Erbium ions are dissolved into a sol-gel precursor, which is drop-coated onto the tapered capillary. (c-d) The CO ₂ laser heats the sol-gel and internal air pressure is applied until an MBR is formed.	64
6.2	Schematic of the setup for pressure tunable lasing in an MBR. P: pressure gauge; OS: optical switch; PD: photodetector; OSC: oscilloscope; OSA: optical spectrum analyzer. The inset shows a microscopic image of the sol-gel coated MBR. The diameter of the MBR is 141 μm	65

6.3	(a) Lasing threshold measurement of a sol-gel coated MBR. The total power of the pump laser is used for estimation. The threshold is about 27 mW for the pump laser. (b) The spectrum with the pump power below threshold. (c) The single-mode lasing spectrum near the threshold.	66
6.4	(a) The laser spectrum of the sol-gel coated MBR at different pressures. The arrow shows the direction of the pressure increase. From the bottom to the top are the laser emission lines from 0 bar to 2.5 bar applied pressure. The resolution of the spectrum is limited by the OSA. (b) The wavelength shift of the lasing mode as a function of the applied pressure. The red line is a linear fit and the error bar is set by the resolution of the OSA.	67
6.5	(a) The transmission spectra at 1535.66 nm for different pressure. From the bottom to the top are transmission spectra at 0, 1, 1.5, 2 bar, respectively. The arrow shows the direction of the WGM shift due to the increase of the internal pressure. (b) Pressure tuning sensitivity fitted from the transmission spectra.	68
7.1	(a) Total dispersion (in terms of derivation of the FSR) of WGMs in a microbubble with a wall thickness of 1.5 μm . The gray area is the anomalous dispersion region. (b) Zero dispersion wavelength of a microbubble with a wall thickness varying from 1.0 μm to 2.0 μm , simulated in MATLAB. The radius $r = 80 \mu\text{m}$	71
7.2	(a) Microscope image of the MBR. The diameter is measured to be 120 μm . (b) SEM image showing the cross-section of the MBR. The typical wall thickness is 1.5 μm , as shown in the inset. The actual wall thickness should be less than this, as explained in the main text. (c) Experimental setup for measuring the frequency comb in the MBR. TLS, tunable laser source; BS, beam splitter; FPC, fiber polarization controller; PD, photodetector; OSA, optical spectrum analyzer; DSO, digital storage oscilloscope.	73
7.3	Transmission spectrum of the MBR. The inset shows the transmission of the pump WGM in the experiment. The red curve is a Lorentzian fit with a FWHM of about 19 MHz, corresponding to a Q-factor of about 2×10^7	74
7.4	Four-wave mixing spectrum of the MBR with a diameter of 120 μm , shown in Figs. 26(a) and 2(b). The separation between the peaks is 2.1 nm.	75
7.5	Frequency comb generation in the MBR at a center wavelength around 765 nm. Up to 14 comb lines are excited.	75
7.6	An improved Kerr frequency comb. More than 40 comb lines have been observed.	76

8.1	(a) Schematic diagram of the stimulated Raman scattering process. (b) Schematic of the experimental system. The input laser is coupled to a silica microsphere resonator through a tapered fiber waveguide, with a coupling constant, γ_{ex} , and resonator intrinsic loss, γ_{in} . Comparison of the gain spectrum and the lasing modes between (c) a typical homogeneously broadened laser and (d) a silica Raman laser. Schematic of (e) a cascaded Raman laser in single-mode fashion and (f) a two-mode Raman laser.	80
8.2	(a) a typical homogeneously broadened laser and (b) a silica Raman laser. Schematic of (c) a cascaded Raman laser in single-mode fashion and (d) a two-mode Raman laser.	81
8.3	Simulation results based on Eq. (8.1) (see Appendix C for details). (a) P_0 , P_1 , and P_2 represent the intracavity powers of the pump, the first, and the second Raman fields. The external pump power is increased when detuning is set to 0. Solid lines represent the stable, steady state, while the dashed lines correspond to unstable cases. (b) The total gain of the two Raman modes and gain fraction from pump and Mode I to Mode II. The parameters used in (b) are $\gamma_j = 25.3 \mu s^{-1}$ and $\gamma_{ex,j} = 26.2 \mu s^{-1}$ for all $j = 0, 1, 2$; the angular frequencies are $\omega_0 = 2\pi \times 390.6$ THz, $\omega_1 = 2\pi \times 377$ THz and $\omega_2 = 2\pi \times 375.3$ THz; and the intracavity Raman gain coefficients are $g_{01} = 3.6 \times 10^{18} s^{-1} J^{-1}$, $g_{02} = 2.7 \times 10^{18} s^{-1} J^{-1}$ and $g_{12} = 0.5 \times 10^{18} s^{-1} J^{-1}$	83
8.4	The output of two Raman lasers and the transmission spectrum (T) of the pump mode as it evolves with pump detuning. The input power is fixed at $I_0 = 0.6$ mW. Other parameters are the same as those in Fig. 8.3(b).	84
8.5	Switching process of the Raman lines is observed by scanning the pump laser in the blue-detuned region of a cavity mode at 768.1 nm. From (a) to (d), the detuning of the pump is approximately set at 20 MHz, 18 MHz, 15 MHz and 10 MHz, respectively. (a) The first Raman laser at 795.9 nm appears (Mode I). (b) The second Raman line (Mode II) at 799.4 nm appears. (c) Mode I is suppressed while Mode II becomes stronger. (d) Mode I is annihilated and only Mode II remains.	85
8.6	The output powers of Mode I and Mode II are negatively and linearly correlated with each other.	86

Chapter 1

Introduction

1.1 Whispering Gallery Mode Resonators

Generally speaking, electromagnetism is the most common interaction of the four interactions in the standard model, and it is observed in our daily life. Light is the fastest and cheapest way to convey electromagnetic waves. The weakness is that light tends to only have subtle interactions with materials. Therefore, for example, resonant circuitry was used to amplify light signals in early telecommunication technologies. In 1960, the discovery and invention of the laser enhanced the interaction greatly [1]. This later enabled light to selectively cool or control particles, provide stable and fast optical communication through optical fibers, etc.

Whispering gallery mode (WGM) resonators are optical microcavities named after the study of acoustic resonances in the whispering gallery of St. Paul's Cathedral (London) by Lord Rayleigh [2]. Instead of the acoustic wave in the original whispering gallery, light is confined in WGM optical resonators due to total internal reflection (TIR) and forms a 3-dimensionally distributed optical mode. The frequencies of the modes have discrete values characterized by the mode number, which is determined by the solution of the Helmholtz equation for the particular cavity geometry - more details on this are given in Chapter 2. Other than at resonance frequencies, light cannot be coupled into WGM resonators (WGMR) due to destructive interference of the different pathways. This technique using cavities is amongst one of the most efficient ways of enhancing the interaction between light and materials.

Compared to other optical cavities, such as Fabry-Pérot interferometers [3], photonic crystal microcavities [4], and microring resonators [5], WGMRs made from silica have a superior quality (Q-) factor. The Q-factor indicates the quality of energy storage in an optical resonator, where a high value of Q means low energy loss. While a Q-factor of 0.8×10^{10} is the theoretical limit in a high-purity, fused silica microsphere [6], a Q-factor of 10^7 is easily achieved in standard silica WGM cavities, such as microtoroids [7–9], microbubbles [10–14], microbottles [15–19], and microspheres [7, 20]. Silicon WGM resonators initially had relatively low Q-factors because of the surface chemistry treatment used. However, a Q-factor of 10^9 can now be routinely achieved by exploiting a newly invented polishing method [21]. Such a high Q-factor and the small mode volume [22] invoke strong light-matter interactions. An ultrahigh finesse of 10^6 [23] is also a remarkable characteristic of WGM cavities.

Different whispering gallery cavity geometries have different advantages. One of the easiest ways of achieving a high Q is to fabricate a microsphere. However, in order to get stronger interaction between light and matter, a microtoroid resonator is preferred, since light is more tightly confined therein than in a microsphere [7–9]. An alternative resonator geometry is the microbubble, a hollow structure with a thin wall. For these devices, resonant modes can be shifted by applying internal air pressure, and sensing applications are easily envisioned by inserting a solution of a target molecule inside the cavity [11–14, 24]. Especially for the biosensing application, the hollow structure can be included in a microfluidic system, as well as a microbottle resonator with a thin wall hollow structure [19].

SiO_2 (silica) is widely used in this field because of its low cost and low loss in the telecommunications waveband. At such wavelengths, Kerr nonlinearity of silica can be exploited in a WGM cavity to study nonlinear optics. However, other materials may also be used to make WGM cavities. For example, transparent liquid droplet cavities have better tunability [25–29], chalcogenide glasses (As_2Se_3) have a wider transparency window in the mid-infrared wavelength [30], lithium niobate (LiNbO_3) enables second-order nonlinearity applications [31–34], and calcium fluoride crystalline (CaF_2) resonators can have extreme Q -factors of 10^{13} in the ultraviolet band [35].

All of these facts lead to applications of WGMRs from ultralow threshold nonlinear optics [36, 37] and lasing [38], to bio/chemical sensing [39–42], telecommunications [43, 44], quantum optics [32], and optomechanics [45–47]. For example, a frequency comb can be generated using the concept of nonlinear optics and it can be used as an optical clock to improve the precision of time measurements. A microlaser may be used as a sensor, communication or operation system in micro-robotics. Bio/chemical sensing using WGM cavities can retrieve information on particles or their reaction without interruption, thus monitoring the physical condition of a patient without dosage may be possible. WGMRs may also be used as a fundamental logic element in an integrated optical device for performing ultrafast computation. Apart from technical applications, these devices have also proven to be test-beds for fundamental physics in areas as diverse as chaos theory [48] and quantum mechanics [49, 50].

1.1.1 Hollow Whispering Gallery Mode Resonators

The microbubble resonator is a relatively recently developed geometry of WGMRs [10]. It can be fabricated by tapering and expanding a silica capillary. The resonator’s main features are its hollow structure and wall thickness as small as $0.4 \mu\text{m}$, while still maintaining a high Q [13]. Such features can be used for sensing and nonlinear optics application.

1.2 Whispering Gallery Mode Sensors

Optical sensors are one of the major applications of optical devices. For example, in the field of fiber optic sensors, fiber optic Bragg grating sensors have been developed as they are small (and, therefore, lightweight), have multiplexing capability, and are immune to electromagnetic interference (EMI) [51]. The sensitivity of an optical sensor

depends on the strength of interaction between light and the target. In that sense, optical resonators, in particular WGM cavities, can confine light inside a micron-scaled cavity for a long time duration. For example, light can be confined inside a silica microsphere of diameter $\sim 100 \mu\text{m}$ for ~ 500 ns. This results in an ultrathin linewidth in the transmission spectrum. Any change to the transmission spectrum can be clearly detected and, therefore, extremely high sensitivity to the perturbation of the resonance condition is achieved. The perturbation by a target results in a change to the resonance condition: for example, a refractive index change in a surrounding medium can shift the resonant frequency [52], or adhesion of a nanoparticle can result in resonance linewidth broadening [53] and mode splitting [54]. In an experimental setup, a resonance mode of a WGM cavity is monitored as a transmission dip, by scanning the input laser frequency (see Fig.1.1(a)). In this system, the perturbation can be monitored as a frequency shift, bandwidth broadening, and mode splitting of the resonant transmission dip (see Fig. 1.1(b)). The frequency shift, or resonant wavelength shift, can be brought about by several changes: for example, thermal expansion of the cavity or a refractive index change in the surrounding medium. These are termed as *dispersive* changes, or for the purpose of sensing, dispersive sensing. Linewidth broadening is when an additional loss is introduced to the cavity, for example, when a nanoparticle is attached to the cavity and absorbs light. This is termed as a *dissipative* change or dissipative sensing. Mode splitting is due to reflection of light inside the cavity, where degenerate clockwise and counter-clockwise optical modes undergo different shifts; this can also be caused by the presence of a nanoparticle.

The experimental study of WGM-based sensors has mainly been done in biosensing. For example, pioneer work by Vollmer et al. used a microsphere to detect bovine serum albumin (BSA) protein and the binding event of streptavidin protein to BSA in 2002 [55]. To date, many improvements have been done in this context [39, 54, 56–58]: the mode volume can be decreased using a small cavity [39], the cavity loss (\sim linewidth) can be compensated for by optical gain [54, 57], real-time DNA reactions [59] and phage protein binding event [60] can be monitored. However, sensing applications using WGM cavities are not limited to biomolecules. Refractive index sensing [52, 61], temperature sensing [12, 62, 63], pressure sensing [64, 65], and stress sensing [66, 67] are also possible due to the ultrahigh Q of the WGM cavity.

1.2.1 Cavity Ring-Up Spectroscopy Sensing

As already mentioned, by sweeping the laser frequency, the transmission spectrum through the coupling waveguide can be recorded. Any changes to the frequency, mode splitting, or linewidth are used to monitor perturbations induced by the physical parameter that is being sensed. During measurements, the transmission spectrum represents a steady state of the coupled system due to limitations on the scanning speed, thereby constraining the time response of the sensor [68–70]. For a WGMR with an optical Q-factor $> 2 \times 10^7$, a ringing effect is observable even if the laser is scanned as quickly as 100 Hz [71]. The ringing spectrum can be used to distinguish between the overcoupling and undercoupling cases [72]. When the scanning speed is faster than

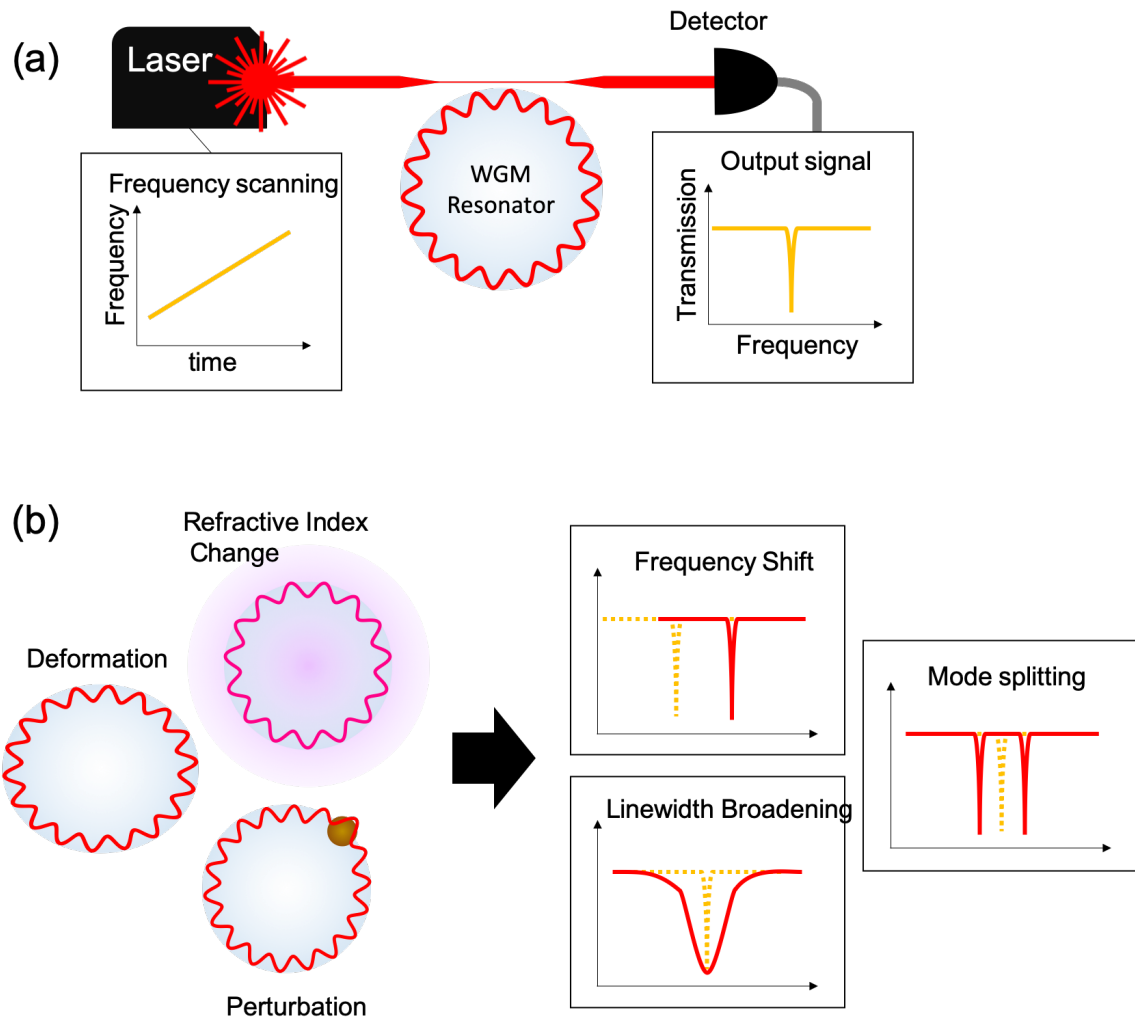


Figure 1.1: (a) Input laser frequency is scanned by a laser controller. The laser light couples into the WGM cavity through the evanescent field of a tapered optical fiber. When an optical mode exists, a transmission dip can be seen on a digital storage oscilloscope (DSO). (b) Frequency shift, linewidth broadening, or mode splitting happens when the resonant condition is changed: for example, deformation of the cavity geometry, refractive index change or or perturbation by a nanoparticle.

the *character speed*, as defined in [70]¹, the steady state treatment can no longer be used to describe the coupled-mode system. For example, if the Q-factor is as high as 10^7 , $\sim 10^{-7}$ s are needed to retrieve dispersive and dissipative information by scanning the laser frequency. If the Q-factor is lower, a longer scanning time is needed. This is not fast enough to sense certain phenomena such as heat dissipation [73], transient particle events (for example, we have observed Brownian motion of nanoparticles in a liquid core MBR that cannot be monitored by an absorption dip change), and fast biochemical events such as methyl proton rotation [74] and hydrated protein relaxation [74, 75]. For example, transient sensing is possible by recording lineshape changes in the ringing tail of an observed transmission spectrum, either by (i) a scanning probe laser or (ii) a fixed laser in resonance with a high Q mode [70]. A proof-of-principle experiment based on the ringing phenomenon has recently been reported [76].

Another possible approach is to send light pulses, which are far detuned from a WGM resonance, through the optical coupler. The retrieved signal on the coupler's output shows an oscillatory lineshape similar to that in [70]; this effect is termed *cavity ring-up spectroscopy* (CRUS) [69] and the rising edge of the light pulse leads to transient broadening. Even though the light is far detuned from the whispering gallery mode, a fraction can still be coupled into the cavity if the broadening is much larger than the detuning. The system is not affected by thermal or nonlinear processes which may arise due to the ultrahigh Q of the mode. The ringing effect occurs within the lifetime of the WGM and, therefore, can be used for ultrafast sensing. The transient capability of CRUS has already been demonstrated by measuring the time response for thermorefractive effects, Kerr nonlinearity and optomechanical vibrations [69]. To date, there has been no thorough theoretical investigation of CRUS and details, such as the influence of the pulse's rise time on the observed spectra, are relatively unknown. We have used coupled-mode theory to solve the related differential equations without relying on the steady state assumption. An approximate analytical solution was obtained and compared to a precise numerical transient solution. The theoretical results fit well to experimental data that we obtained for a silica microsphere resonator. The influences of the pulse rise time, the coupling condition, and the detuning on the ring-up spectrum have been determined given. The possibility of using CRUS in a low Q ($\sim 10^6$) cavity was also explored. This provides a solid foundation for future applications in transient sensing [77].

1.2.2 Optical Trapping with Whispering Gallery Mode Resonators

The sensitivity of a sensor depends on the optical coupling regime. For example, if one uses a tapered fiber to couple light into the cavity, the linewidth depends on the distance between the fiber and the WGM resonator, as we will see in Chapter 2. This means that the cavity can have different responses to the perturbation from a sensing target. Adjusting the cavity to the most sensitive part, i.e., controlling the position of a WGM cavity, can improve the sensing performance. In a tapered fiber optical coupling system, the position of the WGM cavity can be adjusted by a nanostage. However, for practical

¹Character speed is γ^2 , where γ is the decay rate in a cavity.

purposes, e.g. if one wanted to mass-produce optical devices based on WGM cavity sensors, controlling the position of the cavity by an optical force could be a realistic, efficient, and reasonable method. Therefore, investigating optical forces is important for sensing applications. The optical force can be excited as the interaction induced by the evanescent field between optical cavities. Several theoretical studies have been done to investigate optical forces in different optical cavities. In a dual-ring structure, the dependence of the attractive and repulsive forces on the resonant frequency and the coupling strength between the structure and input waveguide have been investigated [78]. The strength of the force also depends on the interacting surface area. This has been shown by assuming parallel planar waveguides and solving Maxwell's equation [79] and making an *optical spring*² assumption [80].

Optical forces can also be excited between two adjacent WGM cavities. When two WGM cavities are adjacent to each other, a so-called *supermode* can be excited. In this condition, the optical resonance for each cavity cannot be described separately and the two cavities should be treated as a single optical resonator [81–83]. An optical mode is split into symmetric and anti-symmetric supermodes that can be excited depending on the displacement between the two WGM cavities, c.f. Fig. 1.2(a). The optical force caused by the supermodes are estimated to be able to control the position of microcavities [84], where, in the study, 100 nN of force is estimated when the distance between the two cavities is smaller than 500 nm and the Q-factor is higher than 10^8 . The electrostatic force is also estimated to be on the order of a few pN, which is negligibly smaller than the optical force in a silica microsphere cavity. Work based on numerical calculations shows when two input lasers are slightly blue-detuned from each supermode, two split supermodes can be described; the symmetric supermode can be excited when the displacement is large and an attractive force is excited between the two cavities, whereas the anti-symmetric supermode is excited when the two cavities are close to each other and the force is repulsive force [85], c.f. Fig. 1.2(c) and (d).

While conventional WGM cavities are fixed to a substrate or a stem, a special type of microsphere called a micropendulum can undergo a significant displacement change [86]. In a coupled-cavity system with a fixed WGM cavity and a micropendulum, the optical force can be used to align the position of the micropendulum and trap it at a certain distance from the fixed cavity. The center of the trap can be shifted by applying static charge; therefore, manipulation of the coupling distance is achievable. Another concern is about the possibility of exciting the supermodes, since the two cavities must be in resonance for the same frequency. This difficulty can be resolved by using a microbubble resonator, since its resonance frequency can be easily tuned by internal air pressure. Therefore, controlling the coupling regime of a micropendulum cavity using the optical force may be achieved by placing a microbubble resonator adjacent to a micropendulum resonator, see Fig. 1.2(b).

Further investigation is required to estimate the optical force of the coupled-cavity system. A theory must be developed to relate the trapping information to the optical information, so that the optical force can be retrieved by analyzing the transmission spectrum. The transmission spectra of the supermode for different distances have been studied in [83]. The information on the optical force can be estimated by the ratio

²The optical force works in the opposite direction to the displacement of the two parallel waveguides.

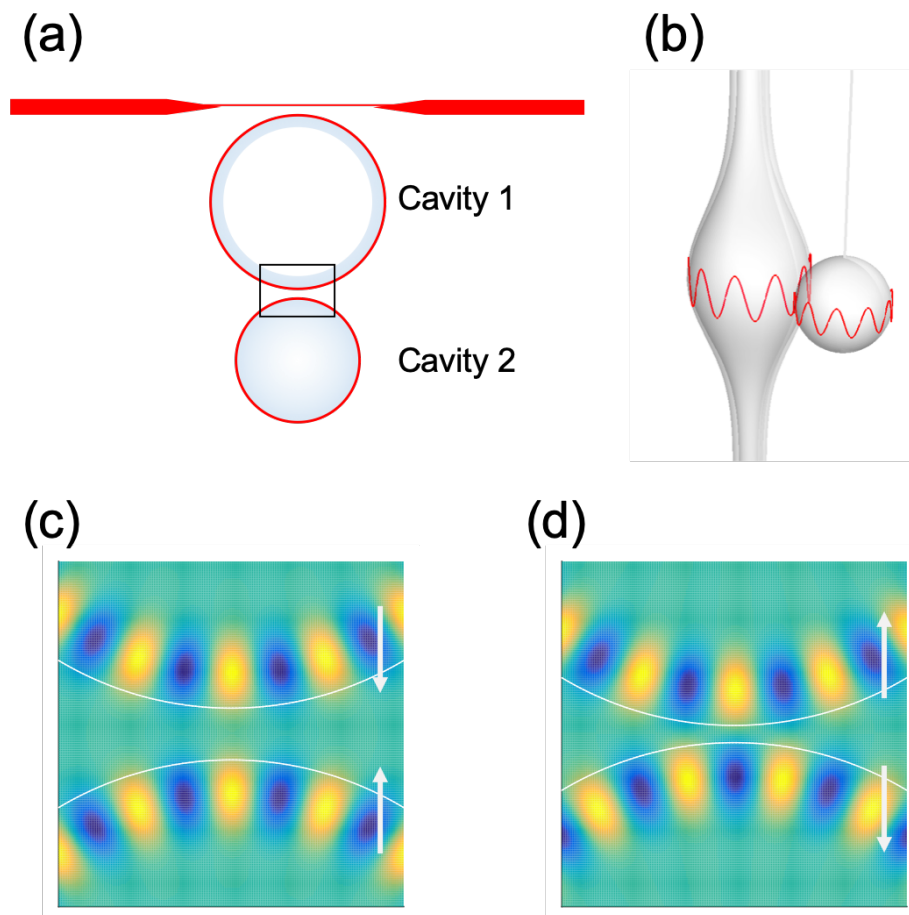


Figure 1.2: (a) Two WGM cavities are coupled to each other while the system is coupled to a tapered optical fiber. (b) One cavity could be a microbubble resonator and the other could be a micropendulum resonator. (c) The symmetric supermode is excited, generating an attractive optical force, when the displacement of the two cavities is large. (d) The symmetric supermode is excited, generating a repulsive force, when the displacement of the two cavities is small.

of the frequency shift to the change in displacement [84, 85]. The mechanical oscillation provides a small displacement. However, is large enough to be monitored as a vibration of the resonant frequency [46]. More generally, the vibration of the resonant linewidth is mixed with the vibration of the resonant frequency [86]. Therefore, the trapping force can be estimated using a comprehensive theory that has been developed based on the study of the transmission spectra of coupled resonators [83, 86]. Subsequently, experimental work was needed in order to determine the trapping efficiency. As a test-bed, a microsphere with a vibrating piezo stage can be used instead of a micropendulum.

1.2.3 Microbubble Lasers for Pressure Sensing

When observing the change of spectral information of an optical mode for sensing, a laser mode can have a narrower linewidth than the transmission dip. The lower limit of the laser linewidth, Δf , is described by the Schawlow-Townes formula [87] and is proportional to the square of the inverse of the Q-factor when lasing does not exist:

$$\Delta f = \frac{hf^3\beta}{4\pi P \cdot Q^2}, \quad (1.1)$$

where P is the output laser power, f is the laser frequency, and β is the spontaneous emission factor representing how efficiently the spontaneous emission from the medium material is coupled to the lasing mode. Ultra-narrow linewidth lasing of 4 Hz at 1550 nm wavelength has been reported in [88]. As stated before, WGMRs can have ultrahigh Q-factors and relatively small mode volumes. Very high Q, low threshold WGM microlasers can be realized when the resonator is made from a material with gain [89–91]. For this purpose, many fabrication methods have been developed [92], one of which is the sol-gel wet chemical synthesis technique. Rare earth ions are mixed into the sol-gel precursor solution and, based on the hydrolysis and condensation reactions of metal-alkoxide precursors in aqueous solutions, alcohol, or other media, a silica film can be formed with the gain medium. Microlasers made from sol-gel coated microspheres [93, 94] and microtoroids [95] have already been realized. Such active WGMRs are used for applications such as nanoparticle sensing [54] and fundamental physics research [9, 96, 97]. Sol-gel is a low-cost, flexible way to functionalize a WGM resonator and can also be applied to microbubble resonators as we shall discuss in the following.

Microbubble resonators are a more recently developed geometry of WGMRs [10, 11, 41]. They are hollow, while still maintaining a high Q-factor and small mode volume. Similar to other WGM resonators, microbubbles can also be used in a wide variety of applications, such as nonlinear optics [18, 98], sensing [61, 64, 65], and optomechanics [99]. Active microbubbles have also been developed by injecting dye solution [100, 101] or other bio-chemical liquids [102] into the core of the resonator such that lasing emission can be achieved. In order to achieve lasing from the wall instead of the core, a glass-on-glass wetting technique was developed [16], whereby bulk Er-doped glass was melted onto the surface of a microcapillary. The wall thickness was limited in this method. To fabricate a microbubble resonator with a thinner, gain-activated wall and to improve the attainable sensitivity, alternative methods need to be found.

In this work, we used a sol-gel coating technique to introduce Er^{3+} ions onto the wall of a microbubble and lasing in the 1550 nm band was realized. With a subwavelength wall thickness, internal aerostatic pressure applied to the wall of the resonator could provide the lasing frequency shift. Sensing applications using a WGM cavity based microlaser have already been reported in [54, 92, 103]. However, the hollow structure of the microbubble allows us to sense changes from the inner surface of the wall. This has advantages when used in microfluidic systems and can avoid the disturbance that a sensing target may have to the optical coupling condition.

1.3 Nonlinear Optics with Whispering Gallery Mode Resonators

The confinement of laser light in WGM cavities strongly enhances interactions between light and matter. Therefore, the nonlinear polarization of the material plays an important role in WGM cavities. The polarization, \mathbf{p} , of the material can be expressed in a Taylor expansion as follows [104]

$$\mathbf{p} = \epsilon_0 [\chi^{(1)} \mathbf{A} + \chi^{(2)} \mathbf{A}\mathbf{A} + \chi^{(3)} \mathbf{A}\mathbf{A}\mathbf{A} + \dots], \quad (1.2)$$

where ϵ_0 is the vacuum permittivity, \mathbf{A} is the light field and $\chi^{(i)}$ are $(i+1)h$ rank nonlinear permittivity tensors. For instance, the second term, with $\chi^{(2)}$, is expressed in detail as

$$p_i^{(2)}(t) = \epsilon_0 \sum_{ijk} \chi_{ijk}^{(2)} A_j(t) \cdot A_k(t), \quad (1.3)$$

where i, j, k refer to each component of the parameters in the Cartesian coordinates. Equation 1.3 describes the second order nonlinearity during the light and matter interactions. If we assume the light field takes discrete values of frequency, ω_1 and ω_2 , as is usually the case in a WGM cavity, Eq.1.3 predicts the generation of different frequencies. This is the so-called *three-wave mixing* process that has been extensively studied [31, 33, 105–107]. For simplicity, we suppose there is only one Cartesian component and the optical field takes the form $A = A_1 e^{-i\omega_1 t} + A_2 e^{-i\omega_2 t} + c.c.$ Terms from A^2 with nonzero $\chi^{(2)}$ components predict frequency conversions such as second-harmonic generation (SHG), where $\omega_{SHG1} = 2\omega_1$ and $\omega_{SHG2} = 2\omega_2$, sum-frequency generation (SFG), where $\omega_{SFG} = \omega_1 + \omega_2$, and difference-frequency generation (DFG), where $\omega_{DFG} = \omega_2 - \omega_1$. Vacuum fluctuation enable ω_1 and ω_2 to be generated by an optical pump at frequency ω_p , where $\omega_p = \omega_1 + \omega_2$. This is known as *spontaneous parametric down conversion* (SPDC).

Inside an optical cavity, however, these conditions are not automatically satisfied. Material dispersion shifts frequencies unequally, thus energy conservation may not be satisfied during the conversion. Nevertheless, many techniques are found and used to achieve energy conservation, i.e., the phase-matching condition, during the wave conversion process. SHG has been achieved using a pump near 1550 nm by polling a pattern on a lithium niobate microtoroid [31]; SPDC has been achieved and a non-classical signal-idler pair has been generated, separated by 100 nm wavelength near 1060 nm, using a 532 nm pump, by applying temperature and voltage to a MgO-doped

lithium niobate WGM resonator [33]; SFG has been experimentally demonstrated at a 1560 nm pump and 780 nm signal by tuning the input polarization in a MgO-doped lithium niobate microdisk [106]; DFG is expected to be achieved in a GaAs microdisk by geometrical control of the effective refractive index [105].

The third order nonlinearity term involves various phenomena satisfying the energy conservation of four waves, $\omega_4 = \omega_1 + \omega_2 + \omega_3$, termed *four-wave mixing* (FWM). Various wave generation processes and nonlinear effects are possible in different combinations of different frequencies and their signs. When ω_1 , ω_2 and ω_3 are of the same frequency and one of the three has a different sign to the other two (since it is the complex conjugate), then no new wavelength is generated; however, the effective refractive index may be shifted depending on the laser power. This is called *self-phase modulation* (SPM). *Cross-phase modulation* (XPM) is another mechanism used to shift the effective refractive index. This is described by terms satisfying, for example $\omega_2 = -\omega_3$. These phase modulations do not require the phase-matching condition to be satisfied since no photons at new frequencies are generated. Terms with $\omega_1 = \omega_2 = \omega_3 = \omega$ describe the frequency generation of $\omega_{THG} = 3\omega$, i.e., *third harmonic generation* (THG). When two pump photons ω_p generate a pair of idler-signal photons (ω_i and ω_s), possible due to the vacuum fluctuation, we call it *hyper-parametric oscillation* or *spontaneous four-wave mixing* (SFWM). As long as the phase-matching condition is satisfied, the photon pair generation process by the hyper-parametric oscillation is cascaded and can lead to frequency comb generation.

1.3.1 Frequency Comb Generation in a Microbubble Resonator

A frequency comb is a light source with equidistant lines in its optical spectrum. It can be generated from four-wave mixing (FWM) and mediated by hyper-parametric oscillation. In modern optics, frequency combs have applications in many areas such as frequency metrology [108], precise optical clocks [109], and biomedical imaging [110]. In the last decade, whispering gallery mode resonators have emerged as excellent devices for frequency comb generation. Frequency comb generation was first introduced by a fiber laser [111] and a mode-locked laser cavity [112]. The number of comb lines present is related to the pulse intensity and the spectral distance between comb lines is inversely related to the cavity size of the laser. Therefore, to generate a broadband frequency comb, high power and a small laser cavity are required in a fiber or laser cavity system [109]. WGMR-based combs are miniature in size and do not require a high power fs laser to drive the comb; these benefits arise from their ultrahigh Q-factor and small mode volume. Frequency combs have been realized near the telecommunications bands in different types of WGMRs such as microspheres [113], microtoroids [114, 115], microrings [116], microdisks [109, 117, 118], and microbubbles [119–121]. Frequency combs in WGMRs require phase matching over a broadband frequency range where the group velocity dispersion (GVD) plays an important role and is crucial for achieving the maximum comb bandwidth [122]. In WGMRs, the GVD is determined by (i) the material dispersion described by the Sellmeier formula and (ii) the geometric dispersion due to non-equidistant mode distribution in the resonator. By changing the material and selecting higher-order whispering gallery modes, the zero dispersion wavelength (ZDW) can be redshifted [123, 124], thus expanding the possibility of frequency comb

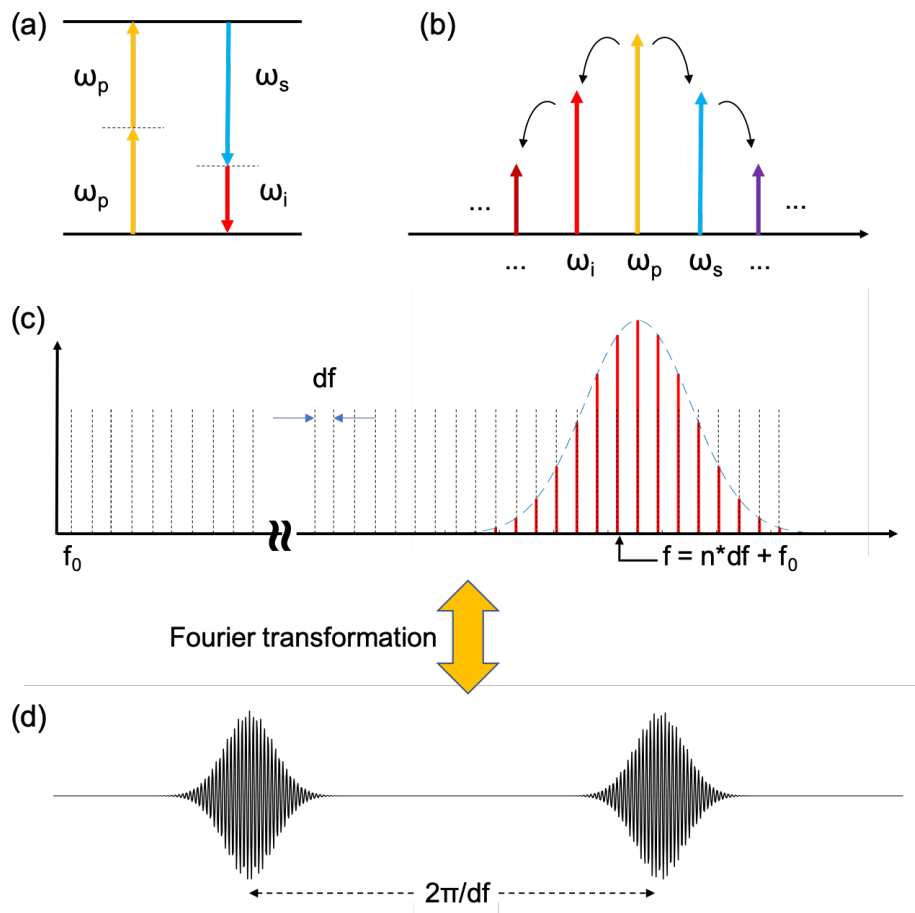


Figure 1.3: (a) Energy diagram representing hyper-parametric oscillation. Two pump photons are converted to an idler-signal photon pair. (b) The cascaded hyper-parametric oscillation process. (c) Comb lines in the frequency domain. (d) A Fourier transformation of the frequency comb, in the time domain.

generation to the mid-infrared (MIR) range [125–127]. Apart from extending the wavelength range of a frequency comb towards the infrared, it is also highly desirable to do the opposite, i.e., move the frequency comb to shorter wavelengths e.g. the visible region. For example, a frequency comb around 780 nm can be used to lock a laser to the rubidium D₂ transitions [128] as required in atomic clocks. Moreover, in a water environment, the light from a near-infrared (NIR) or MIR frequency comb will be strongly absorbed, whereas the absorption of red or near-red (such as 780 nm) light is much less. Hence, a frequency comb at 780 nm could also be used for biological sensing and optical computed tomography imaging [110, 129, 130].

To obtain a Kerr frequency comb, the ZDW must be shifted toward the visible range. However, this is challenging because of the material dispersion. To date, three methods for realizing frequency combs in the visible spectral region have been reported. One method is to use multiple nonlinear processes simultaneously in a material. A silicon nitride microring was used to generate a NIR comb around 1540 nm, which was converted to the near visible range by engineering the material so that second-order optical nonlinearity (SHG and SFG) emerges [131]. The authors observed 17 comb lines in the 765–775 nm region. In the second method, a frequency comb was generated in the normal dispersion regime. The possibility of generating a frequency comb in this regime has been theoretically discussed and has proven to be extremely difficult to achieve [132]. Nevertheless, assisted by a mode-interaction process, a frequency comb in the anomalous dispersion regime was used to generate new combs in the normal regime [133]. Hence, it could be exploited to generate a comb in the visible range. The third technique relies on engineering the total dispersion of the system. This can be achieved by out-of-plane excitation of the higher-order bottle modes in WGMRs with a parabolic lateral profile [134]. In such a situation, the high Q optical modes propagate along the axis of symmetry. It has been shown that the geometry dispersion of such modes is strongly related to the lateral profile [120, 134]. By choosing the right resonator profile, even at a center wavelength of 780 nm, the total dispersion can be forced into the anomalous regime. Using this technique, a frequency comb centered at 794 nm was observed in a crystalline WGMR [134]. Alternatively, by carefully designing the lateral profile of a wedged silica microdisk, broad-band dispersion control can be obtained [135].

Such advances indicate that visible range frequency combs can be achieved. During this PhD work, we developed a much more controllable method to engineer the dispersion by using a microbubble resonator (MBR). In 2013, FWM parametric oscillation at the telecommunications wavelength around 1550 nm was first reported in an MBR [120] and, later, frequency comb generation was also realized [120, 121, 136]. In an air-filled silica MBR, the mode is distributed both in the wall and in the inner air owing to the evanescent field penetration. By varying the wall thickness, the proportion of the mode intensity in air can be modified, thus changing the effective index and the frequency distribution of the cavity modes [24]. It has been theoretically shown that, by shrinking the wall thickness, the ZDW shifts towards shorter wavelengths [119, 137]. Therefore, it should be possible to generate a frequency comb in the visible range by optimizing the wall thickness of the MBR.

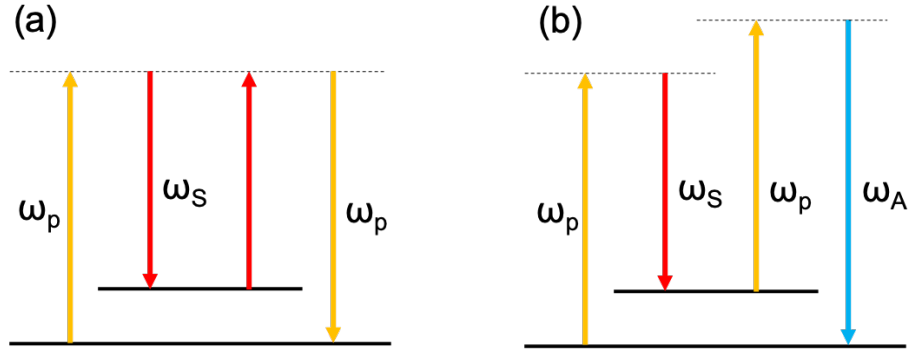


Figure 1.4: The energy diagram of (a) Stokes SRS and (b) anti-Stokes SRS. (a) Stokes SRS is described by $\omega_S = \omega_S + \omega_p - \omega_p$, where ω_p and ω_S are the frequencies of the pump field and Stokes field. The phase-matching condition is not required. (b) In contrast, anti-Stokes SRS is described by $\omega_A = \omega_p + \omega_p - \omega_S$, where ω_A represents the frequency of the anti-Stokes light field. The phase-matching condition must be satisfied between three frequencies [104].

1.3.2 Intrinsic Raman Mode Switching Process with Whispering Gallery Mode Resonators

Light coupled to a WGM resonator can also interact with the vibration of the material's molecules. Light scattered by a long-range lattice wave of the material is called *stimulated Brillouin scattering* (SBS). The light scattered by a local molecule displacement vibration is called *stimulated Raman scattering* (SRS). Those processes can be described by introducing complex third order susceptibility [104] to the system. SBS is not likely to be excited in WGM cavities even though the Brillouin threshold is generally lower than the Raman threshold. The excitation of SBS in a WGM cavity needs the following conditions to be satisfied: (i) The lattice wave must correspond to one of the mechanical resonances of the WGM cavity, (ii) there must be an optical mode that is detuned tens of GHz from the pump mode, where the Brillouin gain band resides so as to support the scattered light, and (iii) the pump light, the lattice wave, and the scattered light must satisfy the energy conservation law. In particular, the second condition is usually not satisfied in a WGM resonator and the other two make the excitation also challenging [138]. Nevertheless, several achievements have been reported in WGM cavities by using a large optical cavity [138] and by using a high-order optical mode that belongs to a different mode family than the pump mode [139].

In contrast, SRS is generally seen in a WGM cavity. While the anti-Stokes SRS needs to satisfy the phase-matching condition, Stokes SRS usually has a broad gain band and can be excited without constraint, once the pump power is above a certain threshold in WGM cavities. Therefore, various WGM cavities support SRS, e.g. microdroplets made from different materials [27–29], CaF₂ crystalline WGM cavities [140, 141], silica WGM cavities [142–144], As₂S₃ glass microspheres [145], polymer coated microspheres [146], and Er³⁺-ion doped microtoroids [95]. The cascaded process can also be easily excited at different wavelengths [140, 143, 146], therefore supporting a wide range of frequency generation. Generally, the frequencies of excited SRS modes are not equally

spaced. However, by carefully tuning the pump laser parameters and cavity dispersion, an equally spaced Raman comb is possible [147]. Note that the dynamics of the Raman formation is relatively unstudied. During this PhD, we have studied interactions between excited Raman modes, theoretically, numerically, and experimentally. For a fairly simple case, we predicted and experimentally demonstrated a mode-switching process.

1.4 Motivation

In this dissertation, the primary motivation is to explore applications of microbubble resonators, especially in developing them as sensors and as tools for nonlinear optics. Chapters 2 and 3 contain general theory and experimental details that are needed when working with WGMRs and, more specifically, MBRs. This then leads into the main works presented within the framework of this dissertation. In Chapter 4, we show how the MBR can be used as an excellent platform for transient sensing, one of the primary applications for which the resonators are suitable. Next, in Chapter 5, we discuss how the MBR can be used in a system where two cavities are coupled for studying optical forces under certain resonance conditions. Applications of the MBR as a tunable microlaser or as a pressure sensing platform are presented in Chapter 6. Then, in Chapter 7, we show that the zero dispersion wavelength can be engineered by playing with the wall thickness of the bubble and this facilitates applications in nonlinear optics, such as frequency comb generation. Finally, in Chapter 8, we show that different patterns of Raman scattering within an MBR can be tuned, leading to the observation and modeling of further nonlinear optics phenomena. The thesis is concluded by putting the work into context for future advances in the field.

Chapter 2

Wave Theory of Whispering Gallery Mode Cavities

2.1 Introduction

In this chapter, we will introduce the theory associated with the intracavity field distribution of light in a microsphere, as essential for WGMs. Next, coupled-mode theory, which has been used to describe experimental work during the course of this PhD, will be introduced. These theories also appear in many other works. For example, the intracavity field distribution theory can be found in [148, 149] and the coupled-mode theory can be found in [150, 151].

2.2 Field Distribution in a Microsphere

In an isotropic medium, where we suppose a permittivity, ϵ , and permeability, μ , are constant, free of charges, and there is no current, Maxwell's equations are given by

$$\nabla \cdot \mathbf{B} = 0, \quad (2.1)$$

$$\nabla \times \mathbf{E} + \frac{\partial \mathbf{B}}{\partial t} = 0, \quad (2.2)$$

$$\nabla \cdot \mathbf{D} = 0, \quad (2.3)$$

$$\nabla \times \mathbf{H} - \frac{\partial \mathbf{D}}{\partial t} = 0. \quad (2.4)$$

Using standard notation, $\mathbf{H} = \mathbf{B}/\mu$ stands for the magnetizing field and $\mathbf{D} = \epsilon\mathbf{E}$ is the electric displacement field. Taking the curl of Eq. 2.2 yields

$$0 = \nabla \times \left(\nabla \times \mathbf{E} + \frac{\partial \mathbf{B}}{\partial t} \right) \quad (2.5)$$

$$= \nabla(\nabla \cdot \mathbf{D}/\epsilon) - \nabla^2 \mathbf{E} + \mu \nabla \times \frac{\partial \mathbf{H}}{\partial t}, \quad (2.6)$$

then substituting Eq. 2.3 and Eq. 2.4 into Eq. 2.6, we get

$$0 = \nabla^2 \mathbf{E} - \mu\epsilon \frac{\partial^2 \mathbf{E}}{\partial t^2}. \quad (2.7)$$

As we are more interested in the spatial distribution of the electric field, we assume that the time dependence of the field is simply $e^{i\omega t}$. The Helmholtz equation is obtained on setting $k = \omega\sqrt{\mu\epsilon}$ such that

$$\nabla^2 \mathbf{E} + k^2 \mathbf{E} = 0. \quad (2.8)$$

We can get a similar relation for the magnetic field by transforming Eq. 2.4 and substituting Eqs. 2.1 and 2.1 into it.

2.2.1 Maxwell's Equations in Spherical Coordinates

If we assume a TE or TM mode¹, as is normally the case in a cavity, the vector field description can also be dropped so that only the vector component parallel to the sphere surface remains. Then, using the separation of variables approach, either the \mathbf{E} or \mathbf{B} field is expressed as $\Psi(r, \theta, \phi)e^{i\omega t}$, where the spatial distribution is

$$\Psi(r, \theta, \phi) = R(r)\Theta(\theta)\Phi(\phi). \quad (2.9)$$

Note we are using spherical coordinates, where the radial, polar, and azimuthal components are represented by $R(r)$, $\Theta(\theta)$ and $\Phi(\phi)$, respectively. Then Eq. 2.8 becomes

$$\frac{1}{R} \frac{d}{dr} \left(r^2 \frac{dR}{dr} \right) + \frac{1}{\Theta \sin\theta} \frac{d}{d\theta} \left(\sin\theta \frac{d\Theta}{d\theta} \right) + \frac{1}{\Phi \sin^2\theta} \frac{d^2\Phi}{d\phi^2} + k^2 r^2 = 0. \quad (2.10)$$

Equation 2.10 can be separated into its variables by following the transformation:

$$\frac{1}{R} \frac{d}{dr} \left(r^2 \frac{dR}{dr} \right) + k^2 r^2 = -\frac{1}{\Theta \sin\theta} \frac{d}{d\theta} \left(\sin\theta \frac{d\Theta}{d\theta} \right) - \frac{1}{\Phi \sin^2\theta} \frac{d^2\Phi}{d\phi^2} \equiv l(l+1), \quad (2.11)$$

$$\frac{\sin\theta}{\Theta} \frac{d}{d\theta} \left(\sin\theta \frac{d\Theta}{d\theta} \right) + l(l+1) \sin^2\theta = -\frac{1}{\Phi} \frac{d^2\Phi}{d\phi^2} \equiv m^2. \quad (2.12)$$

This yields three equations related to r , θ and ϕ :

$$\frac{d^2 R}{dr^2} + \frac{2}{r} \frac{dR}{dr} + \left(k^2 - \frac{l(l+1)}{r^2} \right) R = 0, \quad (2.13)$$

$$\frac{1}{\sin\theta} \frac{d}{d\theta} \left(\sin\theta \frac{d\Theta}{d\theta} \right) + \left[l(l+1) - \frac{m^2}{\sin^2\theta} \right] \Theta = 0, \quad (2.14)$$

$$\frac{d^2 \Phi}{d\phi^2} + m^2 \Phi = 0. \quad (2.15)$$

The constants $l(l+1)$ and m^2 are introduced to solve the equation. When l is a non-negative integer (i.e., $l = 0, 1, 2, \dots$) and m is an integer whose absolute value is smaller than or equal to l (i.e., $m = 0, \pm 1, \pm 2, \dots, \pm l$), Eq. 2.13 is known as a spherical Bessel differential equation and Eq. 2.14 is known as a spherical harmonic differential equation. The general solution of Eq. 2.13 is known to be given by a linear combination

¹TE and TM modes are transverse electric and magnetic modes. When the electric field is parallel to the sphere surface, the resonant mode is called the TE mode. When the magnetic field is parallel to the sphere surface, the resonant mode is called the TM mode

of the spherical Bessel functions, j_l , and spherical Neumann functions, n_l . Considering the spherical Neumann functions diverge at $r = 0$, the solution becomes:

$$R(r) = Aj_l(kr) = A\sqrt{\frac{\pi}{2kr}}J_{l+\frac{1}{2}}(kr) = A\sqrt{\frac{\pi}{2kr}}\sum_{p=0}^{\infty}\frac{(-1)^p}{p!\Gamma(p+l+3/2)}\left(\frac{kr}{2}\right)^{2p+l+\frac{1}{2}}, \quad (2.16)$$

where A is a constant, J_l is a Bessel function of l -th order and $\Gamma(x)$ is the gamma function. Although l appears in the radial component, it is a polar mode number. The radial mode number, n , corresponds to the number of radial field amplitude local maxima. This is related by applying the boundary condition of the cavity, i.e., n is determined and depends on k solved according to the boundary condition, c.f. Fig. 2.1.

The solution of Eq. 2.14 is related to Legendre polynomials, i.e., $\Theta(\theta)$ is proportional to $P_l^m(\cos\theta)$. Together with Eq. 2.15, that can be solved easily, it is generally expressed as the normalized spherical harmonics function:

$$\Theta(\theta)\Phi(\phi) = Y_l^m(\theta, \phi) = C_{lm}P_l^m(\cos\theta)e^{im\phi}, \quad (2.17)$$

with the normalization constant, C_{lm} , noting that m is the azimuthal mode number.

2.2.2 Characteristic Equation

Now we are going to involve the boundary condition in our discussion. We set the center of the spherical coordinate system to correspond to the center of a microsphere with radius, r_0 . We suppose that the microsphere has an ultrahigh Q so that losses are negligible and the theory described in the previous section applies. The boundary condition is that the field and its derivative are continuous at $r = r_0$. For $r > r_0$, the wave travels outwards. This condition is described by the outgoing spherical Hankel functions, $h_l^{(1)}(ikr) = j_l(ikr) + in_l(ikr)$. Then, the boundary condition gives the characteristic equation:

$$\alpha\frac{1}{j_l(n_s k_0 r_0)}\frac{\partial j_l(n_s k_0 r)}{\partial r}\Big|_{r=r_0} = \frac{1}{h_l^{(1)}(in_a k_0 r_0)}\frac{\partial h_l^{(1)}(in_a k_0 r)}{\partial r}\Big|_{r=r_0}, \quad (2.18)$$

where k_0 (corresponding to k/n_s in the microsphere and k/n_a in the surrounding medium) is the wavenumber of light in vacuum. n_s and n_a are the refractive indices of the microsphere and the surrounding medium, respectively, where for silica glass we use n_s and for air or nitrogen gas we use n_a in this thesis. α is the ratio of the refractive indices inside and outside of the sphere. For TE modes $\alpha = n_a/n_s$ and for TM modes $\alpha = n_s/n_a$.² The resonant k_0 value and the radial field distribution can be obtained numerically or approximately as reported in other works [150, 152–155]. Here, Fig. 2.1 is plotted by computing Eq. 2.18 numerically in MATLAB. The resonant value for k_0 is important as it is related to phase-matching and, thereby, it is a key parameter for frequency comb generation. We will revisit this point later in Chapter 7

²The right hand term of Eq. 2.18 always takes a real value even if the numerator and the denominator are generally complex. This can be proven by finding out the recurrent relations and recurrent derivative relations of spherical Hankel functions and applying to $h_0^{(1)}(ikr) = -(1/kr)e^{-kr}$.

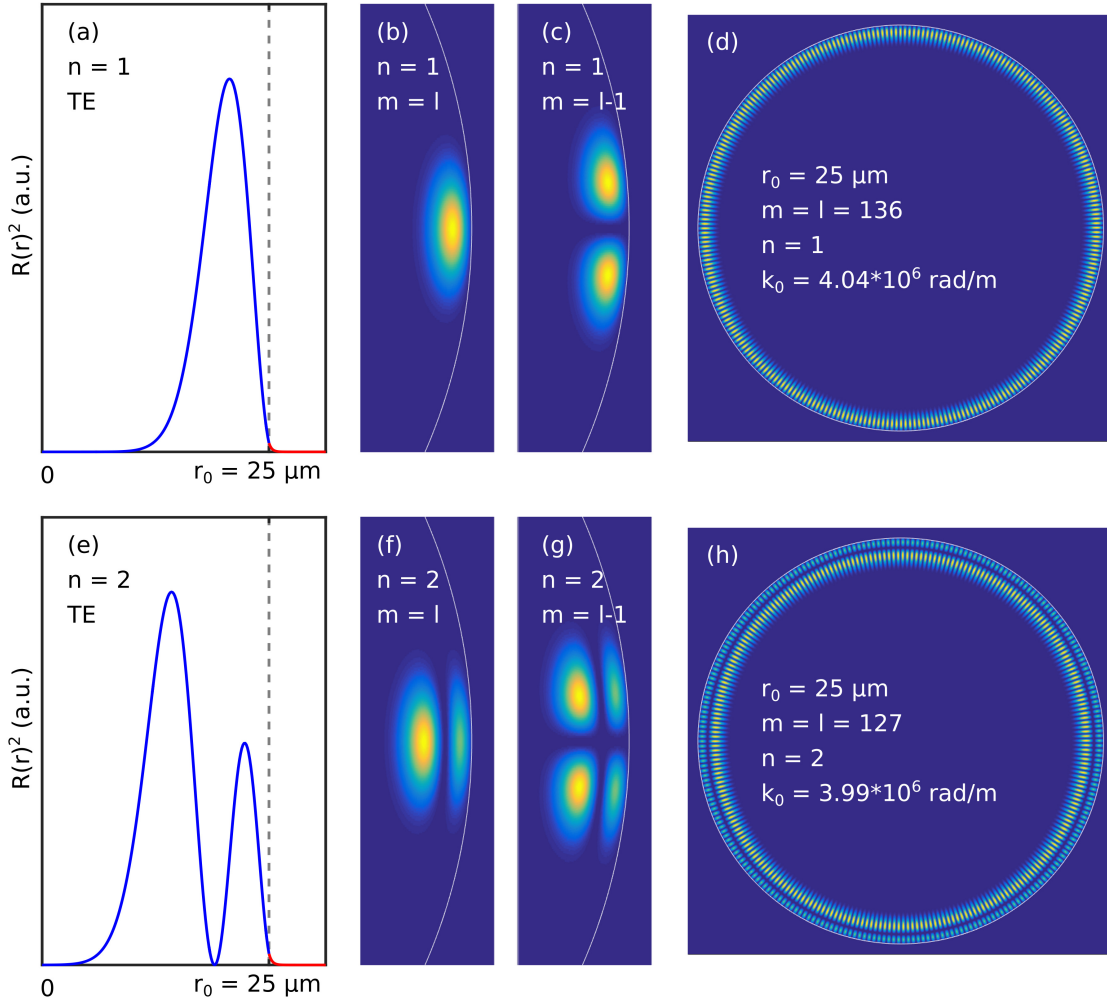


Figure 2.1: Resonant modes obtained by solving the characteristic equation in MATLAB (see Appendix A for details). The diameter of the microsphere is $25 \mu\text{m}$ for all plots. (a)-(d): The resonant wavenumber, k_0 , is $4.04 \times 10^6 \text{ rad/m}$, where $n = 1$ and $l = 136$ is decided by the value of k_0 . (e)-(h): $k_0 = 3.99 \times 10^6 \text{ rad/m}$, $n = 2$ and $l = 127$. The azimuthal mode number, m , can take any integer between $-l$ and l , including 0. The total number of field amplitude maxima is $n \times (l - |m| + 1) \times |m|$. The blue lines in (a) and (e) are norms of the corresponding spherical Bessel functions that describe the intracavity field amplitude and the red lines are norms of the corresponding spherical Hankel functions that describe the evanescent field amplitude.

2.2.3 Free Spectral Range (FSR)

Roughly speaking, the azimuthal mode number, m , relates to the cavity diameter, r_0 , and the wavelength, λ_m , by $m\lambda_m = 2\pi n_s r_0$. Then, we see that

$$mc = 2\pi n_s r_0 f_m, \quad (2.19)$$

$$(m+1)c = 2\pi n_s r_0 f_{m+1}, \quad (2.20)$$

where $f_m = c/\lambda_m$ and $f_{m+1}c/\lambda_{m+1}$, with c being the speed of light in vacuum. Subtracting Eq. (2.20) from Eq. (2.20) we get

$$1 = \frac{2\pi n_s r_0}{c}(f_{m+1} - f_m) = 2\pi n_s r_0 \frac{\lambda_m - \lambda_{m+1}}{\lambda_m \lambda_{m+1}}. \quad (2.21)$$

The free spectral range is defined as

$$\Delta\lambda_{FSR} \equiv |\lambda_m - \lambda_{m+1}| = \frac{\lambda_m \lambda_{m+1}}{2\pi n_s r_0}. \quad (2.22)$$

Strictly speaking, the intracavity field is not distributed on the equator of the sphere but slightly inside. Therefore, the real wavelength, λ , is smaller than what we get by assuming the relationships in Eqs. 2.20 and 2.20. For example, using r_0 and m in Fig. 2.1(d), the approximate wavelength is $\lambda = 1.67 \mu\text{m}$, whereas the real wavelength obtained from the value of k_0 is $1.55 \mu\text{m}$. The free spectral range, $\Delta\lambda_{FSR}$, obtained in Eq. 2.22 is also slightly larger than the real value. It is estimated to be 12 nm in Eq. 2.22) and 11 nm in reality. An effective refractive index may be defined and used to compensate for the difference.

2.3 Optical Field Distribution in a Microbubble Resonator

In a bulk WGMR, the dispersion of the cavity is almost fixed and largely depends on the material. With MBRs it is possible to engineer the geometrical dispersion due to its hollow structure and thin wall. In this context, the resonant k_0 in a capillary was explored numerically by Meldrum and Marsiglio in 2014 [156]. While the theory was developed for a microcapillary, it can also be applied to a microbubble resonator when the optical field is confined to the equator. In this section, we reproduce the theory developed by Meldrum and Marsiglio in [156].

Neglecting the axial part (i.e., $\partial/\partial z = 0$), Maxwell's equations for TE resonances are rearranged in cylindrical coordinates to give

$$\frac{1}{r} \frac{\partial}{\partial r} \left(r \frac{\partial E(r, \phi)}{\partial \phi} \right) + \frac{1}{r^2} \frac{\partial^2 E(r, \phi)}{\partial \phi^2} + k_0^2 n_r E(r, \phi) = 0, \quad (2.23)$$

where E is the field amplitude, r is the radial distance, ϕ is the azimuthal angle and n_r is the refractive index of the medium. Using the separation of variables approach, the azimuthal component is solved, and $E(r, \phi)$ becomes

$$E(r, \phi) = R(r) \exp(\pm im\phi). \quad (2.24)$$

Substituting Eq. 2.24 into Eq. 2.23 yields the Bessel differential equation:

$$r^2 \frac{dR(r)}{dr^2} + r \frac{dR(r)}{dr} + (k_0^2 n_r^2 r^2 - m^2) R(r) = 0, \quad (2.25)$$

where m is the azimuthal mode number. The solution of the radial component of the electric field is known as a cylindrical Bessel function or simply a Bessel function of the first, $J_m(n_r k_0 r)$, and second, $Y_m(n_r k_0 r)$, kind. Now we consider a capillary with inner diameter and outer diameter given by r_1 and r_2 , respectively. Generally, the capillary may be filled with liquid. The refractive index, which depends on the radial positions, is given by:

$$n_r = \begin{cases} n_l & (r < r_1) \\ n_s & (r_1 < r < r_2) \\ n_a & (r > r_2), \end{cases}$$

where n_l , n_s , and n_a are the refractive indices of the intracavity medium (liquid), silica glass, and air, respectively. For $r < r_1$, $R(r)$ should not diverge to ∞ , therefore the second kind of Bessel function, $Y_m(n_l k_0 r)$, is not included. In the silica capillary, there are both incoming, $H_m^{(2)}(n_s k_0 r) = J_m(n_s k_0 r) - iY_m(n_s k_0 r)$, and outgoing, $H_m^{(1)}(n_s k_0 r) = J_m(n_s k_0 r) + iY_m(n_s k_0 r)$, waves. Outside the capillary, the wave is traveling outward. Therefore, the solution of the Bessel differential equation in a silica capillary is expressed as

$$R(r) = \begin{cases} A_m J_m(n_l k_0 r) & (r < r_1) \\ B_m H_m^{(2)}(n_s k_0 r) + C_m H_m^{(1)}(n_s k_0 r) & (r_1 < r < r_2) \\ D_m H_m^{(1)}(n_a k_0 r) & (r > r_2). \end{cases}$$

Here, A_m , B_m , C_m and D_m are proportionality constants. $H_m^{(1)}$ and $H_m^{(2)}$ represent outgoing and incoming waves and are called Hankel functions of the first and second kind. Then, the boundary condition (i.e., $R(r)$ and its derivative, $R'(r)$), should both be continuous at both boundaries, r_1 and r_2) lead to the characteristic equation:

$$\frac{n_a^p H_m^{(1)'}(n_a k_0 r_2)}{n_s^p H_m^{(1)}(n_a k_0 r_2)} = \frac{B_m H_m^{(2)'}(n_s k_0 r_2) + H_m^{(1)'}(n_s k_0 r_2)}{B_m H_m^{(2)}(n_s k_0 r_2) + H_m^{(1)}(n_s k_0 r_2)}. \quad (2.26)$$

We set C_m to be 1 and include the polarization p , where $p = 1$ corresponds to TE modes and $p = -1$ represents TM modes. The B_m are obtained from

$$B_m = \frac{n_s^p J_m(n_l k_0 r_1) H_m^{(1)'}(n_s k_0 r_1) - n_l^p J_m'(n_l k_0 r_1) H_m^{(1)}(n_s k_0 r_1)}{-n_s^p J_m(n_l k_0 r_1) H_m^{(2)'}(n_s k_0 r_1) + n_l^p J_m'(n_l k_0 r_1) H_m^{(2)}(n_s k_0 r_1)}, \quad (2.27)$$

where k_0 must satisfy Eqs. 2.26 and 2.27 and is resonant with the capillary.

For tapered fiber optical coupling at the equator of the cavity, the optical field is mostly confined around the equator. Therefore, the situation can be treated as being the same as for a capillary. Thence, the theory discussed can be applied to an MBR.

Examples of the optical resonant field of an MBR are shown in Fig. 2.2. When not filled with an intracavity medium, the optical field is simply distributed on the silica

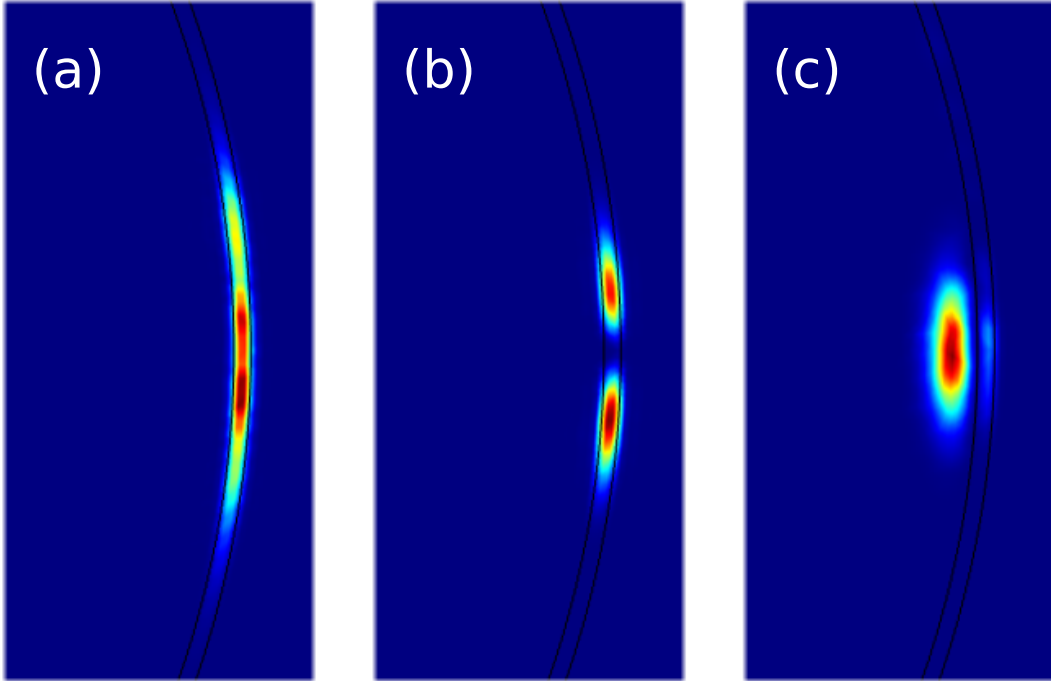


Figure 2.2: Simulated optical field of an MBR for different conditions. (a) The fundamental optical mode and (b) a higher order optical mode in an MBR. The intracavity and surrounding media are simply air. (c) The core of the MBR is filled with ethanol. The resonant optical field can be pushed into the core to form the *quasi-droplet* regime [24]. The simulation is done in COMSOL.

wall (Fig. 2.2(a)(b)). However, the refractive index of the core can be increased by filling a liquid into the cavity. In this regime, the resonant optical field can also be distributed in the core of the MBR and we call it the *quasi-droplet* regime [24] (see Fig. 2.2(c)).

2.4 Optical Coupling through a Waveguide

The input light is coupled to WGM cavities through the evanescent field of a waveguide, such as a prism [157], a polished optical fiber [158, 159], or a tapered optical fiber [160]. In this section, we introduce coupled-mode theory in order to describe the situation [151]. The change in the intracavity field over time is determined by

$$\frac{dA}{dt} = i\omega_0 A - \left(\frac{\gamma_{in}}{2} + \frac{\gamma_{ex}}{2}\right)A + \sqrt{\gamma_{ex}} s e^{i\omega_L t}, \quad (2.28)$$

where A is the unified intracavity electromagnetic field (so $|A|^2$ corresponds to the intracavity energy), ω_0 and ω_L are the resonant frequencies of the optical mode under analysis (which we term the *pump mode* in this thesis) and the input light, respectively,

γ_{in} and γ_{ex} are intrinsic and external decay rates, κ is a coefficient describing the optical tapered fiber coupling strength, and s is related to the degree of the input field power. This equation means that the time evolution of the amplitude of the intracavity field, da/dt , depends on the input field, s , and the decay rates, γ_{in} , due to the cavity loss, and γ_{ex} , due to the optical coupling.

2.4.1 Transmission Spectrum

Applying the rotating frame approximation, Eq. 2.28 transforms to

$$\frac{da}{dt} = i\Delta\omega_0 a - \left(\frac{\gamma_{in}}{2} + \frac{\gamma_{ex}}{2}\right)a + \sqrt{\gamma_{ex}}s, \quad (2.29)$$

where $a = Ae^{-i\omega_L t}$ and $\Delta\omega = \omega_0 - \omega_L$ represents the frequency detuning between the pump mode and the input laser light. This lead to a Lorentzian dip in the transmittance, T , which is given by

$$T = 1 - \frac{\gamma_{in}\gamma_{ex}}{(\gamma_{in} + \gamma_{ex})^2/4 + \Delta\omega^2} \quad (2.30)$$

$$= \frac{(\gamma_{in} - \gamma_{ex})^2/4 + \Delta\omega^2}{(\gamma_{in} + \gamma_{ex})^2/4 + \Delta\omega^2}. \quad (2.31)$$

Equation 2.31 can be used to describe signals collected from the output light while the input laser frequency is scanned. Depending on the degree of optical coupling, γ_{ex} , three regimes can be characterized, see Fig. 2.3 for illustrations.

Undercoupling: $\gamma_{ex} < \gamma_{in}$

The coupling is weak. The decay of the intracavity light field is mainly due to intrinsic loss in the cavity due to impurities and deformations. A large fraction of the pump light is not coupled into the cavity, but is transmitted through the waveguide.

Critical coupling: $\gamma_{ex} = \gamma_{in}$

When the intrinsic loss and the cavity loss due to the waveguide are equal to each other, destructive interference between the transmitted pump light and the π phase-shifted cavity leakage annihilate the transmission.

Over-coupling: $\gamma_{ex} > \gamma_{in}$

In addition to intrinsic losses in the cavity, a large fraction of light coupled to the cavity can be coupled back to the waveguide. This causes a relatively short photon lifetime in the cavity.

2.4.2 Q-Factor

To evaluate the cavity quality, the following definition of the Q-factor is widely used:

$$Q = 2\pi \frac{\text{Energy stored}}{\text{Energy loss in a cycle}}. \quad (2.32)$$

Suppose the energy damping rate is γ , i.e., $(\text{Energy stored}) \times \gamma = (\text{Energy loss})$, then

$$A(t) = A_0 e^{i\omega_0 - \frac{\gamma}{2}t}, \quad (2.33)$$

$$|A(t)|^2 = A_0^2 e^{-\gamma t}. \quad (2.34)$$

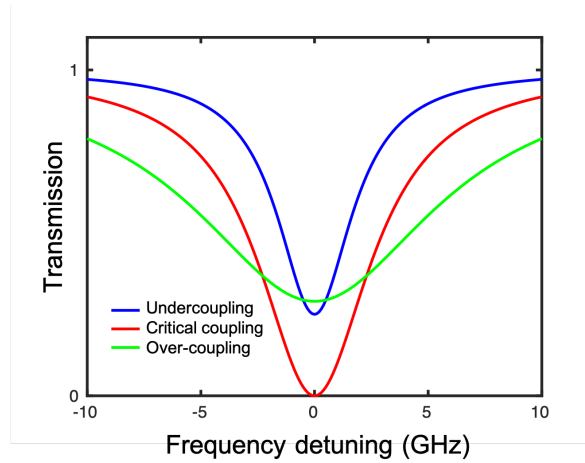


Figure 2.3: The transmission spectra for the three different coupling regimes.

The Fourier transform yields the energy stored as

$$|A(\omega)|^2 = \left| \int_{-\infty}^{\infty} A_0 e^{i\omega_0 t - \frac{\gamma}{2} t} e^{-i\omega t} dt \right|^2 \quad (2.35)$$

$$= \frac{A_0^2}{\gamma^2/4 + (\omega_0 - \omega)^2}. \quad (2.36)$$

Comparing this to the transmittance in Eq. 2.31, where we assume the same situation, we can view γ as corresponding to $\gamma_{in} + \gamma_{ex}$ and $\omega_0 - \omega$ is $\Delta\omega$. Then, Eq. 2.36 is proportional to the subtracted part as a dip in the signal. The full-width-at-half-maximum (FWHM) yields the damping rate, γ . Multiplying by the time period of one oscillation cycle, $1/f_0$, where f_0 is the resonant frequency, we obtain the quality factor of a resonant optical mode related to the FWHM:

$$Q = \frac{2\pi}{\gamma/f_0} = \frac{\omega_0}{\gamma}. \quad (2.37)$$

Note that, in common notation, $\Delta\omega$ is used instead of γ , but for consistency of the notation in this thesis, where $\Delta\omega$ is frequency detuning, we use γ .

2.5 Conclusion

In this chapter, we introduced some of the theory describing optical resonances and coupled-mode theory for WGM resonators. A function describing a resonant mode is chosen once the resonant value, k_0 , is obtained from the characteristic equation. Terms such as free spectral range (FSR) and the quality factor (Q-factor) have been introduced as they play important roles in later chapters. However, the term mode volume has not been explicitly introduced here, since it can have several different definitions so we will discuss this in later chapters. Generally speaking, a small mode volume indicates that the light field is confined in a small region and WGM cavities generally have small mode volume where strong light-matter interactions are invoked. Further discussion on this issue can be found in [142, 150, 157, 161].

Chapter 3

Experimental Methods

In this chapter, the standard experimental methods related to whispering gallery device fabrication for this thesis work will be discussed. This will include details on optical tapered optical fibers and different WGM geometries.

3.1 Tapered Optical Fiber Coupling System

Laser light is coupled into WGM cavities through the evanescent field of a waveguide. Amongst several coupling methods, such as prism coupling [157] and polished optical fiber coupling [158, 159], tapered optical fiber coupling [160] is believed to be the most efficient for coupling the laser light to the WGM cavities up to now. It has three major advantages compared to other coupling methods: (i) an optical mode can be selectively excited due to the thin fiber waist profile, (ii) the coupling strength is controllable by adjusting the gap between the tapered fiber and the WGM resonator, and (iii) the output information is transmitted during the coupling process and is easily collected by a detector. For our work, the tapered fiber is fabricated from a normal commercial optical fiber [162]. We use fibers with 125 μm cladding diameter, such as S630-FP single-mode fiber, 1550BHP single-mode fiber, or FG105LCA multimode fiber from Thorlabs, depending on the purpose. A stripped section of the optical fiber is placed on two pulling stages. The center of the stripped part is heated by a H:O flame while the custom-built fiber pulling rig tapers the fiber down to the desired thickness. During the pulling process, laser light is sent through the fiber and the transmittance is monitored. For our purposes, the thickness of the waist is usually around 1 μm .

During the pulling process, the region where the fiber is heated by the flame is called the hotzone. The easiest way of pulling the tapered fiber is to set the hotzone to have a constant value. While the pulling speed remains constant, the fraction of fiber in the hotzone get smaller during the process, thereby leading to an exponential decay of the fiber volume in the hotzone. The fiber thickness, as a function of the position in the tapered region, is also roughly following the exponential profile. Thus the method produces what is termed an exponential taper. For example, if we set the hotzone to be 3 mm, the pulling length is 33 mm to get $\sim 1 \mu\text{m}$ waist. With this method, more than 90% of transmittance can be achieved after the tapering process. However, it is also possible to explore other geometrical profiles for the tapered fiber.

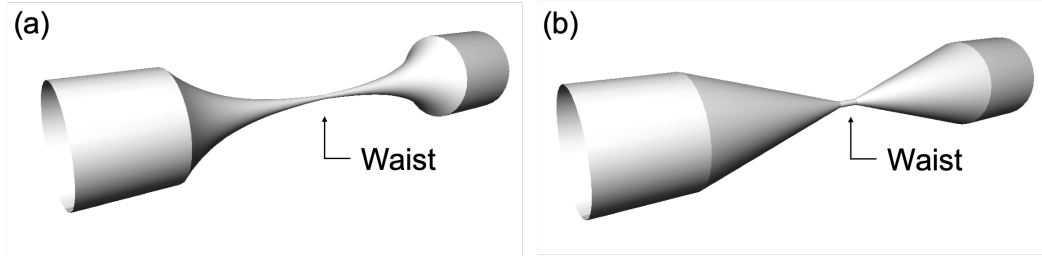


Figure 3.1: (a) Exponential tapered fiber; (b) Linear tapered fiber.

Light traveling through the tapered fiber can be scattered by a sudden change of the fiber diameter. The exponential tapered fiber has a relatively steep region in the thicker part where losses are created. To avoid such loss, tapered fibers with a linear decaying diameter have been developed [162, 163]. Linear tapered fibers have a waist region whose thickness is constant. The waist region is sandwiched between two regions linearly decaying toward the waist region (see Fig.3.1(b)). To fabricate such a fiber profile, the hotzone length varies during the pulling process - this can be computed [162] and submitted to the rig controlling program¹.

3.1.1 Transmission Spectrum and Q-Factor Measurement

After the tapered fiber fabrication, it is placed adjacent to a WGM cavity using nanopositioner stages. Laser light is sent through the tapered fiber and the transmitted light is collected on the other end using photodiodes, the type used depending on the purpose. For example, PDA10A-EC or DET10C photodiode detectors from Thorlabs can be used to detect laser light at 780 nm or 1550 nm, respectively. The 818-BB-35F detector from Newport has a short rise time of 25 ps so it can be used to measure transient light signal changes. Next, the information of the light intensity is transduced to voltage information and monitored on a digital storage oscilloscope (DSO, for example, the DSO5012A from Agilent Technologies). To observe the transmission spectrum through the fiber and find an optical mode in a WGM cavity, the laser frequency is scanned in a triangular wave across a few GHz using a function generator and a laser controller. We use the TLB-6712 and TLB-6728 diode lasers and their accompanying laser controllers connected with the 33250A arbitrary function generator from Aligent Technologies. To avoid thermal mode broadening effects [73], the laser power is kept low so the selected mode reveals its Lorentzian shape.

The optical Q-factor can be estimated by measuring the full-width-at-half-maximum (FWHM) of the Lorentzian transmission dip, see Fig. 3.2. While the transmission data is collected in the time domain is in agreement with the laser frequency scan, the FWHM in the time domain, Δt , can be transduced to the frequency domain, Δf , by scanning the frequency, F , (of the triangular wave), scanning the voltage peak-to-peak from the function generator, V_{pp} , and the ratio of the applied voltage to the laser frequency change, $\rho_{f/V}$, such that:

$$\Delta f = 2\rho_{f/V} \cdot V_{pp} \cdot F \cdot \Delta t. \quad (3.1)$$

¹This is a LabVIEW program developed by unit members over more than a decade.

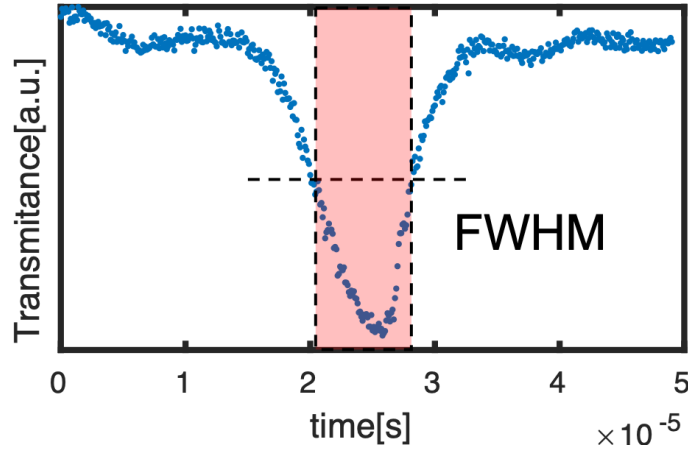


Figure 3.2: Plot of transmission through a tapered fiber as a function of laser frequency. The FWHM is used to determine the Q-factor.

The factor '2' in the equation is since we assume that scan back and forth takes the same time as the triangular wave scan. As shown in Section 2.4.2, Δf equals $\gamma/2$, the damping rate, divided by 2π and the Q-factor is obtained from $Q = f/\Delta f$, for a laser frequency, f . For example, in Fig. 3.2, Δt is $\sim 8 \mu\text{s}$; the scanning frequency, the scanning voltage, and the frequency-to-voltage ratio in this measurement are $F = 40$ Hz, $V_{pp} = 6$ V, and $\rho_{f/V} = (85 \text{ GHz})/(20 \text{ V})$. Thence, $\Delta f \sim 1.6 \text{ s}^{-1}$ and the Q-factor is $Q = 2.4 \times 10^8$, for a laser wavelength of 780 nm.

3.2 Whispering Gallery Mode Resonators

3.2.1 Silica Microspheres and Micropendulums

The microsphere can be viewed as the most fundamental geometry amongst WGM cavities. A high Q-factor of 10^8 was achieved in the early days [157] and, by now, the Q-factor is reaching the theoretical limit [6]. A silica microsphere is relatively easily fabricated by melting the tip of an optical fiber using a CO₂ laser (we used the 48-2 model from SYNRAD). The fabrication takes four steps (see Fig. 3.3): (i) Stick a weight on the tip of a segment of fiber and set it vertically; (ii) use a CO₂ laser to melt the fiber so that the weight pulls the fiber to form a thin stem that sustains the microsphere; (iii) high power CO₂ laser light is applied to cut off the weighted part, leaving a fragment of the fiber; (iv) the fragment is melted by the CO₂ laser so the surface tension of the silica forms a spherical shape. The laser power of the CO₂ depends on the focus condition and can be optimized according to personal preference. For example, we use a ZnSe lens with a focal length ~ 60 mm. When the fiber length is ~ 70 mm, ~ 2.5 W is used for pulling the stem, ~ 5 W is used to cut the weight, and ~ 4 W is used for finally making the sphere. A fabricated silica microsphere is shown in Fig. 3.4(a).

A micropendulum is a microsphere with an ultrathin stem of diameter around 2 μm , so the stem can oscillate [86]. To make such a thin stem, the focus of the CO₂

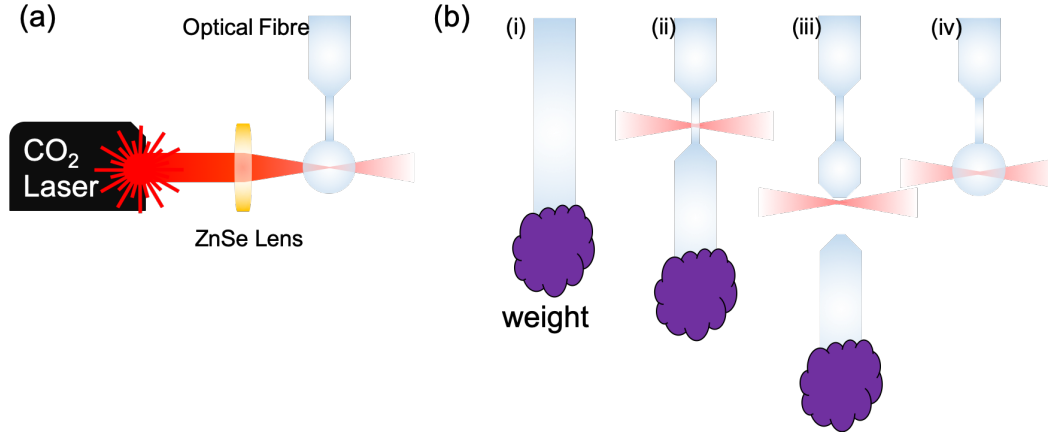


Figure 3.3: Microsphere and micropendulum fabrication process. (a) The sphere fabrication setup. The focal length of the ZnSe lens is ~ 60 mm. (b) A optical fiber is melted and transformed to a microsphere or a micropendulum by following step (i) to (iv).

laser needs to be well adjusted. An off-focus CO₂ laser can only make a thick stem, while a focused laser can easily cut the stem. Empirically, the lower bound of the stem diameter depends on the focus of the laser. This means that if the focus is well adjusted, one can always fabricate a smooth thin stem. Due to such a thin stem, the pressure of the CO₂ laser beam can push the position of the fiber fragment out of the focus. The fragment vibrates between the in and out of focus area of the laser, slowly melting and reaching a spherical shape. A fabricated silica micropendulum is shown in Fig. 3.4(b).

3.2.2 Silica Microbottle and Microbubble Fabrication

A microbottle resonator is a unique WGM cavity since the resonant field is widely distributed over its 2D surface [15]. The condition for the free spectral range (FSR) is different than for other WGM cavities; thus, the zero dispersion regime resides in shorter wavelengths than for conventional WGM cavities [120]. Another unique geometry is the microbubble resonator [10]. The resonant frequency of the microbubble can be tuned by applying internal air pressure. Microbubbles have been used as a platform for sensing applications [11–13]. However, as we will see in Chapters 5 and 7, they can also be used to excite supermodes of coupled resonators and to generate frequency combs.

Both microbottles and microbubbles can be fabricated in a similar way using a silica capillary. The fabrication setup includes two pulling stages to taper the capillary, a CO₂ laser, a 50:50 ZnSe beam splitter, three mirrors² and two ZnSe lenses. The CO₂ laser is split into two beams by a 50:50 ZnSe beam splitter and both beams are reflected off of mirrors so that they are counter-propagating at the center of the pulling stages (see Fig. 3.5(a)). We use two types of silica capillary for the work in this thesis, TSP250350 and TSP100375, both from Molex. TSP250350 has an inner/outer

²Mirrors made from copper, silicon, or molybdenum can be used.

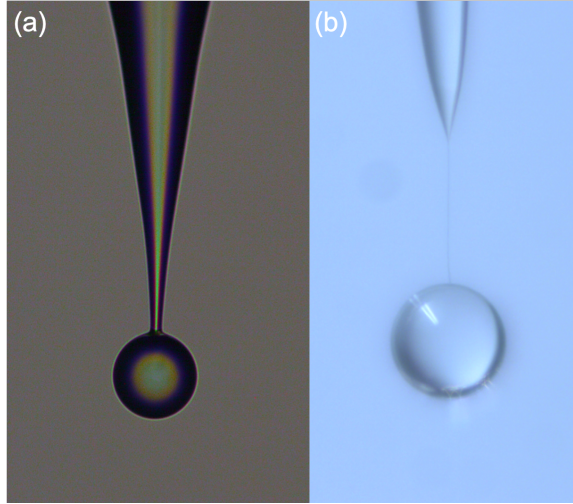


Figure 3.4: Fabricated microsphere (a) and micropendulum (b). The typical diameter of a microsphere fabricated in our laboratory ranges from $40\ \mu\text{m}$ to $200\ \mu\text{m}$. The typical diameter of a micropendulum diameter ranges from $80\ \mu\text{m}$ to $120\ \mu\text{m}$, with a stem length and stem thickness from $100\ \mu\text{m}$ to $500\ \mu\text{m}$ and $1\ \mu\text{m}$ to $3\ \mu\text{m}$, respectively.

diameter of $250/350\ \mu\text{m}$ and TSP100375 has an inner/outer diameter of $100/375\ \mu\text{m}$. The capillary is tapered to tens of μm , depending on the required dimensions of the bubble, using a CO_2 laser and a pulling stage setup. High pressure N_2 gas is inserted through one end of the capillary. By applying a counter-propagating CO_2 laser again to the tapered part, the capillary melts and expands due to the applied inner air pressure, see Fig. 3.5(b). To manage the bubble or bottle dimensions, the CO_2 laser power is finely adjusted while the process is monitored on a CCD camera. Once the capillary is tapered, several bubbles or bottles can be made on the tapered region. We show a fabricated microbubble and microbottle in Fig. 3.6.

The bubble wall thickness, Δr , is roughly estimated from the bubble diameter, r , the inner diameter, r_{in} , and the outer diameter, r_{out} , of the tapered capillary:

$$\Delta r = r - \sqrt{r^2 - (r_{out}^2 - r_{in}^2)}. \quad (3.2)$$

We assume that the ratio of the inner to outer diameter stays the same after tapering³ (e.g., for TSP250350 $r_{in} = (250/350)r_{out}$). Hence, the inner diameter after pulling can be estimated by the ratio and the outer diameter can be measured using an optical microscope. Bubbles are relatively easier to fabricate with TSP250350. With TSP100375, the bubble is closer to spherical shape. However, we need to use a higher applied air pressure to expand the bubble, otherwise the tapered capillary would shrink due to surface tension. This makes it harder to control the bubble diameter. The empirical smallest diameter of a bubble or bottle by this method is around $10\ \mu\text{m}$, as it is thought to be the limit given by the CO_2 laser with a wavelength of $10.6\ \mu\text{m}$. Microbubbles or

³The same profile as for a tapered fiber should roughly be applied to the capillary [163]. Even the normal component of the pulling force, that is canceled when pulling a fiber, is not canceled in the case of the capillary; however, as the adiabatic condition is satisfied, the effect should be negligible.

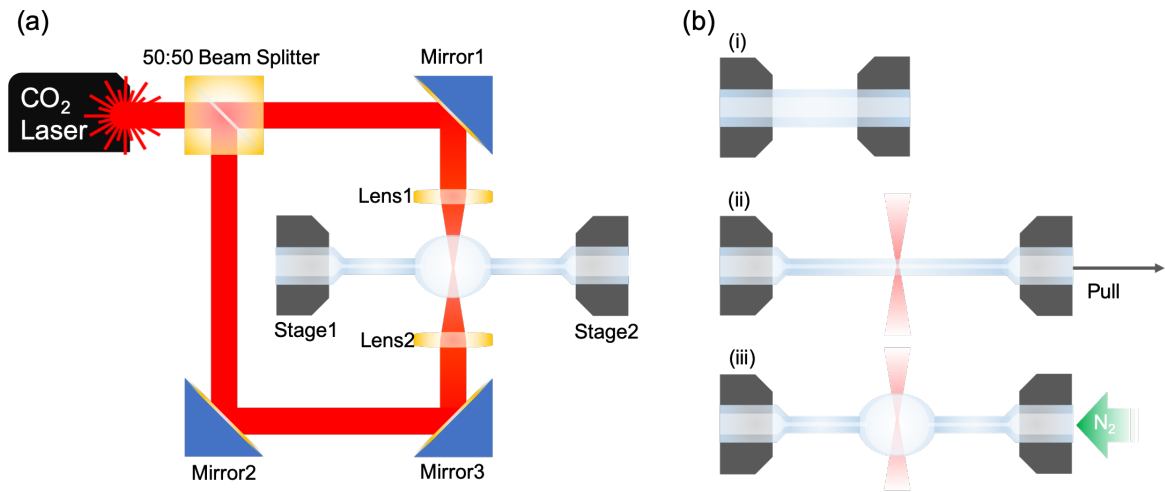


Figure 3.5: Microbubble and microbottle fabrication process. (a) The setup with CO_2 laser for the fabrication. (b) A microbubble and a microbottle fabricated from a tapered silica capillary following steps (i) to (iii).

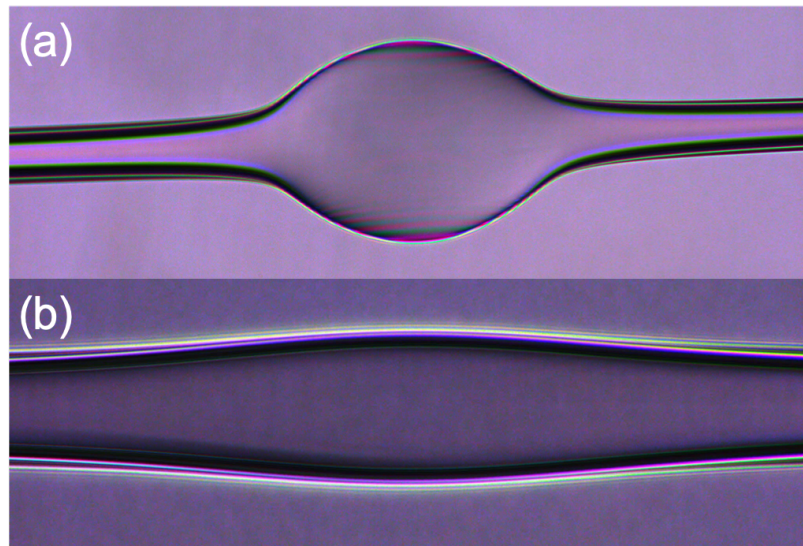


Figure 3.6: Fabricated microbubble (a) and microbottle resonator (b). The diameter of a microbubble resonator fabricated in our setup ranges from $100 \mu\text{m}$ to $200 \mu\text{m}$ and the wall thickness is between $0.5 \mu\text{m}$ to $2 \mu\text{m}$. The typical diameter of a microbottle resonator is between $30 \mu\text{m}$ and $120 \mu\text{m}$.

microbottles with smaller diameters have not been achieved. The wall thickness of the microbubble can be as little as $0.5 \mu\text{m}$, while the Q-factor can be as high as 10^7 [13].

3.2.3 Microtoroid Fabrication⁴

A microtoroid resonator is a widely used WGM resonator. It is sometimes preferred due to its small mode volume, clean transmission spectrum, and ultra-high Q of 10^8 [8, 9, 22, 43, 164]. The microtoroids that were used were fabricated on a silicon wafer covered by 1-2 μm of a silica layer. The fabrication process has eight steps (see Fig. 3.7). (i) Firstly, the well-cleaned silica surface of the wafer is spin-coated by HDMS (Hexamethyldisilazane) to promote surface adhesion; (ii) Photoresist (SHIPLEY 1813) is spin-coated for photolithography and the solvent is evaporated and removed by baking the wafer at 115°C for one minute; (iii) In the photolithography step, the wafer is exposed to a UV ramp with a mask with arrays of disks printed; (iv) The exposed part of the photo resist is washed off in developer (MIF-319); (v) After cleaning the developer, HF etching is executed to remove silica other than the disk part. HF needs specific handling - gloves and safety mask are mandatory. A TEFLON container and tweezers are used and the etching must be done in a ventilated environment; (vi) The HF and mask are cleaned; (vii) The wafer is exposed to XeF_2 etching. In this step, the silica microdisk is etched out from the silicon substrate. A chamber is filled with XeF_2 and the pressure is set to 3 Torr. Every two minutes, impure gas with by-products (i.e., Xe and SiF_4) are replaced with clean XeF_2 . The total etching takes 6 hours; (viii) Finally, a CO_2 laser irradiates each microdisk. The rough edge of the disk is melted to form a smooth toroidal shape.

3.3 Conclusion

In this chapter, we introduced the tapered fiber optical coupling method and fabrication methods to make microspheres, micropendulums, microbubbles, microbottles, and microtoroids. This will help the reader to understand the experiments conducted in later chapters. Although only microspheres and microbubbles are used for the work in the following chapters, other geometries are also considered for further studies.

⁴This fabrication method was done in the Micro/Nano Photonics Laboratory, Department of Electrical and Systems Engineering, Washington University in St. Louis, USA during a 3-month research visit.

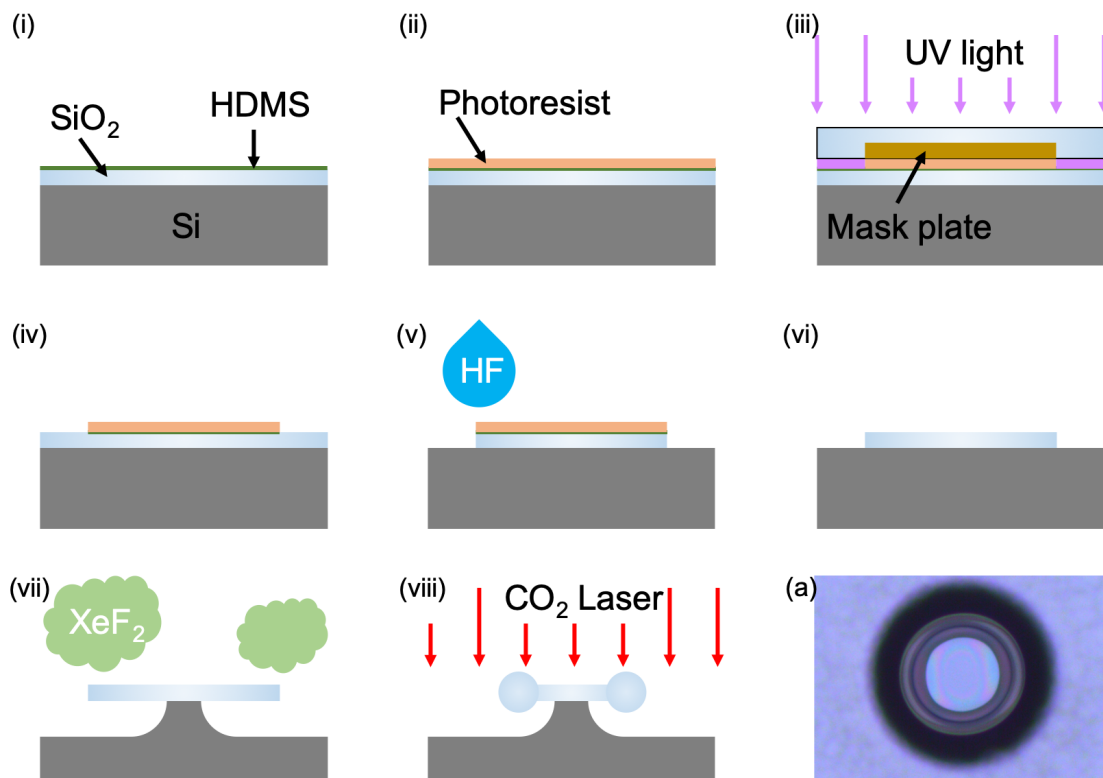


Figure 3.7: Microtoroid fabrication process is illustrated in panels (i)-(viii). Panel (a) shows a fabricated microtoroid resonator. A microtoroid is fabricated from a silica-silicon wafer by photolithography. The diameter of the toroids are typically $100\ \mu\text{m}$ and the minor diameter is $10\ \mu\text{m}$ depend on the mask plate and XeF₂ etching time.

Chapter 4

Cavity Ring-Up Spectroscopy¹

4.1 Introduction

Whispering gallery mode (WGM) resonators are widely used for a number of applications, one of which is sensing [41, 58]. As mentioned in Chapter 1, to measure transient phenomena, e.g. a chemical reaction near a WGM cavity, cavity ring-up spectroscopy (CRUS) based transient sensing could be used [69]. Examples of events that could rely on such sensing techniques include biochemical phenomena in a liquid solvent. For such quick processes in fluids, the microbubble resonator is clearly a suitable platform - the solvent can be inserted into the cavity and stable optical coupling can be achieved from the outside. In this case, the Q-factor of the liquid core cavity can be around 10^6 [24]. Therefore, a method of investigating the transient response to a perturbation in a low Q cavity is an important step towards liquid core, MBR transient sensing. As an MBR is a relatively complicated system, in this work we have investigated CRUS first in a microsphere as a test-bed for later developing a transient sensing technique with an MBR. In this chapter, we provide a theory, developed from coupled-mode theory, to describe CRUS in a high Q WGM resonator. We assume that CRUS is obtained by sending a rectangular pulse with a rising time of $\sim 1 \times 10^{-9}$ s. Numerical simulations are performed to verify the theory and to predict the response to the change of the resonance condition in a low Q cavity. Experimental work verifies the theory and numerical simulations in a high Q cavity and some indication of the process in a low Q cavity is also presented.

4.2 Coupled-Mode Theory

A typical CRUS setup is shown in Fig. 4.1(a). The WGR is coupled evanescently to a tapered optical fiber through which light from a laser propagates. The light

¹This work is published in Y. Yang, R. Madugani, S. Kasumie, J. M. Ward, and S. Nic Chormaic, "Cavity ring-up spectroscopy for dissipative and dispersive sensing in a whispering gallery mode resonator", *Appl. Phys. B* **122**, 291 (2016) and as a chapter in: D. Meschede, T. Udem and T. Esslinger (eds) "Exploring the World with the Laser", Springer, Cham (2018) [77, 165]. S. Kasumie contributed to the numerical simulations of the model and writing the manuscript. Later, S. Kasumie found an analytical solution for the given model as contained herein.

couples into the resonator and is monitored at the opposite end of the fiber. The coupling dynamics can be described using coupled-mode theory. The amplitude of the intracavity electromagnetic field, $A(t)$, changes in time according to the following [70, 166, 167]

$$\frac{dA(t)}{dt} = i\omega_0 A(t) - \left(\frac{\gamma_{in}}{2} + \frac{\gamma_{ex}}{2}\right)A(t) + \sqrt{\gamma_{ex}}S_{in}(t), \quad (4.1)$$

where $i = \sqrt{-1}$, the resonant frequency of the WGM is ω_0 , and γ_{ex} and γ_{in} represent the external and intrinsic coupling rates, respectively. The total damping rate of the cavity is given by $\gamma = \gamma_{ex} + \gamma_{in}$ and $\tau = 2\pi/\gamma$ is the intracavity lifetime. In order to arrive at the transient response of the WGR, the laser light is pulsed with a temporal profile, $S_{in}(t)$. The laser frequency, ω_L , is far detuned, i.e., $\omega_L - \omega_0 \gg \gamma$. The pulsed input field can be separated into a slowly varying and a fast varying term so that

$$S_{in}(t) = s_{in}(t)e^{-i\omega_L t}. \quad (4.2)$$

Here, the slowly varying part, $s_{in}(t)$, represents the temporal profile of the pulse and, in the following discussions, it takes the form of a Gaussian function where

$$s_{in}(t) = \begin{cases} 0, & t < t_0 \\ \alpha_{in} \exp\left(-\frac{4[t - t_0 - t_r]^2}{\ln 2 \cdot t_r^2}\right), & t_0 < t < t_0 + t_r \\ \alpha_{in}, & t > t_0 + t_r. \end{cases} \quad (4.3)$$

The pulse is illustrated in Fig. 4.1(b). The pulse starts at time t_0 and follows a Gaussian profile with a rise time, $t_r \ll \tau$. At time $t = t_0 + t_r$, the total power of the pulse reaches its maximum, $|\alpha_{in}|^2$, and, for later times, the laser can be treated as a continuous light source over the lifetime of the cavity mode.

4.2.1 A Simple Model: Large Spectral Broadening Bandwidth

The temporal profile of $S_{in}(t)$ can be obtained from Eq. 4.2 and Eq. 4.3 and Fourier expanded by $e^{i\omega t}$ as follows:

$$S_{in}(t) = \begin{cases} 0, & t < t_0 \\ \sqrt{\frac{\ln 2}{\pi}} \frac{t_r \alpha_{in}}{4} \int_{-\infty}^{+\infty} e^{-\frac{\ln 2 t_r^2 (\omega_L - \omega)^2}{16}} e^{i[(\omega_L - \omega)(t - t_0 - t_r)]} d\omega, & t_0 < t < t_0 + t_r \\ \alpha_{in} e^{-i\omega_L t}, & t > t_0 + t_r. \end{cases} \quad (4.4)$$

It can be seen that, for a time interval, $t \in [t_0, t_0 + t_r]$, the rise time of the pulse induces sideband frequencies even though the laser source is monochromatic. As the Fourier transform of a Gaussian function is a Gaussian, the laser pulse is expanded transiently with a bandwidth, $B \sim 1/t_r$.

In our experiments, the pulse has a rise time ranging from several tens of ps to ~ 1 ns. The laser frequency broadening bandwidth, B , is of the order of GHz, and, for a WGM with $Q > 10^7$, $\gamma \sim$ MHz. As $B \gg \gamma$, we can assume that only the portion of the broadened laser source at the resonant frequency, ω_0 , can be efficiently coupled to

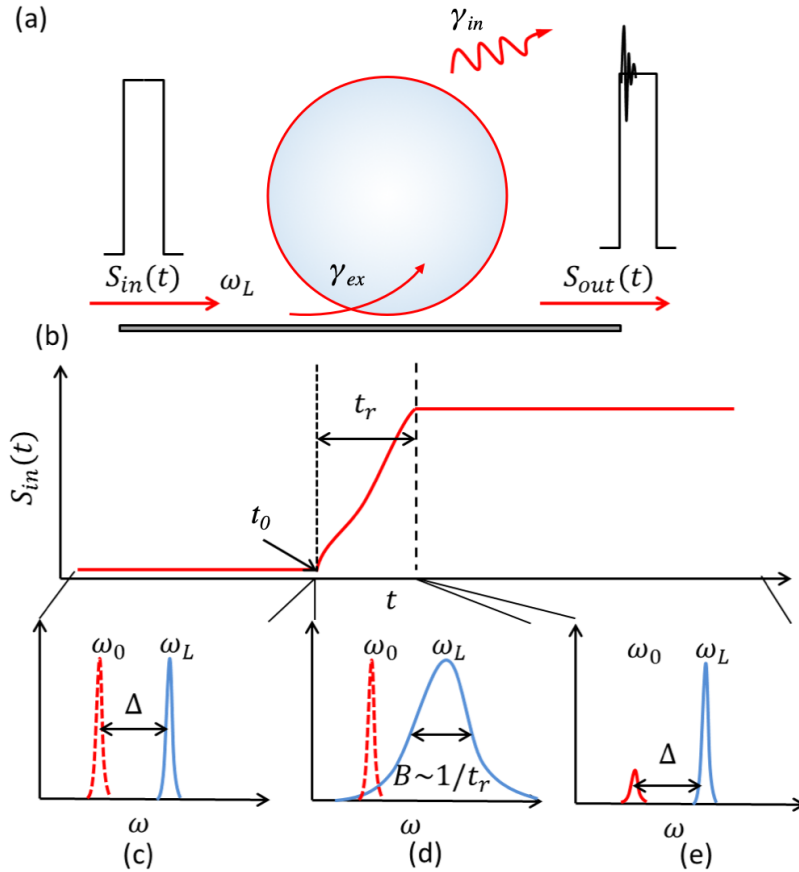


Figure 4.1: (a) Schematic of a taper coupled WGR system for transient sensing using CRUS. A pump laser of frequency ω_L , far off resonance with the WGM, ω_0 , is coupled through the tapered fiber with a temporal profile, $S_{in}(t)$. The pulse profile is depicted in (b); the laser pulse starts at a time t_0 and rises up to its maximum within a time t_r . The mathematical description of the pulse is given in Eq. (4.3). (c)-(e) Transient frequency of the laser pulse for different time intervals. (c): $t = [0, t_0]$; (d): $t = [t_0, t_0 + t_r]$; (e): $t = [t_0 + t_r, +\infty)$. At the rising edge of the pulse, the laser source is transiently broadened (d), so a fraction of the pump signal couples to the WGM and contributes to a beat signal between it and the pump source (e).

the WGM, as illustrated in Fig. 4.1(c)-(e). The WGM acts as an infinitely narrow, bandpass filter so that we only need to consider the frequency at ω_0 , see Fig. 4.1(d). This gives an intuitive explanation of how light is coupled to the cavity during the ringing period.

4.2.2 Analytical Solution

To analytically solve the given model, we can start from a useful mathematical formula:

$$\frac{da(t)}{dt} + \Omega a(t) = e^{-\Omega t} \frac{d}{dt} (a(t)e^{\Omega t}). \quad (4.5)$$

In a rotating frame, we define $a(t) = A(t)e^{i\omega_L t}$ and $\Omega = i\Delta\omega + \gamma/2$. Also, for simplicity, we shift $t = t_0 + tr$ to $t = 0$ in this section. Then the transformation of the coupled-mode equation follows:

$$\frac{da(t)}{dt} = -\Omega a(t) + \sqrt{\gamma_{ex}} s_{in}(t) \quad (4.6)$$

$$\frac{da(t)}{dt} + \Omega a(t) = e^{-\Omega t} \frac{d}{dt} (a(t)e^{\Omega t}) = \sqrt{\gamma_{ex}} s_{in}(t) \quad (4.7)$$

$$\frac{d}{dt} (a(t)e^{\Omega t}) = \sqrt{\gamma_{ex}} s_{in}(t)e^{\Omega t}. \quad (4.8)$$

At this stage, both sides of Eq. 4.8 can be integrated. This needs to be done step-by-step so that the effect of the ringing up survives after integration. For $t < 0$ (i.e., in the model, Eq. (4.3), this corresponds to $t < t_0 + t_r$), the integration of the left term is

$$\int_{-\infty}^0 \frac{d}{dt} (a(t)e^{\Omega t}) dt = a(0). \quad (4.9)$$

As there is no intracavity light field for $t = -\infty$, we choose $a(-\infty) = 0$. In the proposed model and in actual experimental conditions, there is no input field before t_0 ; however, we extend the Gaussian input profile to $-\infty < t < t_0$, so that integration is possible and can be evaluated. This does not change the essence of the method. The

right term can be integrated²:

$$\sqrt{\gamma_{ex}} \int_{-\infty}^0 s_{in}(t) e^{\Omega t} dt = \alpha_{in} \sqrt{\gamma_{ex}} \int_{-\infty}^0 e^{-\beta t^2} e^{\Omega t} dt \quad (4.10)$$

$$\simeq \alpha_{in} \sqrt{\gamma_{ex}} \int_{-\infty}^0 (1 + \Omega t) e^{-\beta t^2} dt \quad (4.11)$$

$$= \frac{\alpha_{in} \sqrt{\gamma_{ex}}}{2} \left(\sqrt{\frac{\pi}{\beta}} - \frac{\Omega}{\beta} \right). \quad (4.12)$$

Here, $\beta \equiv 4/(\ln 2 \cdot t_r^2)$. The approximation in Eq. 4.11 is valid when $|\Omega|$ is sufficiently smaller than $1/t_r$. However, when Q is low or when the detuning is large, the expansion is not valid. Let us suppose that $|\Omega| \ll 1/t_r$.

Now we move to $t > 0$ (i.e., $t > t_0 + t_r$ in Eq. 4.3). The left term of Eq. 4.8 is integrated to yield:

$$\int_0^t \frac{d}{dt'} (a(t') e^{\Omega t'}) dt' = a(t) e^{\Omega t} - a(0), \quad (4.13)$$

and the right term is:

$$\sqrt{\gamma_{ex}} \int_0^t s_{in}(t') e^{\Omega t'} dt' = \alpha_{in} \sqrt{\gamma_{ex}} \int_0^t e^{\Omega t'} dt' \quad (4.14)$$

$$= \alpha_{in} \sqrt{\gamma_{ex}} \left(\frac{e^{\Omega t'}}{\Omega} \Big|_{t'=t} - \frac{e^{\Omega t'}}{\Omega} \Big|_{t'=0} \right) \quad (4.15)$$

$$= \frac{\alpha_{in} \sqrt{\gamma_{ex}}}{\Omega} (e^{\Omega t} - 1). \quad (4.16)$$

An important feature appears in Eq. 4.15. The value of the integrated function at $t = 0$ (i.e., the second term) does not correspond to what was obtained in the rising pump integration (see Eq. 4.12). In the steady state, this term was canceled out for the steady intracavity field, $a(0)$. However, if we suppose the time dependence of the intracavity field is continuous, $a(0)$ in Eq. 4.13 and Eq. 4.9 must correspond to each other and can be canceled out by adding together:

$$\int_{-\infty}^t \frac{d}{dt'} (a(t') e^{\Omega t'}) dt' = \int_{-\infty}^0 \frac{d}{dt'} (a(t') e^{\Omega t'}) dt' + \int_0^t \frac{d}{dt'} (a(t') e^{\Omega t'}) dt' \quad (4.17)$$

$$= a(t) e^{\Omega t}. \quad (4.18)$$

²It is also possible to obtain the integration of higher orders of the expansion, as follows:

$$\begin{aligned} \int_{-\infty}^0 e^{-\beta t^2} e^{\Omega t} dt &= \int_{-\infty}^0 e^{-\beta t^2} \left(1 + \Omega t + \frac{\Omega^2 t^2}{2!} + \frac{\Omega^3 t^3}{3!} + \dots \right) dt \\ \int_{-\infty}^0 e^{-\beta t^2} t^{2m} dt &= \frac{\partial^m}{\partial \beta^m} \int_{-\infty}^0 e^{-\beta t^2} dt = \frac{\partial^m}{\partial \beta^m} \frac{1}{2} \sqrt{\frac{\pi}{\beta}} \\ \int_{-\infty}^0 e^{-\beta t^2} t^{2m+1} dt &= \frac{\partial^m}{\partial \beta^m} \int_{-\infty}^0 t e^{-\beta t^2} dt = \frac{\partial^m}{\partial \beta^m} \int_{-\infty}^0 \frac{d}{dt} \left(\frac{e^{-\beta t^2}}{2\beta} \right) dt = \frac{\partial^m}{\partial \beta^m} \left(-\frac{1}{2\beta} \right). \end{aligned}$$

We can also equate the right-hand side terms:

$$\sqrt{\gamma_{ex}} \int_{-\infty}^t s_{in}(t) e^{\Omega t} dt \simeq \alpha_{in} \sqrt{\gamma_{ex}} \left(\frac{1}{2} \sqrt{\frac{\pi}{\beta}} - \frac{\Omega}{2\beta} + \frac{e^{\Omega t} - 1}{\Omega} \right) \quad (4.19)$$

$$\equiv \frac{\alpha_{in} \sqrt{\gamma_{ex}}}{\Omega} (e^{\Omega t} - I), \quad (4.20)$$

with

$$I \equiv 1 - \frac{\Omega}{2} \sqrt{\frac{\pi}{\beta}} + \frac{\Omega^2}{2\beta}. \quad (4.21)$$

One may also include higher orders of the integration into I . As long as $|\Omega| \ll 1/t_r$ is satisfied, higher order integration is negligible. The form of the rising up input signal is not really important in reality. Experimentally, the rising up signal will always have an error; however, the experimental results do not largely depend on the error. Therefore, one can always suppose an integrable function similar to the Gaussian during the rising up period, to build a valid theory. In this case, the integration term is also included in I .

Finally, the intracavity field is obtained as:

$$a(t) = \frac{\alpha_{in} \sqrt{\gamma_{ex}}}{\Omega} (1 - I e^{-\Omega t}). \quad (4.22)$$

Now, as discussed above, the second term in Eq. 4.15, while normally canceled out in a steady state, remains. From a mathematical point of view, this is the critical reason of the transient transmission vibration phenomenon in CRUS in the given model.

The output signal, $s_{out}(t)$, can be calculated using the input-output relationship [151]:

$$s_{out}(t) = -s_{in}(t) + \sqrt{\gamma_{ex}} a(t). \quad (4.23)$$

Here, we are interested in the output signal after the pulse reaches its maximum value. In the rotating frame, this is just α_{in} . The transient transmission is obtained as:

$$T(t) = \left| \frac{s_{out}}{s_{in}} \right|^2 = \left| \frac{\gamma_{ex}}{\Omega} - 1 - \frac{\gamma_{ex}}{\Omega} I e^{-\Omega t} \right|^2 \quad (4.24)$$

$$\simeq \frac{4\Delta\omega^2 + \gamma'^2}{4\Delta\omega^2 + \gamma^2} + \frac{4\gamma_{ex}^2 |I|^2 e^{-\gamma t}}{4\Delta\omega^2 + \gamma^2} + \frac{4\gamma_{ex} |I| e^{-\gamma t/2}}{4\Delta\omega^2 + \gamma^2} \{ \gamma' \cos(\Delta\omega t) - 2\Delta\omega \sin(\Delta\omega t) \}, \quad (4.25)$$

with $\gamma' = \gamma_{in} - \gamma_{ex}$. The first term is the normal Lorentzian transmission dip. The second term shows there is an additional nonbeating signal from the intracavity field. The third term is the transient beating signal or ringing effect in CRUS. The beating frequency is given by the frequency detuning, $\Delta\omega$. As the cavity leaves the CRUS phase and moves to an equilibrium state, the signal components described in the second term and then the third term fade out. A typical wave form is plotted in Fig. 4.2(a).

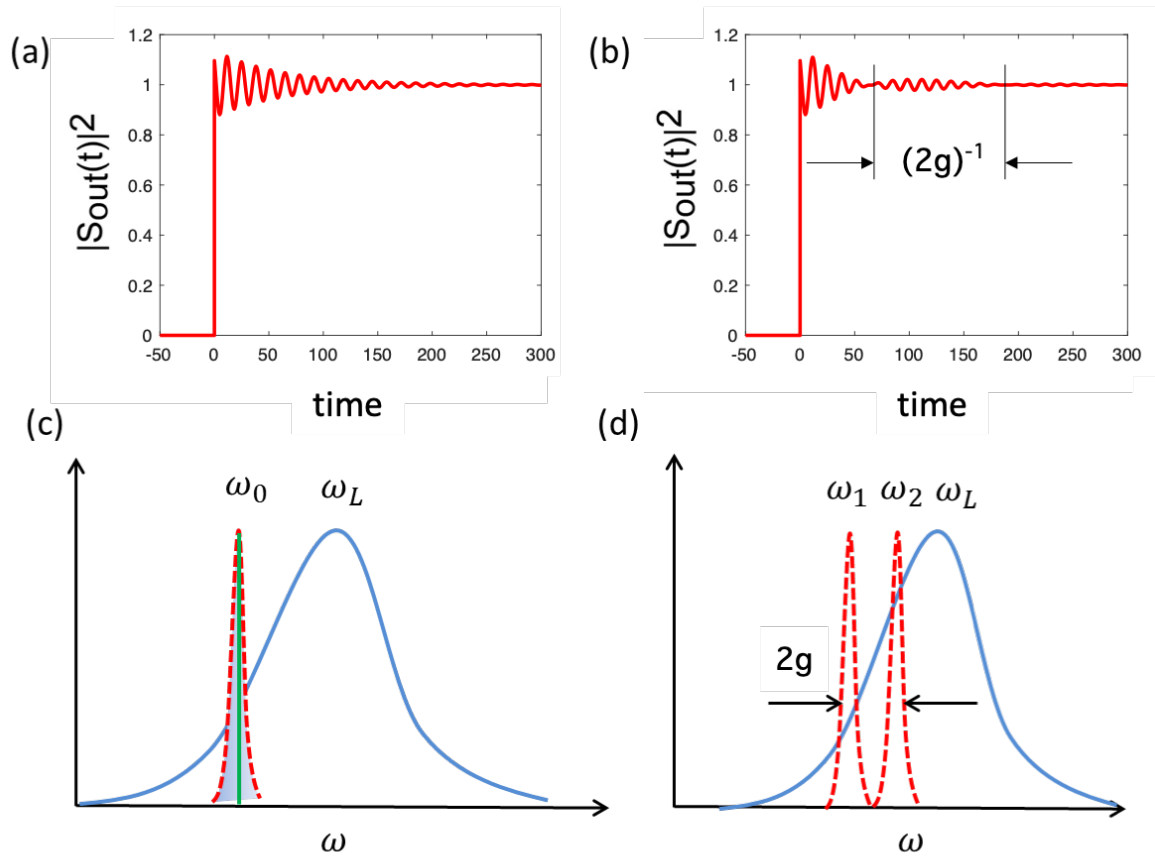


Figure 4.2: (a). A typical CRUS signal. The beating happens according to the second term and third term of Eq.(4.24). This is due to the frequency broadening at the rising edge of the input signal. We can treat the WGM as an ultra-narrow filter; therefore, only the on-resonance, $\omega = \omega_0$, component in the broadened pump laser signal can be stored in the WGM as shown in (c). (b) The CRUS signal when there is modal coupling with coupling strength, g . The beating is modulated by a trigonometric envelope of period $(2g)^{-1}$. (d) On the other hand, the modulation also happens when there are two cavity modes separated by $2g$.

4.2.3 The Mode Mixing Case

In practice, multiple WGM resonances may fall within the transient spectral broadening bandwidth. In the following, the case in which two modes mix will be investigated. There are two different types of mode mixing that we consider. The first situation is that where two modes exist quite close to each other in the spectrum. In the following discussion, we assume that both modes lie within the transiently broadened spectrum bandwidth, B , while satisfying the narrow bandpass filter approximation made in Sec. 4.2.1. Defining the two modes as ω_1 and ω_2 , with a separation between them of δ , the coupled-mode equations for each mode are given by

$$\frac{dA_i}{dt} = i\omega_i A_i(t) - \frac{\gamma_{in,i} + \gamma_{ex,i}}{2} A_i(t) + \sqrt{\gamma_{ex}} S_{in,i}(t) e^{-i\omega_L t}, \quad (4.26)$$

where $i = 1, 2$ and represents the two modes. Since there is no spectral overlap of the two modes, the mode equations are decoupled and can be solved separately. This yields the same expressions as in Eq. 4.24 and each mode beats with $S_{in}(t)$ separately. The total beating signal, $T_b(t)$, is simply:

$$T_b(t) = \sum_{i=1,2} T_{i,b}(t) \quad (4.27)$$

$$= \sum_{i=1,2} \frac{4\gamma_{ex,i} |I_i| e^{-\gamma_i t/2}}{4\Delta\omega_i^2 + \gamma_i^2} \{ \gamma'_i \cos(\Delta\omega_i t) - 2\Delta\omega_i \sin(\Delta\omega_i t) \}. \quad (4.28)$$

$T_b(t)$ is a linear combination of the two individual beat signals. The amplitudes of the signals with different frequencies are determined from the detunings, $\Delta\omega_i$, of the resonances relative to the laser source. If δ is large, then one of the beat signals will be much larger than the other since the $\Delta\omega_i$ in the denominator are different. In this case, the weaker signal can be ignored. In contrast, if the two modes are similar to each other so that $\delta \ll \Delta\omega_i$ and $\gamma_1 \simeq \gamma_2 = \gamma$ then, for simplicity, we set $\Delta\omega_1 \approx \Delta\omega_2 = \Delta\omega$ and the coupling rates, $\gamma_{ex,i}$, are approximately equal. From Eq. 4.28, the total beat signal, $T_b(t)$, is:

$$T_b(t) \simeq \frac{4\gamma_{ex} |I| e^{-\gamma t/2}}{4\Delta\omega^2 + \gamma^2} [(1 + \cos(\delta t)) \{ \gamma' \cos(\Delta\omega t) - 2\Delta\omega \sin(\Delta\omega t) \} - \sin(\delta t) \{ \gamma' \sin(\Delta\omega t) + 2\Delta\omega \cos(\Delta\omega t) \}]. \quad (4.29)$$

The expression is complex, however, we are able to read the beating frequency of δ .

The other possible case to consider is that where the two modes are coupled. This is often the case in traveling wave resonators, such as WGRs. Degenerate modes in the resonator represent clockwise and counter-clockwise propagation. Due to scattering along the propagation path, the two modes can indirectly couple to each other; this effect is called modal coupling and leads to normal mode splitting [168, 169]. Here, we define a modal coupling strength, g , and the coupled-mode equations for the two modes are given by a_{cw} and a_{ccw} , representing the two opposing propagation directions.

The two coupled-mode equations can be written as

$$\begin{aligned}\frac{dA_{cw}}{dt} &= i\omega_0 A_{cw}(t) - \frac{\gamma_{in} + \gamma_{ex}}{2} A_{cw}(t) - igA_{ccw}(t) + \sqrt{\gamma_{ex}} S_{in}(t); \\ \frac{dA_{ccw}}{dt} &= i\omega_0 A_{ccw}(t) - \frac{\gamma_{in} + \gamma_{ex}}{2} A_{ccw}(t) - igA_{cw}(t).\end{aligned}\quad (4.30)$$

The two modes should have the same values of γ_{in}, γ_{ex} and detuning. By letting $A_1(t) = A_{cw}(t) + A_{ccw}(t)$ and $A_2(t) = A_{cw}(t) - A_{ccw}(t)$, these two equations can be transformed into two uncoupled equations [169]:

$$\begin{aligned}\frac{dA_1(t)}{dt} &= i(\omega_0 - g)A_1(t) - \frac{\gamma_{in} + \gamma_{ex}}{2} A_1(t) + \sqrt{2\kappa_e} S_{in}(t) \\ \frac{dA_2(t)}{dt} &= i(\omega_0 + g)A_2(t) - \frac{\gamma_{in} + \gamma_{ex}}{2} A_2(t) + \sqrt{2\kappa_e} S_{in}(t).\end{aligned}\quad (4.31)$$

Here, the original two traveling modes generate two equivalent standing wave modes with frequency shifts, $\pm g$, as illustrated in Fig. 4.2(d). Usually, the modal coupling strength is in the MHz range for silica WGRs, i.e., the frequencies of the two standing waves are quite close to each other. Since $B \gg 2g$, we can assume that the two modes have the same transient components at the rising edge time, as in the previous case. Also, in the actual experiments, we measure the light transmitted through the tapered fiber, so that $T(t) = |(1 - \sqrt{\gamma_{ex}} a_{cw}(t))/S_{in}(t)|^2$, where $a_{cw} = 1/2(A_1(t) + A_2(t))$. $T_b(t)$ is a beat signal between the initial signals with frequencies, $\Delta\omega$ and $\Delta\omega \pm g$, and has the following form

$$\begin{aligned}T_b(t) &\simeq -\frac{4\gamma_{ex}|I|e^{-\gamma t/2}}{4\Delta\omega^2 + \gamma^2} \left[\left(1 + \frac{1}{2}\cos(2gt)\right) \{\gamma' \cos(\Delta\omega t) - 2\Delta\omega \sin(\Delta\omega t)\} \right. \\ &\quad \left. - \frac{1}{2}\sin(2gt) \{\gamma' \sin(\Delta\omega t) + 2\Delta\omega \cos(\Delta\omega t)\} \right].\end{aligned}\quad (4.32)$$

From the above equation, when there is mode splitting due to intrinsic scattering, the transient signal has a trigonometric form of frequency, $\Delta\omega$, and is modulated by a slowly oscillating envelope with a frequency of $2g$. This yields a similar waveform to that obtained in the uncoupled modes' case. Comparing Eq. 4.32 to Eq. 4.29, we see that there is a factor of 1/2 difference. When modal coupling is present, the two modes interfere with each other, whereas for the uncoupled case, the beating of the two modes has no coherent property.

4.3 Numerical Methods

For a more precise simulation of the transient system, we should solve the coupled-mode equations numerically. Equation 4.1 can be transformed into a rotating frame of reference, with an angular frequency, ω_L , such that

$$\frac{da(t)}{dt} = -i\Delta\omega a(t) - \frac{\gamma}{2} a(t) + \sqrt{\gamma_{ex}} s_{in}(t).\quad (4.33)$$

The input-output relationship for the rotating frame is $s_{out}(t) = -s_{in}(t) + \sqrt{\gamma_{ex}}a(t)$. For simplicity, we rescale the time by t_r in the following discussion and we assume that the WGR is critically coupled to the external coupler, unless we explicitly mention otherwise. All of the simulations are done in MATLAB using the Runge-Kutta methods. All analytical plots are based on Eq. 4.21 and Eq. 4.24 (see Appendix B for details). First, let us assume that the lifetime of a WGM is about 250 ns. Three different responses under various detunings are plotted in Fig. 4.3(a), ranging from $\Delta\omega = 3\gamma$ to $\Delta\omega = 9\gamma$. After the rising up, there is a sharp peak followed by a dip, and then a ringing peak that is less sharp. For the rest of the text in this chapter, we term the sharp peak as a "sharp peak", whereas we call the less-sharp peak, simply a "peak" (for example, "the peak height of the less-sharp peak" is just "the peak height"). The unique waveform is due to the negative sign of the sine function in Eq. 4.24. The oscillation period follows the detuning, so that a larger detuning yields a higher oscillation frequency, which represents the beating between the laser and WGM frequencies, as discussed in Section 4.2.

First, we evaluate the peak height (i.e., the height of the less-sharp peak; for example, when $\Delta\omega = 3\gamma$, the second peak it shown in Fig. 4.3(a))³. When Q is high, γ is small, and the detuning is sufficiently large (see Fig. 4.3(b)). This evaluation is possible and valid as the sine curve is dominant. The peak is always higher than the sharp peak in this regime. The height of the second peak reduces when the detuning increases. However, when the detuning is too small, the peak height decreases and the evaluation of the peak height for sensing purposes loses its validity. The analytical and numerical results match each other quite well when the detuning $\Delta\omega$ is smaller than $1/t_r$. When $\Delta\omega$ is large, the curves from the analytical and numerical plots start to diverge, as predicted by Eq. 4.21. If $\Delta\omega$ is fixed at $\Delta\omega \ll 1/t_r$ while the ratio γ_{ex}/γ is changed, the peak height is roughly linear to γ_{ex}/γ , as we can see in Fig. 4.3(c). A more comprehensive numerical simulation is shown in Fig. 4.3(e). This ensures that evaluating the peak height is always valid when the detuning is between 5 to 20 times γ in the high Q situation. The bandwidth of the transient broadening is determined by t_r ; therefore, it controls the peak height relationship to detuning, as illustrated in Fig. 4.3(d). Significant bandwidth shrinkage is visible only if the rise time increases by more than a factor of 10. This verifies the behavior we assumed in Section 4.2. In essence, it is the broadening from the rise time of a detuned pulse that allows light to couple into the WGM and leads to the subsequent beat signal.

Research projects within our group include nanoparticle sensing in a so-called quasi-droplet silica microbubble [24]. In a microbubble, a nanoparticle approaching the inner wall surface is expected to be detected through the intracavity evanescent field. The evanescent field can be extended and, thereby, sensitivity can be improved, by decreasing the wall thickness. However, when the wall thickness is decreased, the photon lifetime is also decreased. This can be partially compensated by filling the microbubble with water (quasi-droplet regime). With this compensation, the Q-factor of a silica microbubble can be maintained to more than 10^6 in the 780 nm waveband (i.e., $\tau > 2$ ns) near the lower limit of the wall thickness ($\sim 0.5 \mu\text{m}$). To evaluate the possibility of transient sensing in a quasi-droplet silica microbubble, CRUS signals in

³This differs from the original manuscript [77].

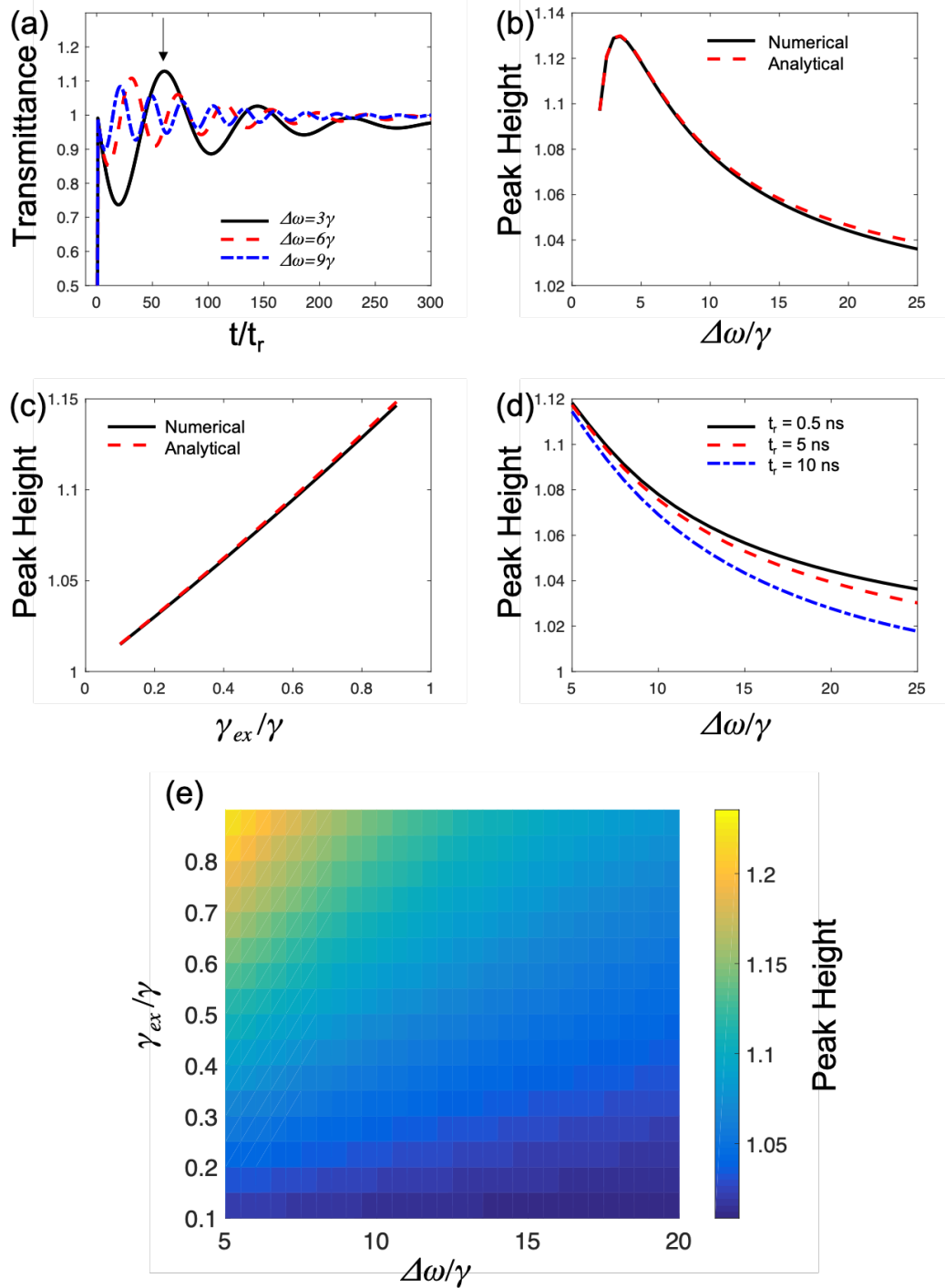


Figure 4.3: (a). The transient response of a pulse detuned to the high Q WGM. The legend shows the detuning (normalized to γ) for different curves. (b) The peak heights (less-sharp peak), for different detunings in (a). The peak height decreases when the detuning is smaller than 4γ . If this is the case, the evaluation of the peak height for sensing loses its validity. (c) The peak heights at different coupling conditions, γ_{ex}/γ . (d) Peak heights as a function of detuning for certain coupling conditions with different pulse rise-up times, t_r . (e) A comprehensive simulation of the peak height showing that evaluation of the peak height is valid when the detuning is between 5γ and 20γ in a high Q cavity.

a short photon lifetime regime (i.e., for $\tau \sim 2$ ns) are also numerically investigated.

We suppose the photon lifetime is 3 ns, or the Q-factor $\sim 1 \times 10^6$, with a pump laser at 780 nm wavelength. The numerical simulation results of the CRUS signal for different detunings, Fig. 4.4(a), and different external decays, Fig. 4.4(b), are plotted. In Fig. 4.4(a), γ_{ex} is fixed to 0.5γ , and in Fig. 4.4(b), $\Delta\omega$ is fixed to 0.5γ . In a low Q cavity, the transient signal decays quickly and reaches equilibrium level, as we can see in Fig. 4.4. The evaluation of the peak height⁴ is not valid for a low Q cavity. The static transmission level decreases as a function of decreased detuning.

Next, we evaluate the possibility of dissipative transient sensing. The equilibrium transmission level does not have a consistent signature of increase or decrease along with the increase of γ_{ex} . (Note this is described as the transmission spectrum in a different coupling regime, c.f. Section 2.4.1.) However, the sharp peak of the CRUS signal (shown by a black arrow in Fig. 4.4(b)) may be negatively related to the increase of the external decay. This needs further analysis and discussion because the sharp peak may not appear, as we see in Fig. 4.4(a), when $\Delta\omega = 2\gamma$, the blue double-dashed curve.

4.4 Experiment

To confirm the above theory, we performed an experiment using an ultrahigh Q silica microsphere. The experimental setup is depicted in Fig. 4.5. A 30 μ W, 1550 nm laser was initially modulated using an intensity modulator with an EOM (Thorlabs model LN63S-FC, with rise-up time 50 ps). For this purpose, a pulse generator providing a pulse with a rise time of 5 ns, a width of 500 ns, and a delay of ~ 100 ns was used. The modulated light was coupled to the microsphere's WGM using a fiber taper. The transmission through the fiber was detected with a fast photodetector (Newport model 818-BB-35F) with a typical rise time of 500 ps. The signal was retrieved on a digital storage oscilloscope (DSO) and recorded at a sampling rate of > 1 GS/s. The microsphere had a diameter of 80 μ m and the fiber waist was ~ 1.2 μ m. We chose a high Q silica microsphere with a lifetime of ~ 500 ns. To study the detuning effects on the CRUS, the microsphere and the fiber taper were aligned to be in contact coupling mode, therefore the coupling condition γ_{ex}/γ is fixed. The coupling regime is determined by the diameter of the tapered fiber. In our case, the diameter is ~ 1 μ m and the coupling regime is over-coupling. The detuning of the laser with respect to the whispering gallery mode was changed so that its frequency approaches that of the WGM in finite steps. The results were normalized to get the peak heights and are plotted in Fig. 4.6.

We made a separate measurement of the transmission spectrum of the WGM being probed, as illustrated in Fig. 4.6(a). From the transmission efficiency of the mode (80%), and assuming that the system is in the undercoupled regime, it can be deduced that $\gamma_{ex}/\gamma = 0.3$. The FWHM of the mode is 1.5 MHz using Lorentz fitting to the dip in Fig. 4.6(a). The peak height decreases when the pump laser is far detuned. This matches the theoretical prediction illustrated in Fig. 4.3(b).

⁴Shown in Fig. 4.4(a)

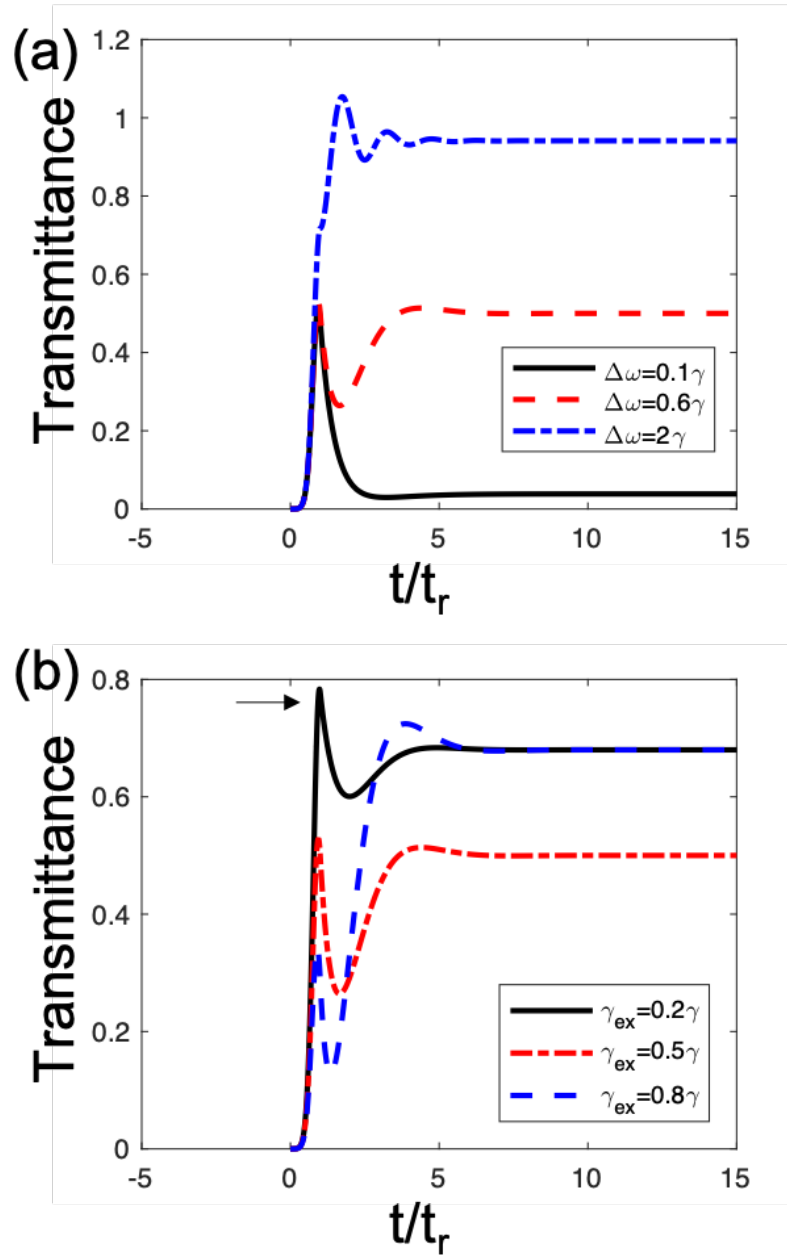


Figure 4.4: Numerical simulation results when the photon lifetime is 3 ns. (a) CRUS signal with different detunings. The external decay rate, γ_{ex} , is set to be 0.5γ . (b) CRUS signal with different external decays. The frequency detuning, $\Delta\omega$, is set to be 0.5γ .

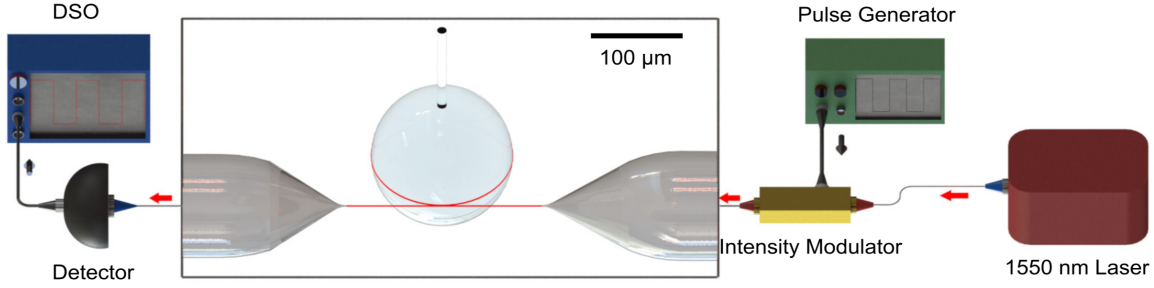


Figure 4.5: The experimental setup used for cavity ring-up spectroscopy. A 1550 nm laser is intensity modulated and coupled to the microsphere cavity and the transmitted light pulses are detected using a fast detector, with the signals recorded on a fast digital storage oscilloscope (DSO).

We also evaluated the peak height with different coupling gaps by varying the gap using a closed-loop, piezo nanopositioner (Smaract SLC1730s-416). The relative position of the taper from the microsphere was determined using a nanopositioner controller (Smaract MCS-3D). Here, γ_{in} is a constant, while γ_{ex} satisfies a near exponential curve to the coupling gap [166], as shown in the inset of Fig. 4.6(c). The corresponding peak heights for different coupling conditions plotted in Fig. 4.6(c) show a near-linear relationship.

From Fig. 4.6(c), we see that when the coupling gap is increased the period of the CRUS becomes larger. The taper introduces a dispersive red-shift to the microsphere's resonance [86]. In our experiments, the laser is blue-detuned relative to the resonance and fixed. The larger the distance between the WGR and the taper, the less the dispersion introduced; thus, the cavity mode shifts relative to the laser, thereby decreasing the beat frequency. In Eq. 4.24, the peak height should be related to both the coupling condition and the detuning. However, supposing the detuning is large, slightly changing its value will not influence the peak height significantly, see Fig. 4.3(b). In the experiment, we deliberately chose an initial large detuning; therefore, the peak height is still linear with γ_{ex}/γ despite the dispersive disturbances. When the system is strongly overcoupled, the results deviate from the linear relationship, as seen when $\gamma_{ex}/\gamma = 0.75$. In the supplementary material of Ref. [86], it was shown that the dispersive shift rate increases exponentially when moving to a strongly overcoupled regime. This means that the dispersive influence of the taper will induce a very large frequency shift for the cavity mode and cannot be neglected. As a consequence, the peak height does not vary linearly with γ_{ex}/γ .

Next we show several data that match the theoretical and numerical predictions in Sections 4.2.1 and 4.3. As mentioned in Section 4.3, to apply the transient sensing to the so-called quasi-droplet silica microbubble [24], we experimentally collected several sets of data using the same experimental setup as described in Fig. 4.5⁵. This time, the profile of the rectangular pulse is 1 ns of rise time, 120 ns of pulse width, and 500 μs of delay time.

⁵Only the sample is different; instead of a microsphere, a microbottle with a diameter of 57 μm was used.

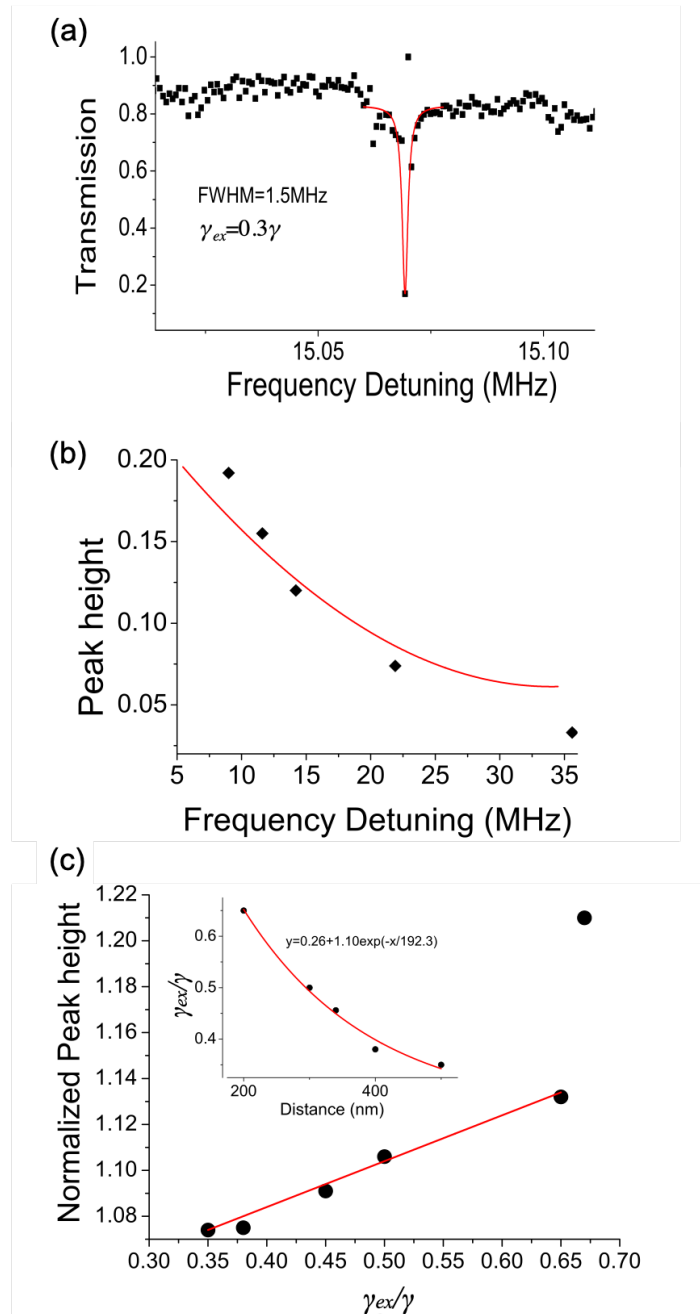


Figure 4.6: (a) The transmission spectrum of the microsphere which has an ultrahigh Q WGM. (b) The peak height measured at different laser detunings simulating a dispersive shift of the microsphere. The red curve is the theoretical fitting based on the published theory [77]. (c) The peak satisfies a linear relationship to γ_{ex}/γ . The inset shows the external coupling coefficient as an exponential function of the coupling gap.

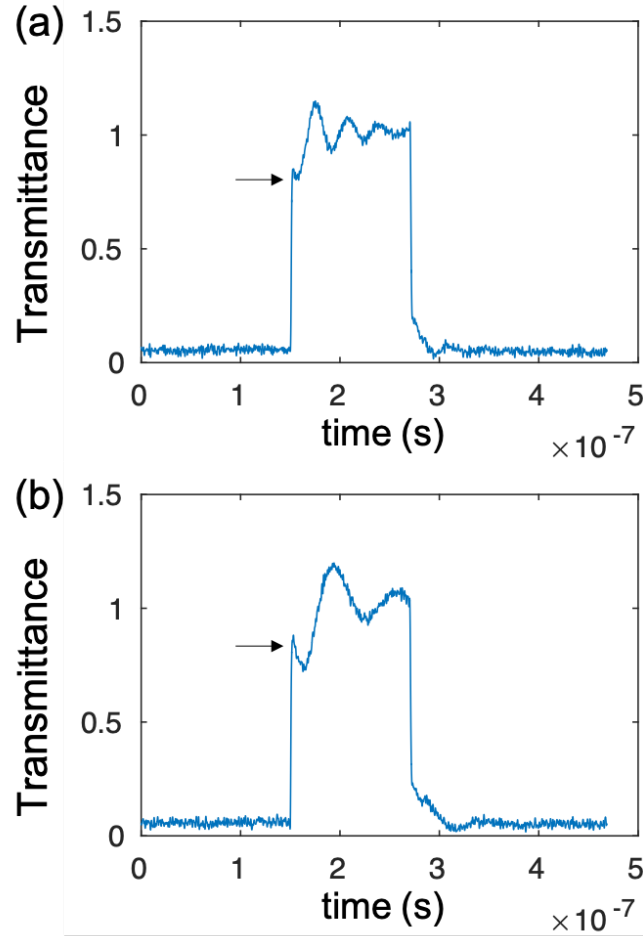


Figure 4.7: Normalized transmittance signal of CRUS. (a) When the detuning is relatively large, a small sharp peak can be seen following the rising up. (b) When the detuning is decreased, the ringing frequency decreases and the sharp peak become more pronounced.

First, we coupled light to a high Q mode, where its Q-factor is estimated to be $\sim 10^8$ (lifetime ~ 500 ns). We can see the sharp peak soon after the rising up in Fig. 4.7(a). This was not fully understood when the data was originally analyzed. Now we see the sharp peak corresponds to the simulation result in Fig. 4.3(a). Next, we decrease the detuning and the sharp peak becomes more pronounced as the dip become deeper, see 4.7(b). This tendency can also be seen in Fig. 4.3(a).

Finally, we show the results when we coupled light to a low Q mode, intended to push forward the plan of transient sensing in the quasi-droplet regime. The Q-factor of the optical mode is estimated to be $\sim 10^6$ (lifetime ~ 5 ns). From all of the plots in Fig. 4.8, we see that the ringing up signal decays quickly and reaches the equilibrium transmission level. Then, as the detuning is decreased, the equilibrium transmission level decreases, see Fig. 4.8(a)-(d). This corresponds to the simulation results plotted in Fig. 4.4(a). We also see the case where the sharp peak is almost hidden, in Fig. 4.8(a), by the black arrow, as predicted in Fig. 4.4(a) by the blue double-dashed line.

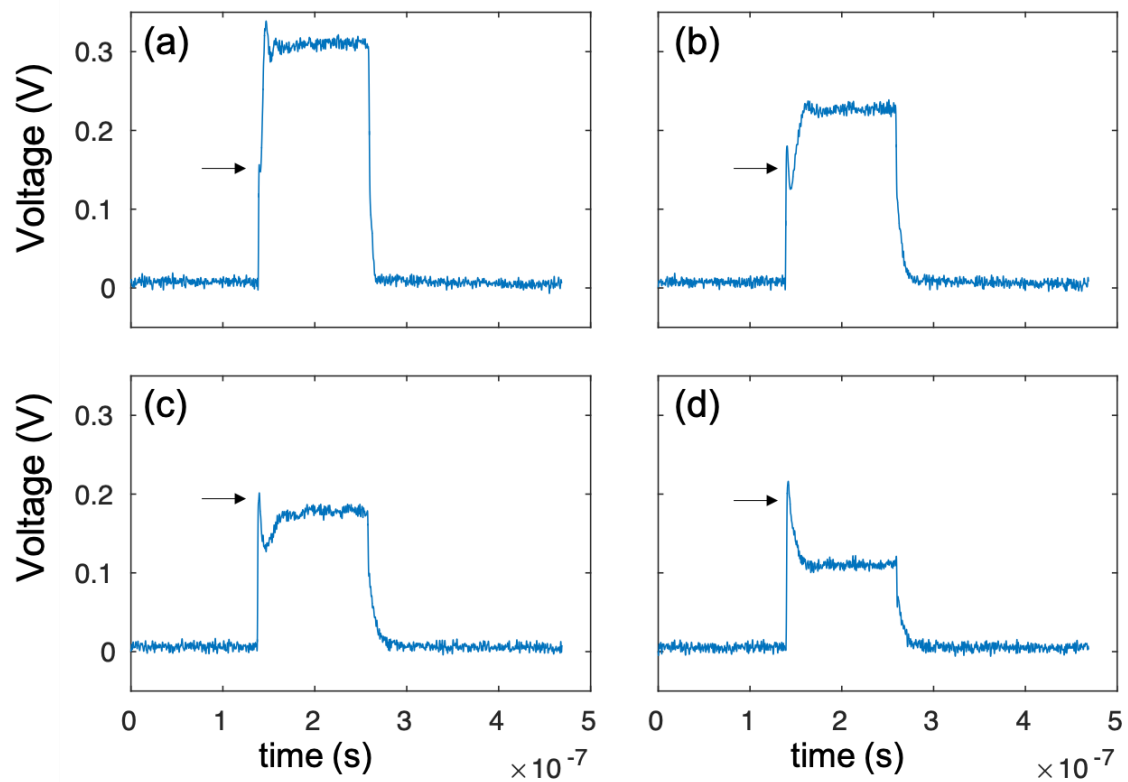


Figure 4.8: Transient signal of CRUS in a low Q ($\sim 10^6$) cavity with different detuning. (a) When the frequency is far detuned, the sharp peak cannot be seen clearly. (b)-(d) As the detuning become smaller, the equilibrium transmission level decreases, and the sharp peak become obvious.

4.5 Discussion

Similar to the work in [70], the deduced formula of CRUS here shows that it also provides redundant information if the cavity's intrinsic Q-factor is high and known. Instead of doing a time-consuming fast Fourier transform (FFT) of the transient response signal [69], one can record the maximum of the transient signal to retrieve the information for sensing, assuming that one can measure all the other parameters, such as γ_{ex} , γ_{in} , and t_r , from the steady-state transmission spectrum. This significantly reduces the complexity of the data processing and decreases the burden for data acquisition. In this sense, the acquisition speed can be further improved. For sensing based on reactive/dispersive interactions [39], the sensitivity can be optimized by choosing the correct laser detuning. In order to obtain valid sensing, while the sensitivity is maintained, the pump laser frequency should be chosen so that the detuning is near ten times the decay rate, γ . For example, in Fig. 4.3(b), when $\Delta\omega \sim 10\gamma$, the sensitivity is $dH/d\Delta\omega \sim 0.005/\gamma$ (where H is the peak height). Also, from Fig. 4.3(d), when t_r is longer, the curve is steeper; this also improves the sensitivity.

For dissipative sensing [53], measuring the peak height for a fixed detuning will also yield valid results. As numerically shown in Fig. 4.3(e), the peak height changes almost linearly with γ_{ex}/γ in a high Q cavity, with sufficiently large detuning. If the system experiences an intrinsic dissipation change due to environmental conditions, the peak height should maintain an inverse relationship to intrinsic dissipation under a certain coupling condition, i.e., the gap between the taper and the microsphere in our case. In a more complicated scenario, where both dispersion and dissipation exist, extracting dissipative (or dispersive) information from the mixed information may not be efficient only by measuring the peak height. One may suppress the dispersive change by increasing the detuning in order to purify the dissipative information. From Fig. 4.3(e), we are able to see this also suppresses the sensitivity to the dissipative information. Either dispersive or dissipative sensing has to be done by evaluating other parameters, for example the ringing frequency, or performed by other methods, in order to attain reliable sensing. Recently, we become aware that the peak actually decreases when the detuning is small, as illustrated in Fig. 4.3(b), while the equilibrium level should follow a Lorentzian profile, as mentioned in Eq. 4.25. Therefore, instead of viewing the evaluation of the peak height to be invalid, the decrease of the peak height may be directly used for sensing, and the sensitivity should be as high as that achievable for steady-state sensing. In this case, the highest sensitivity can be achieved when the detuning is small, and the mix between dispersive and dissipative information may be resolved. The temporal resolution needed is a few tens of ns to resolve the peak height.

On the other hand, in a low Q cavity (again, $Q \sim 10^6$; or $\tau \sim 3$ ns), dispersive sensing can be simply done by measuring the equilibrium level of the transmission, which is reached quickly due to a short photon lifetime. Dissipative sensing may also be possible by measuring the height of the sharp peak, following the rising up. This requires further comprehensive research about the height dependence of the sharp peak to the dissipative change in a low Q cavity. However, as we can see in Fig. 4.4(b), the

sharp peak dependence on γ_{ex} is certain⁶. The sharp peak may only be obscured when the detuning is large. This perspective is true from the current scope of analysis, as seen in Fig. 4.4(a) and Fig. 4.8(a).

Recently, we have also come to realize that the Kerr and thermal effects are, in fact, not negligible in Fig. 4.7 and Fig. 4.8 [69], in contrast to our earlier assumptions. Thence, the experimental data should be further analyzed. When the Q-factor is as low as 10^6 , based on simulation results, the sharp peak height change can be as sensitive as $(0.6 \text{ pulse height})/\gamma$ and the equilibrium level change is $(0.9 \text{ pulse height})/\gamma$, and $\gamma = 2 \times 10^9 \text{ s}^{-1}$. The temporal resolution is also from a few to tens of nanosecond for the pulse level to reach equilibrium.

The sensitivity follows the same trend as conventional steady-state sensing: scanning the laser frequency and monitoring the change of the absorption spectrum should be sufficient. Therefore, if Q drops the sensitivity will also drop. The sensitivity can be resolved by the pulse height and noise level, similar to the fixed frequency case in [70].

4.6 Conclusion

In summary, the dynamical mechanisms behind CRUS in a high Q optical resonator were investigated by solving the coupled-mode equations for a transient response to a Gaussian input pulse. The detailed relationship of CRUS to laser detuning, coupling coefficient, and rise time was determined using approximate analytical solutions. This was further verified by numerical simulations and experimental measurements.

We also investigated the case when the Q-factor is as low as 10^6 . A theoretical study shows the possibility of achieving transient sensing in the quasi-droplet regime with an MBR. Further experimental work needs to be done to verify the theory is correct and to demonstrate that the MBR can, indeed, be used as a transient sensing platform.

⁶This does not apply for a high Q cavity.

Chapter 5

Optical Force Between Coupled Whispering Gallery Mode Resonators

5.1 Introduction

While the previous chapter dealt with the feasibility of using a microbubble resonator for transient sensing, here we consider a completely different application by tuning the resonant frequency of an MBR using internal air pressure. This technique can be used to match the MBR resonance with that of another WGMR, thereby achieving co-resonance. In this chapter, we use an MBR to push forward the proposed plan from previous work of our research group [85]. In a coupled resonator configuration, symmetric and antisymmetric supermodes can be excited. The symmetric supermode yields an attractive force and can be excited when two cavities are distant from each other. The antisymmetric supermode can be excited when the two cavities are near each other and yields a repulsive force. When two pump lasers are configured so that their frequencies match those of the two supermodes, the system can provide a trapping force that keeps the two coupled resonators at a certain distance from each other. The work presented in this chapter is concerned with investigating the strength of this trapping force.

First, a brief introduction to the coupled resonators system is given. With the framework provided in [83], different regimes such as EIT-like, ATS-like, and an intermediate regime will be defined. Next, the analytical expressions for the optomechanical transduction spectrum of the micropendulum will be deduced for the intermediate regime. The experimental setup of the photonic molecule using a micropendulum and a pressure-tunable microbubble resonator (MBR) is described and a fit to the experimental results is also given. Note, in this work we used a microsphere instead of a micropendulum. Finally, the affect of the intermediate regime on the trapping potential in an ideal, coupled resonator system is examined.

5.2 Theory of Coupled Resonators

In our system, a microbubble resonator is coupled to a tapered fiber and a microsphere is positioned adjacent to the MBR, see Fig. 5.3. If we use the coupled-mode equation

for two cavities in a steady state, the intracavity field amplitudes, A_1 and A_2 , satisfy the equations:

$$(i\Delta\omega_1 - \frac{\gamma_1}{2})A_1 - i\kappa A_2 = \sqrt{\gamma_{ex}}A_0, \quad (5.1)$$

$$(i\Delta\omega_2 - \frac{\gamma_2}{2})A_2 - i\kappa A_1 = 0, \quad (5.2)$$

where γ_1 and γ_2 are the total cavity losses in the MBR and the microsphere, respectively, with $\gamma_1 > \gamma_2$ in our experiments and κ is the coupling coefficient between the two cavities. $\Delta\omega_{1,2}$ are the detunings between the pump laser and the resonant frequency of the MBR, ω_1 , and microsphere, ω_2 , respectively. In other words, $\Delta\omega_1 = |\omega_0 - \omega_1|$ and $\Delta\omega_2 = |\omega_0 - \omega_2|$, where ω_0 is the laser frequency. The normalized transmission is approximated to be

$$T \sim 1 - 2\gamma_{ex}Im(\chi), \quad (5.3)$$

with

$$\chi = \frac{\omega_0 + i\alpha_2}{\kappa^2 - (\omega_0 + i\alpha_1)(\omega_0 + i\alpha_2)}, \quad (5.4)$$

where $\alpha_1 = i\omega_1 + \gamma_1/2$ and $\alpha_2 = i\omega_2 + \gamma_2/2$. The intracavity field of the MBR is expressed as $A_1 = i\sqrt{\gamma_{ex}}A_0\chi$. The two coupled cavities have supermodes. The complex eigenfrequencies, ω_{\pm} , are defined when the amplitude of the intracavity field reaches infinity. In reality, the laser frequency has a real value, therefore infinity is never reached and

$$\omega_{\pm} = \frac{-i(\alpha_1 + \alpha_2) \pm \beta}{2}, \quad (5.5)$$

where $\beta = \sqrt{4\kappa^2 - (\alpha_1 - \alpha_2)^2}$. When $\beta = 0$, we define the threshold of the coupling strength, $\xi \equiv (\gamma_1 - \gamma_2)/4$.

5.2.1 Coupled-Mode Induced Transparency

For $\kappa < \xi$, β is imaginary. The real part of the eigenfrequency is $Re(\omega_{\pm}) = (\omega_1 + \omega_2)/2$ and the imaginary part is $Im(\omega_{\pm}) = -\zeta \pm |\beta|/2$ with $\zeta = (\gamma_1 + \gamma_2)/4$. This means that the supermodes are degenerate with the same frequency, $\Omega \equiv (\omega_1 + \omega_2)/2$, but the linewidths are different for each supermode. The imaginary part of χ is derived to yield the EIT-like transmission spectrum:

$$T_{EIT} = 1 - 2\gamma_{ex} \left[\frac{-(1/2 + \xi/|\beta|)Im(\omega_-)}{\Delta\omega^2 + Im(\omega_-)^2} - \frac{(1/2 - \xi/|\beta|)Im(\omega_+)}{\Delta\omega^2 + Im(\omega_+)^2} \right], \quad (5.6)$$

with detuning $\Delta\omega = |\omega_0 - \Omega|$. We see that two Lorentzians with different signs and linewidths appear in $Im(\chi)$. Note $Im(\omega_{\pm})$ and $(1/2 - \xi/|\beta|)$ are negative here, therefore both fraction terms in the square bracket are positive. The Lorentzian with positive sign has a larger linewidth, $2|\omega_-|$, is the transmission dip. The other term, with negative sign, has a narrower linewidth, $2|\omega_+|$, and represents a transparency window, similar to EIT. As the coupling strength, κ , increases, $|\beta|$ decreases and the linewidth of the transparency window increases.

5.2.2 Autler-Townes Splitting

When the coupling strength is much larger than the transition threshold (i.e., $\kappa \gg \xi$), β is real. Neglecting $(\alpha_1 - \alpha_2)^2/\beta^2$, the complex eigenfrequencies become $\omega_{\pm} \sim \Omega - i\zeta \pm \kappa$. The transmission spectrum is given by

$$T_{ATS} = 1 - \gamma_{ex} \left[\frac{\zeta}{(\Delta\omega - \kappa)^2 + \zeta^2} + \frac{\zeta}{(\Delta\omega + \kappa)^2 + \zeta^2} \right]. \quad (5.7)$$

We see the two Lorentzian dips are located at detunings of $\pm\kappa$ from the center Ω . The linewidth of the dips are equal to each other. An increase of coupling strength leads to larger separation of the dips, while the linewidth 2ζ stays the same.

5.2.3 Intermediate Regime

When $\kappa > \xi$, we call it the intermediate regime. β is real and the eigenfrequencies are $\omega_{\pm} = \Omega - i\zeta \pm \beta$. The transmission spectrum is

$$T_{int} = 1 - 2\gamma_{ex} \left[\frac{(\Delta\omega/\beta - 1/2)\xi}{(\Delta\omega - \beta/2)^2 + \zeta^2} - \frac{(\Delta\omega/\beta + 1/2)\xi}{(\Delta\omega + \beta/2)^2 + \zeta^2} \right] - \gamma_{ex} \left[\frac{\zeta}{(\Delta\omega - \beta/2)^2 + \zeta^2} + \frac{\zeta}{(\Delta\omega + \beta/2)^2 + \zeta^2} \right]. \quad (5.8)$$

Both square bracket terms are composed of two Lorentzians located at detunings of $\pm\beta/2$. The first square bracket term has Lorentzians with different linewidths and the second square bracket term shows the contribution from the ATS-like regime. Examples for each regime are shown in Fig. 5.1. As the coupling strength κ increases, the EIT regime (a), the intermediate regime (b), and the ATS regime (c) appear.

5.3 Optomechanical Spectrum in the Coupled Resonators Structure ¹

We characterize the swinging motion of a micropendulum in the coupled system using two terms. Supposing the swinging amplitude is small, we can describe the change of the coupling strength, $\kappa(x)$, and the shift of the resonant frequency of the supermode, Ω , according to the pendulum's displacement, x . Note, we use the detuning, $\Delta\omega(x)$, instead of Ω , as we can always get Ω by adding the laser frequency, ω_0 , to $\Delta\omega(x)$:

$$\kappa(x) = \kappa(1 + g_{\kappa}x), \quad (5.9)$$

$$\Delta\omega(x) = \Delta\omega + g_{\omega}x. \quad (5.10)$$

According to earlier research [86], the oscillation period of the micropendulum is on the order of ms. We can assume the resonant light is always in the steady state while the

¹The theory was developed by Dr. Y. Yang, a former postdoctoral researcher in the LMI-QT Unit. The theory was also used for the thesis work of Dr. R. Madugani, a former PhD candidate in the LMI-QT Unit [170].

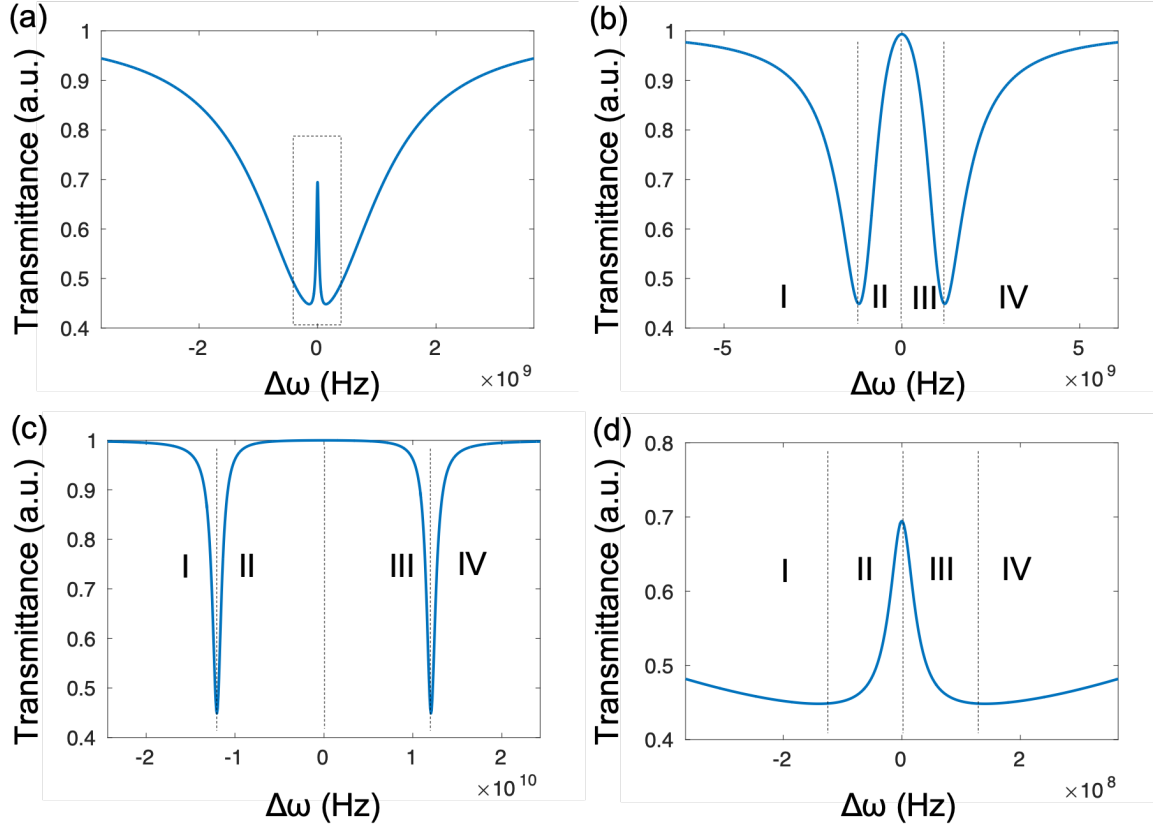


Figure 5.1: (a) The transmission spectrum in the EIT regime; the dashed window is shown in (d). (b) The transmission spectrum in the intermediate regime. (c) The transmission spectrum in the ATS regime. Parameters used are $\gamma_2 = 1.2 \times 10^7$, $\gamma_1 = 100\gamma_2$ and $\gamma_{ex} = \gamma_1/3$; $\kappa = 10\gamma_2$ for the EIT regime, $\kappa = \gamma_1 - \gamma_2$ for the intermediate regime, and $\kappa = 10(\gamma_1 - \gamma_2)$ for the ATS regime.

pendulum motion is introduced to the coupled system, as the lifetime of light in this system is on the μs scale. We can start from Eqs. 5.2 and 5.2 and include mechanical oscillation in each regime.

In the EIT regime, letting $\kappa \ll \xi$ as a relatively simple case, $|\beta|$ is approximated to become $|\beta| = \xi[2 - (\kappa/\xi)^2]$. $(\frac{\kappa(x)}{\xi})^2 \approx (\frac{\kappa}{\xi})^2(1 + 2g_\kappa x)$ and $\Delta\omega(x)^2 \approx \Delta\omega^2 + 2g_\omega \Delta\omega x$ also follow. Substituting these transformations into Eq. 5.6 and taking the first order Taylor expansion of x , the optomechanical transduction spectrum is approximated and takes the form:

$$\mathcal{T}_{EIT} \approx \left| \frac{\{\gamma_2'^2 \gamma_2 (\kappa/\xi)^2 - 2\gamma_2' \gamma_2 (\kappa/\xi)^4 + 4\gamma_2 (\kappa/\xi)^2 \Delta\omega^2\} g_\kappa - 4\gamma_2 (\kappa/\xi)^2 \Delta\omega g_\omega}{(4\Delta\omega^2 + \gamma_2'^2)^2} - \frac{(4\Delta\omega^2 + \gamma_1'^2) \gamma_1 (\kappa/\xi)^2 g_\kappa - 4[2\gamma_1 + \gamma_1 (\kappa/\xi)^2] \Delta\omega g_\omega}{(4\Delta\omega^2 + \gamma_1'^2)^2} \right|, \quad (5.11)$$

where $\gamma_2' = \gamma_2 + \kappa^2/\xi$. A numerical plot is shown in Figs. 5.2(a) and (b).

The optomechanical transduction spectrum when $\kappa \ll \xi$ is composed of four peaks. Starting from the red-detuned side, the first peak appears when the optical coupling

starts to enter the large transmission dip, i.e., region I in Fig. 5.1(d). Then, the second peak appears when the detuning reaches the red side of the transparency window, i.e., region II in Fig. 5.1(d). Next, another peak at the blue side of the transparency window appears, i.e., region III in Fig. 5.1(d) and, finally, the last peak appears when the coupling is leaving the large dip, i.e., region IV in Fig. 5.1(d).

For the ATS-like regime, the same optomechanics is used as for Eq. 5.7 and the optomechanical spectrum is obtained from the first order term of the Taylor expansion:

$$\mathcal{T}_{ATS} \approx \frac{2(\Delta\omega - \kappa)(g_\omega - g_\kappa\kappa)}{[(\Delta\omega - \kappa)^2 + \zeta^2]^2} + \frac{2(\Delta\omega + \kappa)(g_\omega + g_\kappa\kappa)}{[(\Delta\omega + \kappa)^2 + \zeta^2]^2}. \quad (5.12)$$

A numerical plot of this regime is shown in Figs. 5.2(c) and (d).

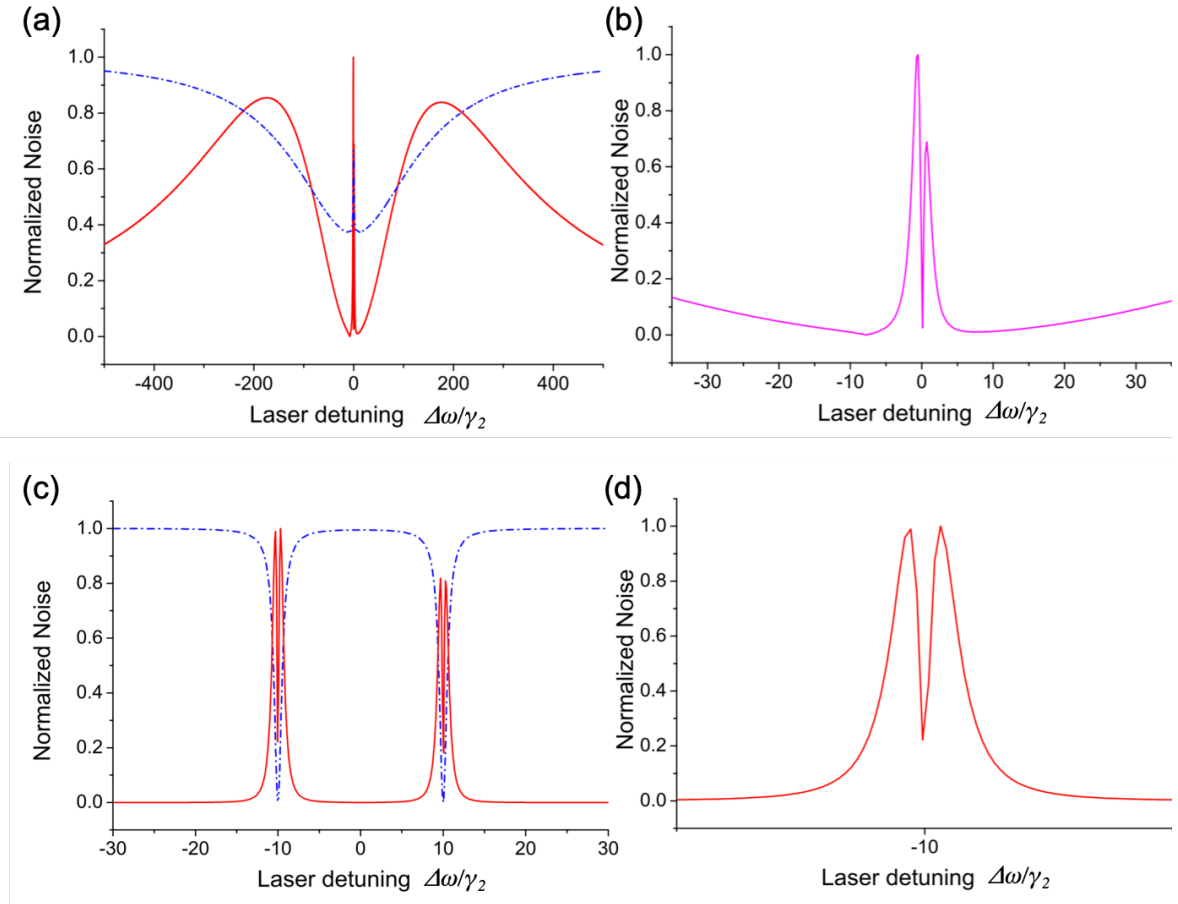


Figure 5.2: (a) Transduction noise spectrum (red solid line) and the corresponding transmission spectrum (blue dashed line) when the system is in the EIT regime. (b) A zoom-in window of (a) when the detuning is small. (c) Transduction noise spectrum (red solid line) and the corresponding transmission spectrum (blue dashed line) when the system is in the ATS regime. (d) A zoom-in window of (c) when the detuning is around one of the Lorentzian dips. The theoretical plot was generated by Dr. R. Madugani [170].

For the purpose of trapping, strong coupling, such as in ATS-like regime, is preferred. But, at room temperature, this regime may not be possible. Static charge is

estimated to be small [84]; however, thermal vibration can still affect the resonators and the two cavities will likely come into contact. Obviously, the intermediate regime can still be studied.

Recall the imaginary part of χ is:

$$\begin{aligned} \text{Im}(\chi) = & \frac{(\Delta\omega/\beta - 1/2)\xi}{(\Delta\omega - \beta/2)^2 + \zeta^2} - \frac{(\Delta\omega/\beta + 1/2)\xi}{(\Delta\omega + \beta/2)^2 + \zeta^2} \\ & + \frac{1}{2} \left[\frac{\zeta}{(\Delta\omega - \beta/2)^2 + \zeta^2} + \frac{\zeta}{(\Delta\omega + \beta/2)^2 + \zeta^2} \right]. \end{aligned} \quad (5.13)$$

The optomechanical transduction spectrum of the first term is:

$$\begin{aligned} \mathcal{T}_{int}\left(\frac{(\Delta\omega/\beta - 1/2)\xi}{(\Delta\omega - \beta/2)^2 + \zeta^2}\right) = \\ \left(\frac{\xi}{\beta}\right) \left[\frac{-(g_\omega + G_\kappa/\beta)(\Delta\omega - \beta)^2 + (g_\omega - G_\kappa/\beta)\zeta^2}{[(\Delta\omega - \beta)^2 + \zeta^2]^2} \right]. \end{aligned} \quad (5.14)$$

Here, $G_\kappa = g_\kappa\kappa^2/\beta$ is the effective coupling rate. In the condition that mechanical oscillation exists, β becomes $\beta + G_\kappa x$ when the displacement is x and assuming x is small. Similarly, the transduction spectrum of the second term is obtained as:

$$\begin{aligned} \mathcal{T}_{int}\left(\frac{(\Delta\omega/\beta + 1/2)\xi}{(\Delta\omega + \beta/2)^2 + \zeta^2}\right) = \\ \left(\frac{\xi}{\beta}\right) \left[\frac{-(g_\omega - G_\kappa/\beta)(\Delta\omega + \beta)^2 + (g_\omega + G_\kappa/\beta)\zeta^2}{[(\Delta\omega + \beta)^2 + \zeta^2]^2} \right]. \end{aligned} \quad (5.15)$$

The last term of Eq. 5.8, as we mentioned before, is a contribution from the ATS-like regime. Therefore, the transduction is also similar and is given by

$$\mathcal{T}_{int}(ATS - like) = \zeta \left[\frac{(\Delta\omega - \beta)(g_\omega - G_\kappa)}{[(\Delta\omega - \beta)^2 + \zeta^2]^2} + \frac{(\Delta\omega + \beta)(g_\omega + G_\kappa)}{[(\Delta\omega + \beta)^2 + \zeta^2]^2} \right]. \quad (5.16)$$

By adding Eqs. 5.14, 5.15 and 5.16 together, we obtain the optomechanical transduction spectrum. There are four peaks in the spectrum that appear according to the frequency detuning. We can see that the peaks appear when the laser frequency is on the slopes of the red- and blue-detuned sides of the two dips, i.e., in regions I to IV in Fig. 5.1(b). Depending on the system parameters, the four peaks have different heights. In order to confirm the theory, experimental work was done and is discussed in the next section.

5.4 Experimental Implementation with an MBR

To experimentally implement a coupled resonator system, the cavity modes of each resonator need to be in resonance. This can be done either by careful design and nanofabrication or by *in-situ* tuning. In our experiment, an MBR is chosen for *in-situ* tuning. By applying internal pressure into the MBR, the cavity is expands, thus shifting the optical modes [64]. Compared to other tuning mechanisms, pressure tuning

provides a linear response and long term stability [171]. A wide range of tuning is achieved in our laboratory in ultrathin walled MBRs with a Q-factor of nearly 10^7 [13]. Pressure tuning is spatially localized, making it a perfect candidate for realizing coupled resonators.

The coupled resonator system was achieved by placing a tapered fiber, MBR, and microsphere together as shown in Fig. 5.3(a). A scanning, narrow linewidth laser, at 1550 nm, was used to excite WGMs in the MBR and the transmitted optical power at the output of the tapered fiber was detected by a photodiode and monitored on a digital oscilloscope (DSO). Initially, only the MBR was coupled to the tapered fiber and only its WGM spectrum was shown on the DSO. When the microsphere was moved close enough to the MBR, the sphere's optical modes also appeared in the spectrum. Then, pressure of the gas inside the MBR was adjusted, see Fig. 5.4, to shift an MBR mode into resonance with a sphere mode. Mode splitting was observed by moving the sphere even closer to the MBR. A typical transmission spectrum when the two resonators

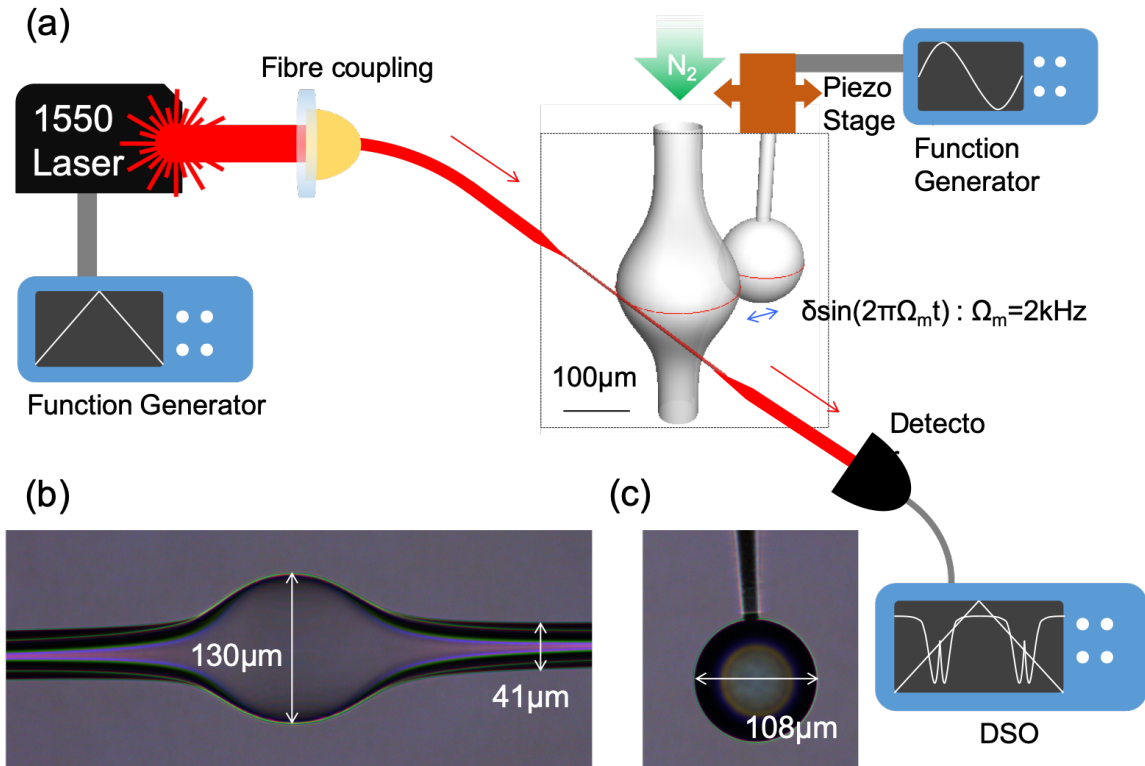


Figure 5.3: (a) Experimental setup for transduction measurement. (b) Fabricated microbubble and (c) microsphere.

from the photonic molecule are co-resonant is illustrated at the bottom of Fig. 5.4. When the two resonators have a large coupling gap, the coupling strength is weak, and an EIT-like spectrum can be found with a transparency window occurring at the center of the resonance. With stronger coupling, and a smaller gap, the system is driven into the ATS-like regime. The original transmission dip is split into two with nearly identical linewidths and depths, shown as the upper curves in Fig. 5.4. The frequency splitting of the modes increases when the gap between the two resonators is decreased.

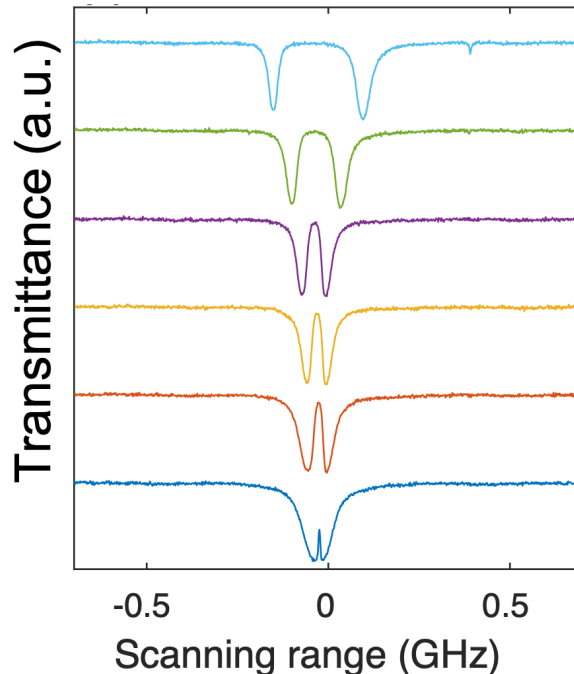


Figure 5.4: The normalized transmission spectrum of the coupled resonators when the two cavities are tuned into resonance. The spectrum shows the transition from the EIT-like to the ATS-like state.

The linewidth of the MBR and the microsphere were estimated to be $\gamma_1 = 2\pi \times 230$ MHz and $2\pi \times 58$ MHz, respectively, from transmission spectra obtained when the two modes are far detuned. Numerical fitting with Eq. 5.8 and Eq. 5.13 shows the coupling strength between the two cavities to be $\kappa = 2\pi \times 530$ MHz. To experimentally simulate the motion of a micropendulum, a sinusoidal driving voltage was applied to a custom-built piezo-actuated stage holding the sphere. This driving voltage moved the sphere in and out from the MBR with a frequency of 2 kHz. While the laser frequency was slowly scanned over the resonances of the supermodes, the transduced mechanical motion was recorded by taking an FFT of the transmitted optical power. The result shown, with error bars, in Fig. 5.5(b) is the average of 6 measurements. The fitting parameter shows that the system is in the intermediate regime rather than the ATS-like regime. The optomechanical transduction noise spectrum in the intermediate regime is also calculated for a theoretical fit (c.f. the red line in Fig. 5.5(b)). Fitting parameters is $G_\kappa/g_\omega = 30$.

5.5 Conclusion

In summary, we investigated the evanescent coupling of two resonators in order to estimate the possibility of trapping according to the proposal [85]. An MBR and a

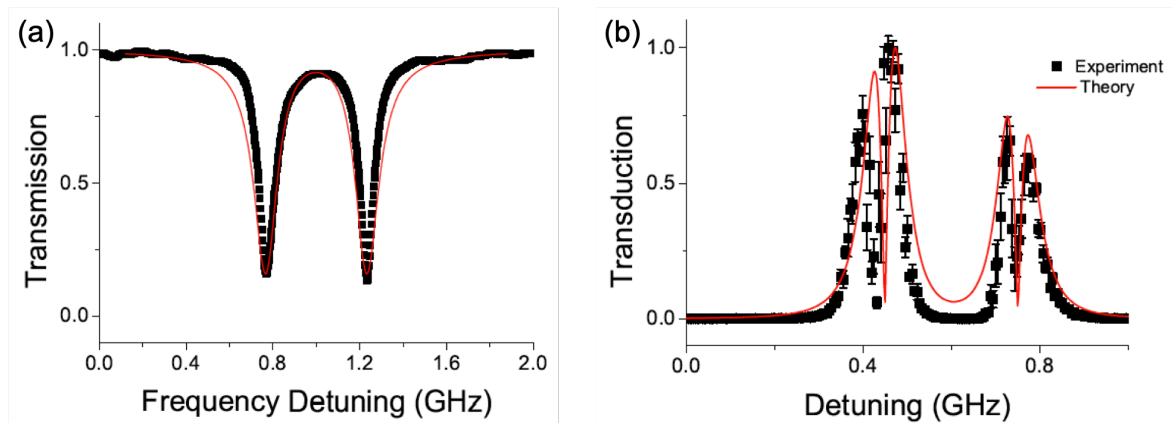


Figure 5.5: (a) The normalized optical transmission spectrum of the coupled cavities in the intermediate regime. (b) The normalized optomechanical transduction spectrum in the optical frequency domain in the coupled system in the intermediate regime. The theoretical fitting was done by Dr. Y. Yang.

microsphere were fabricated and coupled to each other for the demonstration. The MBR played a central role to excite supermodes as the resonance frequency can be tuned by air pressure. The system can be in the EIT-like regime, the intermediate regime, or the ATS-like regime depending on the coupling strength. The intermediate regime was experimentally achieved and the transduction spectrum was obtained. The shape of the transduction spectrum is asymmetric and shows good agreement with the theoretical prediction. A significant optical force has not been demonstrated and further investigation is needed. For example, light confinement could be improved by using smaller cavities and stronger pump power. This work further widens the scope of [85] and will guide a future experimental implementation of center-of-mass control.

Chapter 6

Microbubble Lasers for Pressure Sensing¹

6.1 Introduction

While in an earlier chapter we considered using an MBR as a sensing platform, it turns out that the air pressure tunability of an MBR itself can be viewed as a sensor. Here, we explore how a microlaser made from an MBR is not only a tunable laser, but also acts as a high sensitivity pressure sensor. Instead of measuring the transmission spectrum from a WGM cavity mode, sensing can also be done with the WGM microlaser. As lasing modes have narrower linewidths than expected resonance transmission dip in a WGM fiber-coupled cavity, a higher sensitivity can be achieved [54, 92, 103]. In this chapter, we report on an observed frequency shift of microbubble-based microlaser emissions due to air pressure tuning. The laser tuning is achievable due to the subwavelength wall thickness of an Er^{3+} -doped microbubble resonator, the fabrication of which is described in the following.

6.2 Fabrication

Having a high Q cavity mode is a necessary precondition for achieving low threshold lasing. For a passive MBR, we have previously demonstrated that the Q-factor can reach 10^7 , close to the theoretical limit [65]. To maintain the high Q after introducing a gain medium, we dissolved erbium ions into a sol-gel precursor solution and used this as the gain material, ensuring that the erbium ions are distributed uniformly in the silica matrix of the MBR after fabrication. The sol-gel precursor solution was made by mixing erbium(III) nitrate hydrate (i.e. $\text{Er}(\text{NO}_3)_3 \cdot 5\text{H}_2\text{O}$), tetraethoxysilane (i.e. TEOS), isopropyl alcohol (i.e. IPA), water (H_2O), and hydrochloric acid (37% HCl)

¹This work is published in Y. Yang, F. Lei, S. Kasumie, L. Xu, J. M. Ward, L. Yang and S. Nic Chormaic "Tunable erbium-doped microbubble laser fabricated by sol-gel coating", *Opt. Express* **25**, 1308-1313 (2017) [14]. S. Kasumie contributed to develop the fabrication of the erbium-doped MBR using sol-gel coating and writing of the manuscript. The sol-gel coating is done in the Micro/Nano Photonics Laboratory, Department of Electrical and Systems Engineering, Washington University in St. Louis, USA during a 3-month research visit.

with a weight ratio of 0.03:6.5:6.1:0.7:0.6 for 2 hours at 70°C [93]. After 24 hours, the sol-gel precursor was ready to use.

The fabrication steps for the erbium-doped MBR is presented in Fig. 6.1. First, two counter-propagating CO₂ laser beams were focused onto a silica capillary (outer diameter 350 μm, inner diameter 250 μm) to heat it, thereby allowing us to pull the capillary into a uniform taper with a waist diameter of around 30 μm. Afterwards, a droplet of the sol-gel precursor was transferred to the tapered capillary. Finally, the capillary was filled with compressed air and the CO₂ laser was reapplied to reheat it. With the correct choice of laser power, the section of capillary in the focus of the laser beams expands to form an MBR. Due to the high temperature, the residual sol-gel solvent was removed and only silica doped with erbium ions remained; this material formed the wall of the MBR during the expansion process. The maximum erbium concentration was $5 \times 10^{19}/\text{cm}^3$ according to the concentration in the sol-gel precursor.

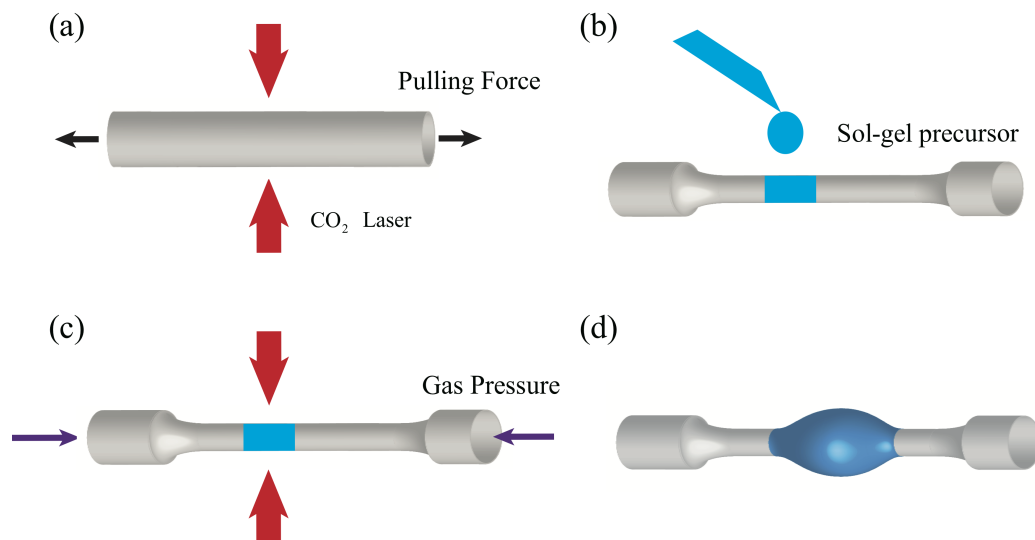


Figure 6.1: Schematic of the fabrication process for a sol-gel coated MBR using CO₂ laser heating. (a) A capillary is tapered using a CO₂ laser heat source. (b) Erbium ions are dissolved into a sol-gel precursor, which is drop-coated onto the tapered capillary. (c-d) The CO₂ laser heats the sol-gel and internal air pressure is applied until an MBR is formed.

6.3 Aero-pressure tuning of the MBR laser

6.3.1 Experimental Setup

The MBR was coupled to a tapered optical fiber that was placed in contact. The laser source was a broadband, 980 nm laser with a maximum power of 200 mW. The tapered fiber waist was about 1.1 μm. Since the 980 pump has a linewidth of about 2 nm, even without fine tuning of the pump laser frequency, some coupling into the MBR modes can occur. About 10% of the pump power was absorbed after passing the MBR. The coupled laser light excited 1535 nm lasing in the Er ions. The experimental setup is

illustrated in Fig. 6.2. The MBR was placed in a dry nitrogen gas environment to maintain the optical quality. In order to tune the frequency of the MBR, one of its outputs was sealed with epoxy, while the other end was connected to a compressed air cylinder. The internal pressure of the MBR was adjustable via a valve and the pressure reading was recorded on a pressure gauge. During the experiment, the pressure was changed from 0 bar to 2.5 bar. The lasing spectrum was measured on an optical spectrum analyzer (OSA), which had a minimum resolution of 0.07 nm.

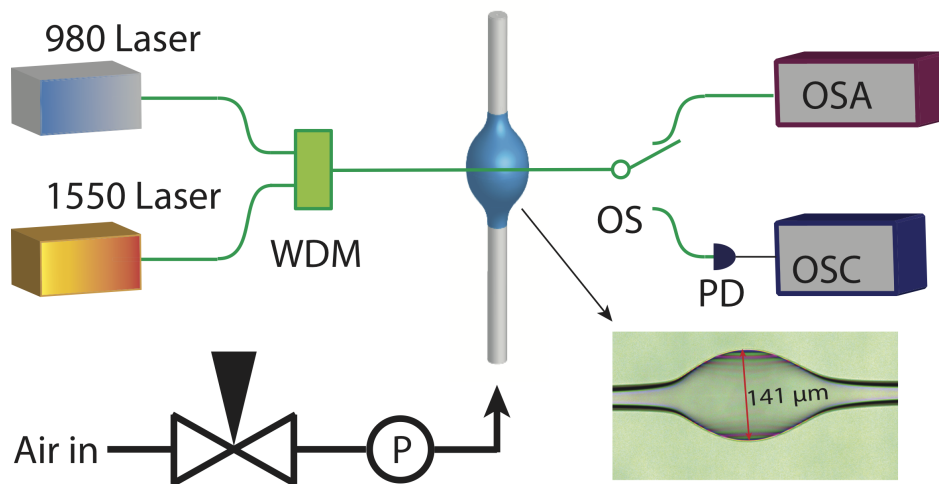


Figure 6.2: Schematic of the setup for pressure tunable lasing in an MBR. P: pressure gauge; OS: optical switch; PD: photodetector; OSC: oscilloscope; OSA: optical spectrum analyzer. The inset shows a microscopic image of the sol-gel coated MBR. The diameter of the MBR is 141 μm .

6.3.2 Experimental Results

First, the lasing threshold for the coated MBR was measured. The pump power was adjusted from 17.9 mW to 94.7 mW. Because the pump is broadband, it is difficult to know exactly how much power couples into the modes; therefore, we used the total pump power to evaluate the threshold. The laser output power at 1535.66 nm was recorded against the pump power and is plotted in Fig. 6.3(a) - the threshold is estimated to be about 27 mW. From the fluorescence background (see Fig. 6.3(b)) single mode lasing occurs (see Fig. 6.3(c)) when the pump power is beyond the threshold. In reality, the actual threshold must be significantly lower than this stated upper limit as there are certainly some coupling losses in the system.

By applying aerostatic pressure inside the bubble, the MBR expands so that all modes are red-shifted [64]. With a maximum applied pressure of 2.5 bar, the laser emission at 1535 nm was shifted by about 240 pm, as shown in Fig. 6.4(a). The shift of the modes is much smaller than the bandwidth of the pump. Therefore, even without tuning the wavelength of the pump, modes can still be excited via the 980 nm source. In the case here, single-mode lasing was achieved within the pressure tuning range. The wavelength shift as a function of the applied pressure is plotted in Fig. 6.4(b).

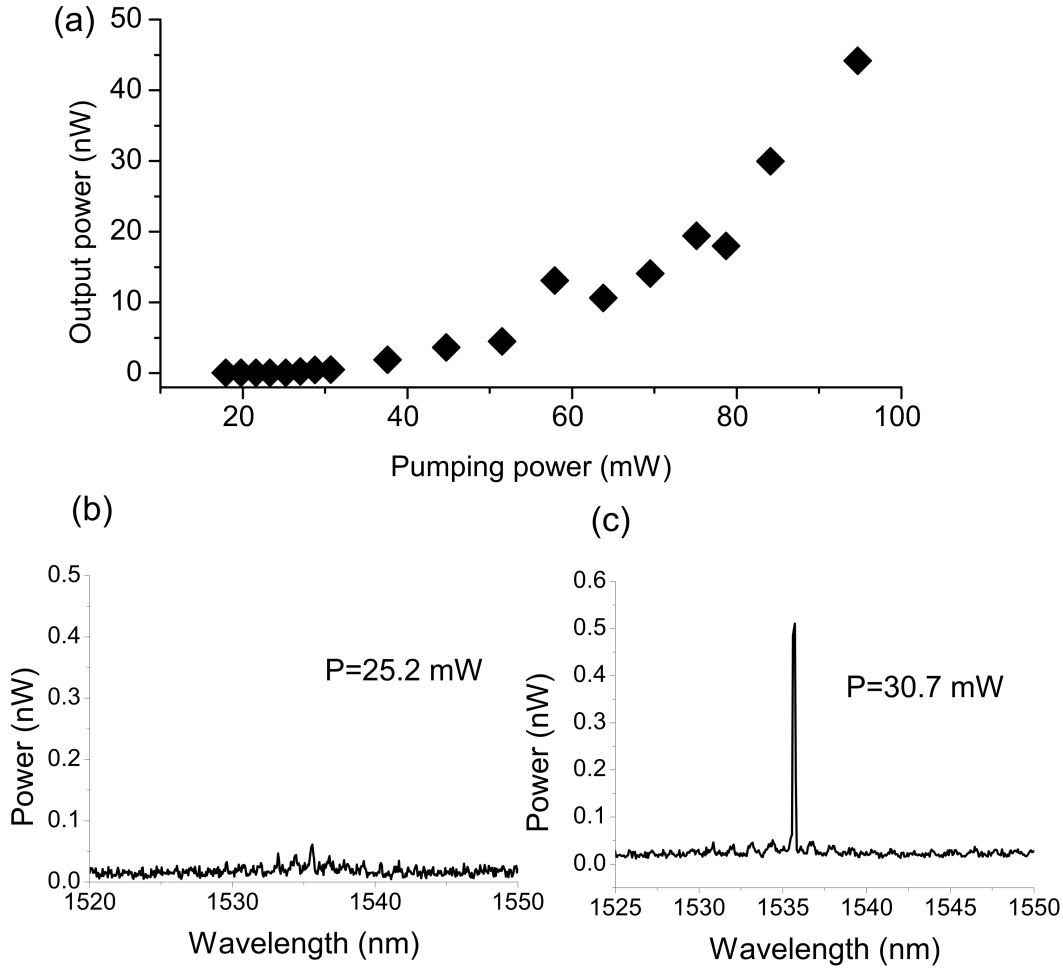


Figure 6.3: (a) Lasing threshold measurement of a sol-gel coated MBR. The total power of the pump laser is used for estimation. The threshold is about 27 mW for the pump laser. (b) The spectrum with the pump power below threshold. (c) The single-mode lasing spectrum near the threshold.

Note that this measurement is not so accurate since the laser linewidth and the mode shifts are smaller than the resolution of the OSA. However, a linear relationship is still obvious, similar to the linear tuning property of the modes of a passive MBR [64]. The sensitivity is the slope of the pressure tuning curve, which ranges from approximately 6 GHz/bar to 14 GHz/bar, as determined by the error bars in Fig. 6.4(b). For a subtle change of pressure, so that the OSA cannot resolve the change even if the sensitivity is increased, a beating effect can be used to measure the frequency shift instead. Active sensing in WGMs has already been developed by measuring the beat signal of a split lasing mode [54]. Here, the mode splitting effect is not caused by pressure. However, we can input a near-detuned laser so that the beat frequency can be measured, and thus, a small frequency shift can be determined.

In order to obtain a more accurate pressure tuning slope, we measured the transmission spectrum by switching to a finely tunable laser, around 1535 nm (New Focus

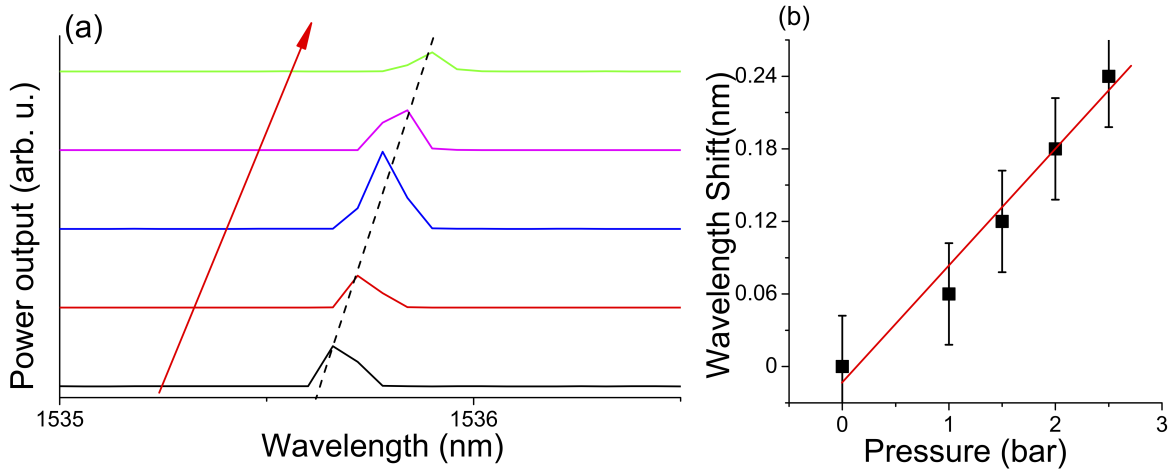


Figure 6.4: (a) The laser spectrum of the sol-gel coated MBR at different pressures. The arrow shows the direction of the pressure increase. From the bottom to the top are the laser emission lines from 0 bar to 2.5 bar applied pressure. The resolution of the spectrum is limited by the OSA. (b) The wavelength shift of the lasing mode as a function of the applied pressure. The red line is a linear fit and the error bar is set by the resolution of the OSA.

Velocity 6728), and a photodetector connected to an oscilloscope, as shown in Fig. 6.2. The transmission spectra of this MBR laser, for different applied pressures, are given in Fig. 6.5(a), where the mode is indicated by an arrow and the measured Q-factor is about 10^6 . The resolution of the pressure tuning, measured by monitoring the pump transmission through the fiber coupler, was limited only by the Q-factor [65] and is more accurate than measurements made using the spectrum analyzer. By tracking the resonance positions, shown in Fig. 6.5(b), a tuning sensitivity of 8.2 GHz/bar was measured. From the microscope image of the MBR, the wall thickness of the MBR was estimated to be about $1.3 \mu\text{m}$. For an MBR with a diameter of $141 \mu\text{m}$, the obtainable sensitivity is calculated to be 8.5 GHz/bar [64], which is in accordance with the measured results.

6.4 Conclusion

By using a sol-gel technique, a layer of Er^{3+} ions was coated onto the outer surface of an MBR. We achieved lasing emission at 1535.66 nm when pumped at 980 nm. We also observed a laser frequency shift when internal air pressure was applied. The lasing threshold could be further optimized if a narrow linewidth tunable pump laser were used. When the frequency is shifted by a target to be detected, all modes, including those modes at the pump wavelength, will shift. Therefore, a narrow band pump is not so practical for implementing such a sensing application as the pump itself needs to be locked to the MBR mode. With broad band pumping, the laser remains coupled to the MBR mode, making the setup simple. Other rare earth ions could be diffused into the wall of the MBR, thereby expanding the wavelength of the MBR laser to

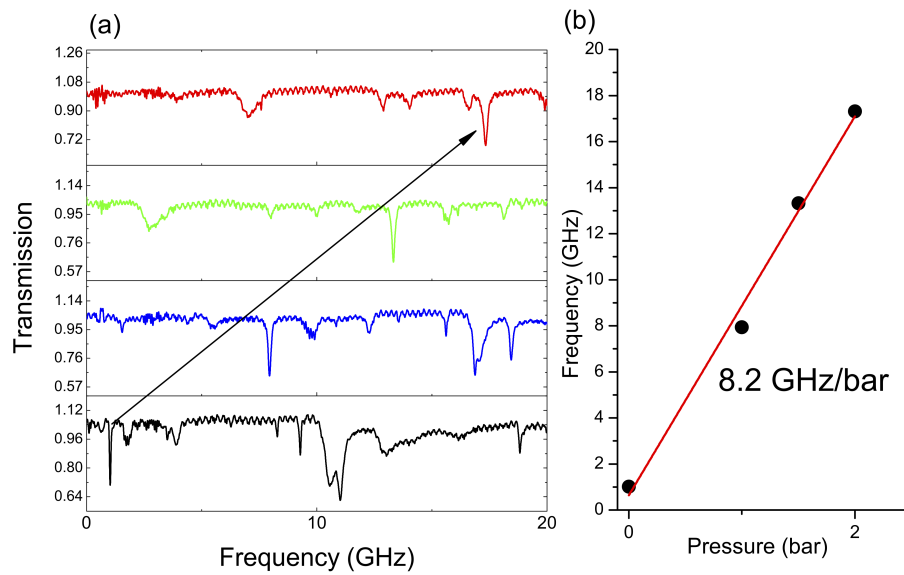


Figure 6.5: (a) The transmission spectra at 1535.66 nm for different pressure. From the bottom to the top are transmission spectra at 0, 1, 1.5, 2 bar, respectively. The arrow shows the direction of the WGM shift due to the increase of the internal pressure. (b) Pressure tuning sensitivity fitted from the transmission spectra.

the visible range and into the transparency window for water-based fluids in the core. This technique can also be viewed as a sensing technique. In such a context, the linewidth of the laser may be much narrower than the linewidth of the transmission dip [87], therefore the sensitivity could be much higher than simply using a pump laser and measuring distortion to the transmission dip. In principle, sensing has also been achieved in other WGM cavities; for example, refractive index sensing [52, 61], flow rate sensing [172], and biosensing [19, 39, 54, 56–58]. Such applications should also be possible with an MBR. In particular, for sensing applications with liquids, stable optical coupling via a tapered fiber on the outside of the bubble can be used, while the sensing targets flow through the interior of the resonator.

Chapter 7

Frequency Comb Generation in a Microbubble Resonator¹

7.1 Introduction

In this chapter, we exploit some nonlinear optics features of microbubble resonators to provide a controllable method for frequency comb generation. In an MBR structure, the resonance condition depends on the wall thickness. The eigenfrequencies are distorted from the solid bulk microresonators. In a normal silica microsphere resonator, the phase matching condition for parametric oscillation can be achieved at wavelengths near or longer than 1550 nm [124]. This can be pushed to shorter, or even visible, wavelengths by decreasing the wall thickness of the microbubble [119, 137]. We experimentally demonstrate comb generation centered near 780 nm using a microbubble, thereby verifying the prediction made in [137] and opening a window for frequency comb generation at a visible waveband in WGMRs.

7.2 Theory

7.2.1 Four-Wave Mixing

Hyper-parametric oscillation (or spontaneous four-wave mixing) is generated due to the nonlinear polarization of a medium to a coupled electromagnetic wave. When laser light is coupled into a medium, the relation between the input electric field and

¹This work is published in Y. Yang, X. Jiang, S. Kasumie, G. Zhao, L. Xu, J. M. Ward, L. Yang, and S. Nic Chormaic, "Four-wave mixing parametric oscillation and frequency comb generation at visible wavelengths in a silica microbubble resonator", *Opt. Lett.* **41**, 5266-5269 (2016) [173]. S. Kasumie contributed to the fabrication of the MBR, making measurements, writing of the paper, and, later, improving the comb generation to extend it further into the visible region. The measurement was done in the Micro/Nano Photonics Laboratory, Department of Electrical and Systems Engineering, Washington University in St. Louis, USA during a 3-month research visit by S. Kasumie. Some sections are also published in S. Kasumie, Y. Yang J. M. Ward, and S. Nic Chormaic, "Toward visible frequency comb generation using a hollow WGM resonator", *Rev. Las. Eng.* **46**, 92 (2018) [50], a review article mainly written by S. Kasumie.

polarization is described using the Taylor expansion as

$$P_i = \epsilon_0 \left(\chi_{ij}^{(1)} E_j + \Sigma_{jkl} \chi_{ijk}^{(2)} E_j E_k + \Sigma_{jkl} \chi_{ijkl}^{(3)} E_j E_k E_l + \dots \right). \quad (7.1)$$

Here, P is the dielectric polarization density, E is the input electric field, and ϵ_0 is the vacuum permittivity. The first term describes the linear response to the input field. The second term describes a second order nonlinearity, which is negligible in silica glass due to inversion symmetry. We are interested in the third term, where the first nonlinearity contribution of silica glass exists. The susceptibility tensor, χ , in an isotropic media, here silica glass, is constant. The equation is simplified as

$$P = \epsilon_0 \left(\chi^{(1)} E + \chi^{(3)} E^3 + \dots \right). \quad (7.2)$$

Here, we substitute two light fields, $E = \frac{E_1}{2} e^{i(k_1 z - \omega_1 t)} + c.c. + \frac{E_2}{2} e^{i(k_2 z - \omega_2 t)} + c.c.$, into the third nonlinearity term. The term with $E_1 E_1 E_2^*$ describes a (degenerate) four-wave mixing process

$$E^3 = \dots + E_1 E_1 E_2^* e^{i(2k_1 - k_2)z - (2\omega_1 - \omega_2)t} + \dots \quad (7.3)$$

Here, another wave whose frequency and wave vector are $\omega_3 = 2\omega_1 - \omega_2$ and $k_3 = 2k_1 - k_2$ is predicted. However, for the predicted wave to exist, energy conservation and momentum conservation must be satisfied. Momentum conservation is always satisfied in a WGM resonator as the wavenumber is given by $2\pi m/r_0$, with the mode number m . For energy conservation, we consider the phase matching condition. When ω_1 and ω_2 are near each other, suppose the difference is $\Delta\omega = |\omega_2 - \omega_1|$. Then the phase mismatching is described as

$$\Delta k = 2k_1 - k_2 - k_3 \quad (7.4)$$

$$= 2k(\omega_1) - k(\omega_1 + \Delta\omega) - k(\omega_1 - \Delta\omega) \quad (7.5)$$

$$= 2k(\omega_1) - \left[k(\omega_1) + \Delta\omega \left. \frac{dk}{d\omega} \right|_{\omega_1} + \frac{\Delta\omega^2}{2} \left. \frac{d^2k}{d\omega^2} \right|_{\omega_1} + \dots \right] \quad (7.6)$$

$$- \left[k(\omega_1) - \Delta\omega \left. \frac{dk}{d\omega} \right|_{\omega_1} + \frac{\Delta\omega^2}{2} \left. \frac{d^2k}{d\omega^2} \right|_{\omega_1} + \dots \right] \quad (7.7)$$

$$= -(\Delta\omega)^2 \left. \frac{d^2k}{d\omega^2} \right|_{\omega_1}. \quad (7.8)$$

When $\Delta k = 0$, the phase matching condition is achieved and the corresponding wavelength is called the *zero dispersion wavelength* (ZDW). The process is cascaded as long as the phase matching condition is satisfied. In a real laser setup, a single pump laser at ω_1 and the vacuum fluctuation correspond to the two fields. In principle, any frequency of the vacuum fluctuation can be regarded as the second field. Comb generation is only achieved when the frequencies correspond to resonant frequencies. If the second field is at ω_2 , even if the second light field is weak, the pump power exceeding the threshold transfers the fluctuation to the third light field at ω_3 , which then acts as the second light field where it is subsequently transferred to ω_2 . The process repeats so that a single pump laser can excite many resonant modes and generate the frequency comb.

In conventional microresonators, material dispersion is dominant. Therefore, the waveband of the generated frequency is also restricted by the material dispersion. In a

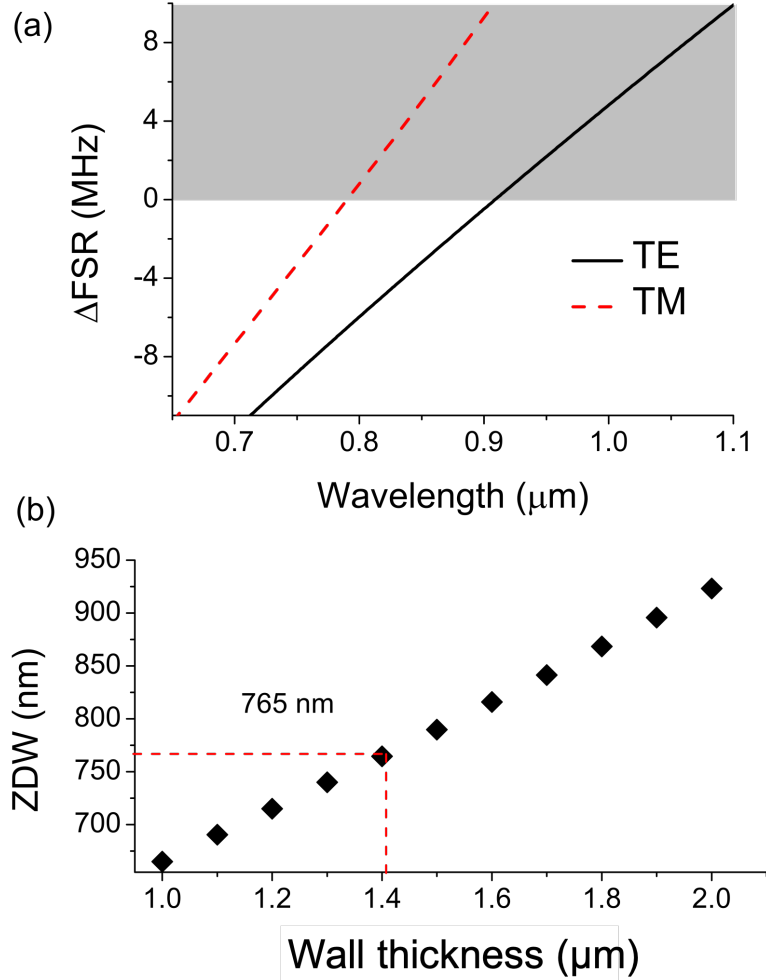


Figure 7.1: (a) Total dispersion (in terms of derivation of the FSR) of WGMs in a microbubble with a wall thickness of $1.5 \mu\text{m}$. The gray area is the anomalous dispersion region. (b) Zero dispersion wavelength of a microbubble with a wall thickness varying from $1.0 \mu\text{m}$ to $2.0 \mu\text{m}$, simulated in MATLAB. The radius $r = 80 \mu\text{m}$

silica WGM resonator, the frequency comb is generated near 1550 nm as this is where its ZDW resides [114, 164]. However, the resonant vacuum wavenumber, k_0 , is generally engineerable.

As has been shown earlier in Chapter 2, for the input light field to be resonant with the MBR, k_0 must satisfy the characteristic , Eqn. (2.26) and (2.27). The total dispersion is obtained by calculating the differences in the free spectral ranges based on k_0 . In Fig. 7.1(a), we show the dispersion of an MBR with a diameter of $120 \mu\text{m}$ and a wall thickness of $1.5 \mu\text{m}$. The TE and TM modes have different dispersions, as explained in [174]. We see that, for the TM mode, the ZDW is about 790 nm . For longer wavelengths, the MBR is in the anomalous dispersion regime (shown by the gray area in Fig. 7.1(a)), where four-wave mixing can be phase matched [119, 122]. The calculated ZDW for different wall thicknesses is plotted in Fig. 7.1(b). To shift the ZDW to 765 nm , the wall thickness should be reduced to around $1.4 \mu\text{m}$. The

threshold for FWM depends on Q^2/V , where V is the WGM volume. Q is lower for a thinner MBR; therefore, its geometrical parameters should be optimized [137]. In practice, obtaining an MBR with a high enough Q was a major technical challenge until an improved fabrication process was developed [13].

7.3 Experiment

The microbubble was fabricated using a CO₂ laser. The fabrication method is detailed in Chapter 3. To obtain the desired wall thickness of around 1.4 μm , we chose a silica capillary with an inner and outer diameter of 100 μm and 375 μm , respectively, which we subsequently tapered down to an outer diameter of 29 μm by a heat-and-pull technique. The tapered microcapillary was then connected to dry nitrogen gas with an aerostatic pressure of about 2.5 bars. By heating the microcapillary on both sides using the CO₂ laser beams, its wall softens and swells, and the process can be monitored on a CCD camera. When the outer diameter of the bubble reached about 120 μm , the process was stopped. The geometric parameters were estimated under a microscope, see Fig. 7.2(a). A more precise measurement of the wall thickness was implemented after the experiment by breaking the microbubble near the middle and performing scanning electron microscopy (SEM), as seen in Fig. 7.2(b). The cross-section in Fig. 7.2(b) is slightly removed from the equatorial plane of the MBR, and the estimated wall thickness on the SEM is equal to or less than 1.5 μm . In practice, the inner profile of an MBR is elliptical and the wall is thinner in the equatorial plane. Therefore, the actual wall thickness at the equator is even thinner than what was measured here, thereby guaranteeing anomalous dispersion at 765 nm where the Kerr effect (i.e., self-phase modulation and cross-phase modulation) can compensate for the phase matching condition.

A tapered fiber was used to couple light into and out of the MBR; a single-mode fiber (in the wavelength bandwidth of 780 nm) was tapered down to a diameter of less than 1 μm . The total light propagation efficiency of the taper was about 70%. The MBR was placed on a 3D nano-stage to control the coupling between the resonator and the tapered fiber. In order to excite and measure FWM and the frequency comb generated in the MBR, a setup as illustrated in Fig. 7.2(c) was used. The pump power from a tunable laser diode (New Focus TLB-6712-P), centered at 765 nm, was coupled into the MBR through the tapered fiber. A maximum power of 6 mW could be coupled into the MBR. After the light coupled out of the MBR, it passed through a 50/50 inline beam splitter (BS). One output of the BS was connected to a photoreceiver (New Focus 1801), and the other was connected to an optical spectrum analyzer (OSA, HP 70950B) with a minimum resolution of 0.08 nm. In the measurement, the pump laser was scanned over 40 GHz around a high Q mode, and the transmission spectrum was recorded on a digital oscilloscope (Tektronics TDS 3014B). During the experiment, the coupling fiber was in contact with the MBR at the equatorial plane to maintain coupling stability.

A typical transmission spectrum and a resonance mode with a Q -factor of $\sim 2 \times 10^7$ are shown in Fig. 7.3. The span of the laser scan was then decreased until only the selected high Q mode (see inset of Fig. 7.3) was coupled to the MBR. As the

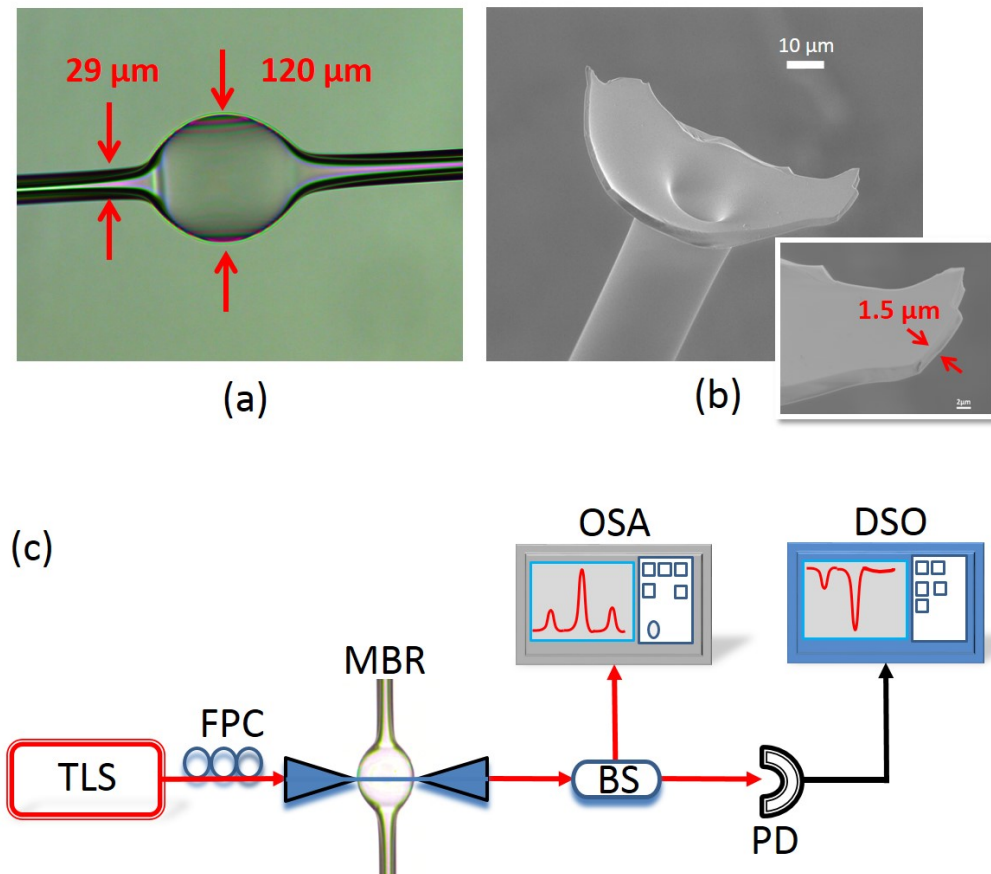


Figure 7.2: (a) Microscope image of the MBR. The diameter is measured to be 120 μm . (b) SEM image showing the cross-section of the MBR. The typical wall thickness is 1.5 μm , as shown in the inset. The actual wall thickness should be less than this, as explained in the main text. (c) Experimental setup for measuring the frequency comb in the MBR. TLS, tunable laser source; BS, beam splitter; FPC, fiber polarization controller; PD, photodetector; OSA, optical spectrum analyzer; DSO, digital storage oscilloscope.

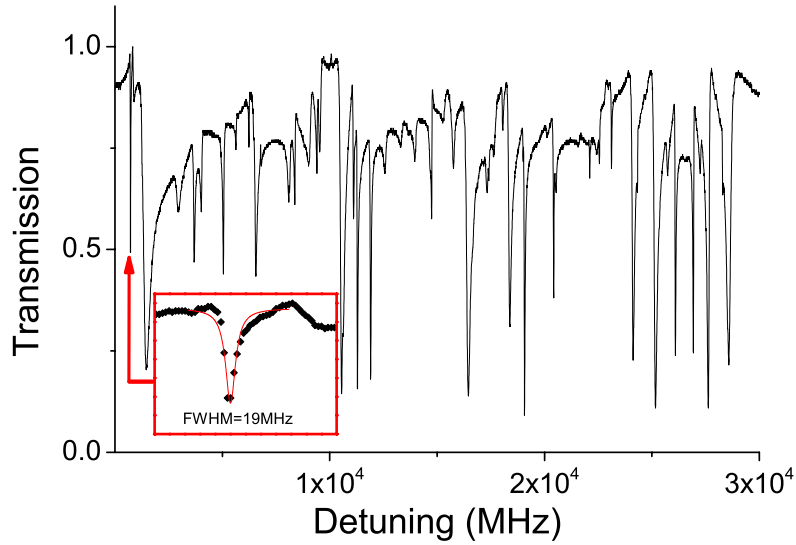


Figure 7.3: Transmission spectrum of the MBR. The inset shows the transmission of the pump WGM in the experiment. The red curve is a Lorentzian fit with a FWHM of about 19 MHz, corresponding to a Q-factor of about 2×10^7 .

simulation results indicate, the TE and TM modes in the MBR have different ZDWs. To effectively excite the TM mode, a fiber polarization controller (FPC) was used between the laser source and the tapered fiber. A typical FWM spectrum is presented in Fig. 7.4 with an input power of ~ 3 mW at a pump wavelength of 766.45 nm. The symmetric equidistant lines on either side of the pump (which is the highest peak of the spectrum) are separated by 2.1 nm, roughly twice the calculated FSR of 1.1 nm.

Next, we kept increasing the input power of the pump laser and more modes were excited via the degenerate FWM process and the subsequent, nondegenerate FWM until parametric oscillation occurred. Figure 7.5 shows the resulting spectrum at a power level of around 6 mW. Here, 14 peaks are visible, and the separation between adjacent lines is only one FSR (1.1 nm). More comb lines appear in Fig. 7.5, compared to Fig. 7.4 due to the complicated nonlinear interactions between modes. In this case, a natively mode-spaced comb has been generated [175].

7.4 Improvement to the Frequency Comb

To obtain a frequency comb at a shorter wavelength and with more comb lines, a laser amplifier (Toptica BoosTA) was introduced to the setup. An MBR with 152 μm diameter and 1.36 μm wall thickness was fabricated. An improved frequency comb with more than 40 comb lines was obtained, centered at 780 nm wavelength (see Fig. 7.6) The central wavelength is essential to push the comb band to shorter wavelengths; however, we were unable to achieve this in the experimental setup described in this thesis, but the work is ongoing in the research unit. A broad bandwidth frequency comb is related to the flatness of the dispersion curve near the ZDW. This could be improved by fabricating an MBR with a larger diameter [137]. This also reduces the possibility

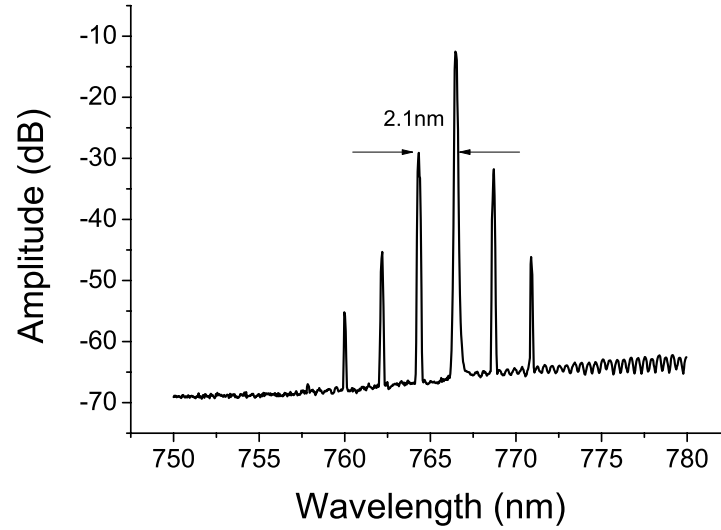


Figure 7.4: Four-wave mixing spectrum of the MBR with a diameter of $120 \mu\text{m}$, shown in Figs. 26(a) and 2(b). The separation between the peaks is 2.1 nm.

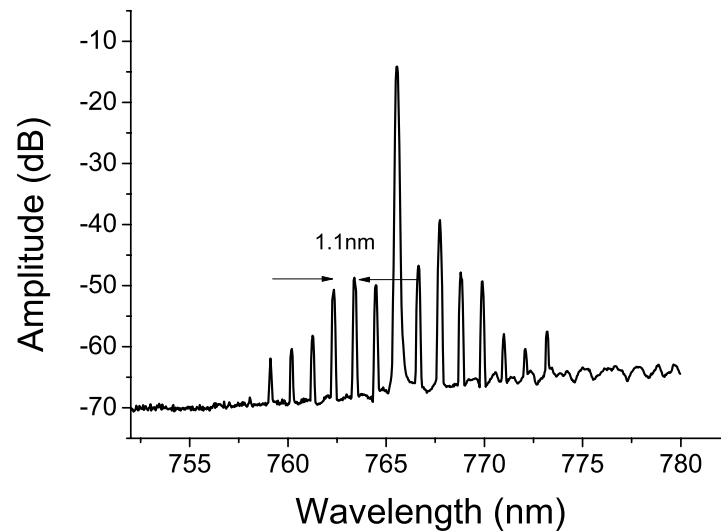


Figure 7.5: Frequency comb generation in the MBR at a center wavelength around 765 nm. Up to 14 comb lines are excited.

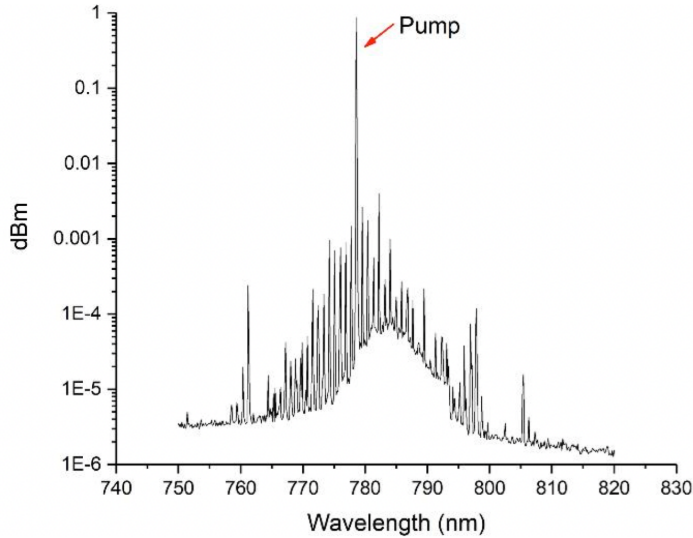


Figure 7.6: An improved Kerr frequency comb. More than 40 comb lines have been observed.

of exciting Raman scattering that competes with the comb generation process. In this case, mode locking is very likely to be achieved. We assume that light is coupled to an optical mode that is thermally broadened. There is the possibility that other optical modes are also involved in this method. However, as the optical mode that generates the frequency comb is rarely found ², we assume that the frequency comb is generated from a single optical mode. Unfortunately, we lost this optical mode during our measurements and, therefore, failed to determine its Q-factor. Here, the pump power was ~ 500 mW and was converted to comb lines of around tens or hundreds of μW . To improve the conversion efficiency, materials with a high third nonlinearity should be considered. We also need a small minimum ZDW so that the frequency comb can be generated in the visible range. So far, we have not identified a material that would greatly improve the generation of a visible frequency comb.

7.5 Conclusion

In conclusion, we have generated a Kerr frequency comb near the ZDW in a silica MBR by engineering the dispersion through optimizing the wall thickness and diameter of the MBR in a controllable way. The ZDW can be shifted beyond the limitation of the material's dispersion. We experimentally demonstrated FWM at 765 nm as a proof-of-principle. A frequency comb with multiple equidistant lines was generated by increasing the pump power to enter the parametric oscillation regime. The frequency comb generation was limited by the total available input power. The spectral bandwidth of the frequency comb increased with a higher power. In order to improve the frequency span of the comb, careful control of the dispersion is required; this could be implemented by introducing a small amount of curvature to the MBR. In practice, the wall thickness can be further decreased while still maintaining a high Q-factor [13].

²In this MBR sample, most optical modes produce Raman scattering instead of the Kerr comb.

Then, the center wavelength of the frequency comb could be shifted to an even shorter wavelength, until it is eventually limited by the material absorption window. This mechanism of dispersion engineering could be used for other materials [174], in particular, glass materials with high nonlinearity [176]. In the future, an improved frequency comb in the visible wavelength range may be realized and researchers in our unit are currently pursuing this.

Chapter 8

Raman Laser Switching Induced by Cascaded Light Scattering¹

8.1 Introduction

Finally, as part of this thesis work, we explore how the tunability of a microbubble may control the dynamics of laser emissions. In particular, we focus on the dynamics of stimulated Raman scattering. Stimulated light scattering, such as stimulated Raman scattering (SRS) and stimulated Brillouin scattering (SBS), can lead to the generation of coherent photons in different materials and geometries [104, 178]. Unlike conventional inversion lasers, the emissions of stimulated scattering lasers are not limited to specific wavebands, since no real energy levels are required; this provides unique advantages in many applications, e.g., arbitrary wavelength conversion [142, 179, 180], high-quality microwave generation [181], gyroscopes [182], sensing [103, 183–186], mode control [187, 188], etc. Considering that the stimulated gain arises from coherent coupling between a pump field and a Stokes field mediated by another field, e.g., a phonon field, the newly generated Stokes field may also act as a pump for the generation of further Stokes fields - an effect known as cascaded light scattering (CLS), resulting in cascaded Raman and Brillouin lasers [138, 143, 189–191]. Due to the presence of CLS, stimulated lasers are usually multimode when a high pump power is applied. Nevertheless, it is generally assumed that the dynamics of stimulated lasers involving CLS is trivial and usually attention is focused on the interactions of pump and Stokes waves. This is indeed true for Brillouin lasers because of the phase-matching condition [138, 139]. However, in Raman lasers, as the phase-matching condition is automatically satisfied [142], see Fig.8.1(a) [104], CLS could lead to many lasing modes being coupled together, thence rendering the behavior of such lasers to be quite unique, especially for multimode lasing [192, 193]. As a specific example, in this chapter, we show, both theoretically and experimentally, that CLS can induce mode-switching in multimode Raman lasers. This study illustrates the importance of considering CLS effects for Raman lasing in dielectric resonators.

¹This work appears in S. Kasumie, F. Lei, J. M. Ward, X. Jiang, L. Yang, and S. Nic Chormaic "Raman laser switching induced by cascaded light scattering", arXiv:1902.02487 (2019) [177]. S. Kasumie contributed to theory development, experimental verification, and writing the manuscript.

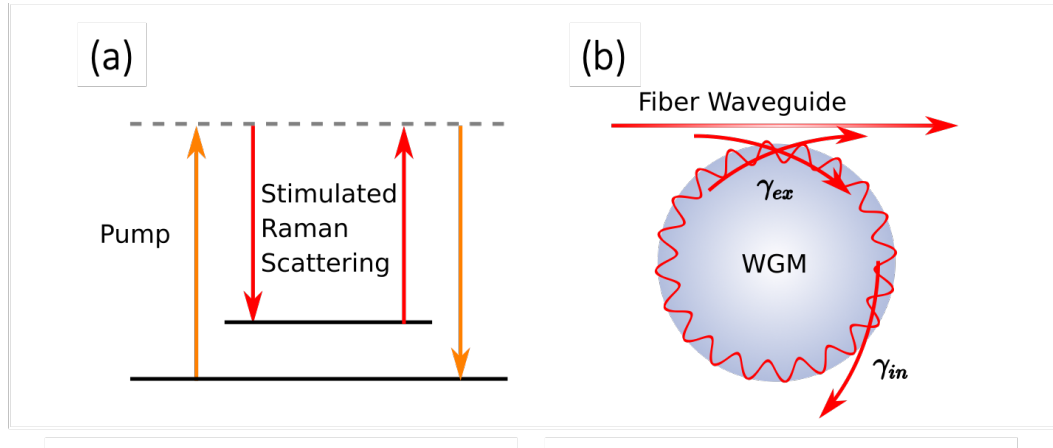


Figure 8.1: (a) Schematic diagram of the stimulated Raman scattering process. (b) Schematic of the experimental system. The input laser is coupled to a silica microsphere resonator through a tapered fiber waveguide, with a coupling constant, γ_{ex} , and resonator intrinsic loss, γ_{in} . Comparison of the gain spectrum and the lasing modes between (c) a typical homogeneously broadened laser and (d) a silica Raman laser. Schematic of (e) a cascaded Raman laser in single-mode fashion and (f) a two-mode Raman laser.

In this work, a whispering gallery mode (WGM) silica Raman laser is chosen as the experimental platform [194]. As depicted in Fig. 8.1(b), the light fields can be coupled into and out of the WGM resonator through a waveguide. The Stokes light (i.e., the Raman laser) can be generated in a WGM resonator as long as the following requirements are met: (i) the frequency of the Stokes light coincides with a high Q WGM and (ii) the Stokes mode has sufficient spatial overlap with the pump mode, i.e., mode overlap. With a single-mode pump, the Raman gain of a silica matrix can be considered to be homogeneously broadened if one neglects CLS, see Fig. 8.2(a). Under this circumstance, only the mode with the highest gain can lase, even if all the modes have the same losses, i.e., Q-factors, since the gain is clamped at the lasing threshold [195]. At this point, a question would naturally arise: how can one explain the frequent occurrence of multimode Raman lasing in a single-mode pumped microresonator?

Here, we show that, due to the existence of CLS, two (or multiple) modes with unequal gain provided by the pump, but equal cavity loss (more generally, unequal gain/cavity loss ratio) lase simultaneously, see Fig. 8.2(b). It is noteworthy to point out that this CLS-assisted, multimode lasing scenario differs from conventional cascaded single-mode Raman lasing, whereby a single mode is generated for each order of lasing, as shown in Fig. 8.2(c). The first order Raman lasing mode (Mode I), originating from the pump, could generate the subsequent Stokes field, i.e., the second order Raman laser (Mode II), and the typical frequency shift between the pump and Stokes is about 14 THz. In this case, the pump does not provide gain directly to the second (or even higher order) Stokes field. Hence, the power of this Raman laser usually decreases with increasing order, and it is impossible to obtain a higher order Raman signal without the presence of its previous order. The dynamics of such a typical cascaded laser can be simply treated as a cascaded energy transfer process; therefore it is trivial and does not

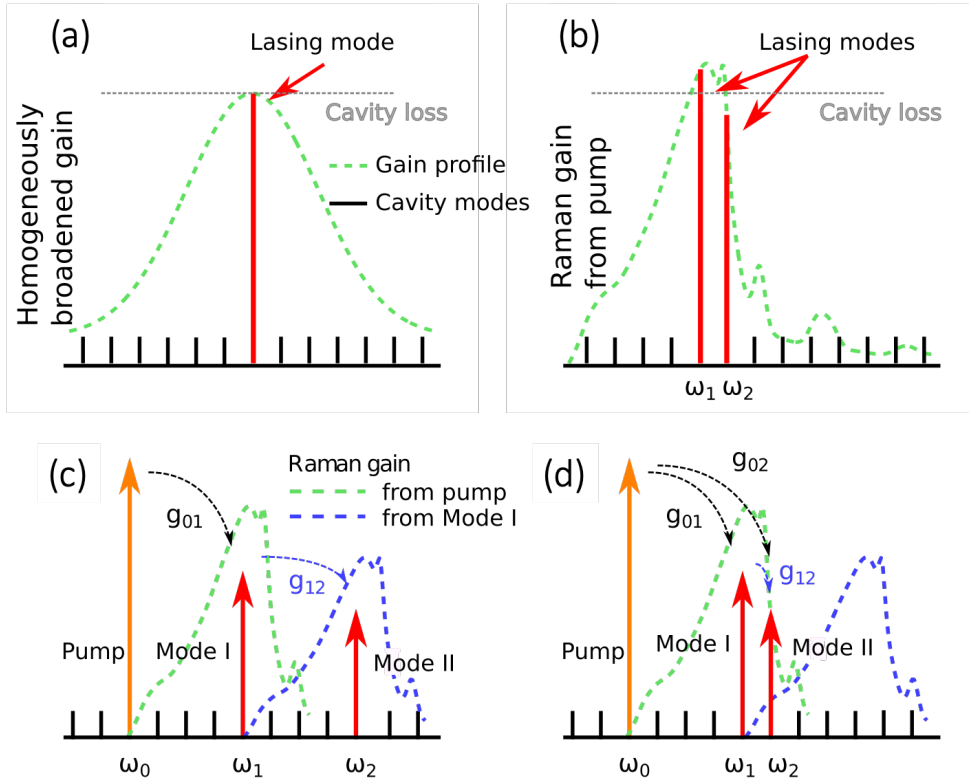


Figure 8.2: (a) a typical homogeneously broadened laser and (b) a silica Raman laser. Schematic of (c) a cascaded Raman laser in single-mode fashion and (d) a two-mode Raman laser.

differ much from the conventional single-mode lasing case. However, for the multimode lasing case, the presence of CLS can modulate the laser dynamics significantly. As illustrated in Fig. 8.2(d), two adjacent modes *in the same mode family* are excited simultaneously by a single-mode pump. Both Raman lasing modes derive their gain from the pump through SRS, but, at the same time, the first Raman mode interacts with the second due to CLS. Though the interaction may be weak, it is not negligible and can account for the existence of multimode Raman lasing, and may even play a subtle role in Raman laser switching.

Indeed, the CLS-induced coupling between the two lasing modes seems not so obvious and is easily overlooked. In textbooks, the SRS is usually illustrated with two light fields and a simplified two level system, as shown in Fig. 8.1(a). However, in real solid materials, like silica [196], silicon [197], or silicon carbide [198], the Raman gain profile is not simply composed of only a few discrete peaks, but rather it is a continuum; therefore, it is natural to introduce a coupling term between the two lasing modes. To control the emission pattern, such as the observed switching between Fig. 8.2(c) and Fig. 8.2(d) when using an MBR, the coupling terms should also be introduced.

8.2 Theory

To understand the multimode Raman laser (see Fig. 8.2(d)), the standard coupled-mode equations must be modified [143] to include *all* the CLS terms. Given a certain j th cavity mode, it couples to the external driving pump in the waveguide via the overlap of the evanescent fields, and to *all* the other cavity modes through SRS. We introduce a summation term into the coupled-mode equations to represent the interactions of the cavity modes. The motion of the intracavity field, E_j , can now be described as

$$\begin{aligned} \dot{E}_j = & \left(-\frac{\gamma_j}{2} + \sum_{i < j} g_{ij} |E_i|^2 - \sum_{k > j} g_{jk} \frac{\omega_j}{\omega_k} |E_k|^2 \right) E_j \\ & + \sqrt{\gamma_{ex,0}} \delta_{0,j} s, \end{aligned} \quad (8.1)$$

where i , j , and k are mode order indices and the resonant frequencies decrease with the order (the order of the pump mode is set to be 0). The γ_j and $\gamma_{ex,j}$ denote the total energy decay rate and the extrinsic decay rate into the waveguide, respectively, ω_j is the resonant frequency, $I_0 = |s|^2$ is the input pump power from the waveguide, and δ is the Kronecker delta function, where $\delta_{ij} = 1$ if and only if $i = j$. We set g_{ij} as the intracavity Raman gain coefficient between mode i and j , proportional to the Raman gain spectrum of the bulk silica, $g_R(|\omega_i - \omega_j|)$ [143, 196]. Note that the Raman gain spectrum will not be modified due to the effect of cavity quantum electrodynamics (cQED) [199]. The second and third terms in Eq. (8.1) describe the gain and the loss caused by the SRS from the higher and lower frequency modes, respectively. It is important to point out that the coherent anti-Stokes Raman scattering is not included in the model since the phase-matching condition is not easily satisfied, as discussed later.

In order to gain insight into this phenomenon, we consider the simplest case, i.e., one pump mode and two Raman lasing modes, see Fig. 8.2(d). The intracavity powers for steady-state are governed by

$$P_0 \left(-\frac{\gamma_0}{2} - g_{01} \frac{\omega_0}{\omega_1} P_1 - g_{02} \frac{\omega_0}{\omega_2} P_2 \right)^2 = \gamma_{ex,0} I_0, \quad (8.2)$$

$$P_1 \left(-\frac{\gamma_1}{2} + g_{01} P_0 - g_{12} \frac{\omega_1}{\omega_2} P_2 \right) = 0, \quad (8.3)$$

$$P_2 \left(-\frac{\gamma_2}{2} + g_{02} P_0 + g_{12} P_1 \right) = 0, \quad (8.4)$$

where P_0 , P_1 , and P_2 represent the intracavity power for the pump, the first (Mode I), and the second lasing mode (Mode II), respectively. There are four different steady-state regimes as I_0 is increased, see Figs. 8.3(a) and (b). Mode I is located in the vicinity of the peak of the Raman gain profile, while Mode II has a lower resonant frequency and a relatively lower Raman gain coefficient. Therefore, Mode I lases first, as long as its gain can overcome its loss (regime II), as shown in Figs. 8.3(a) and (b). One can see that P_1 continues to increase with I_0 , but the intracavity pump power, P_0 , is clamped at $\gamma_1/2g_{01}$. Thus, Mode II cannot derive sufficient gain solely from the

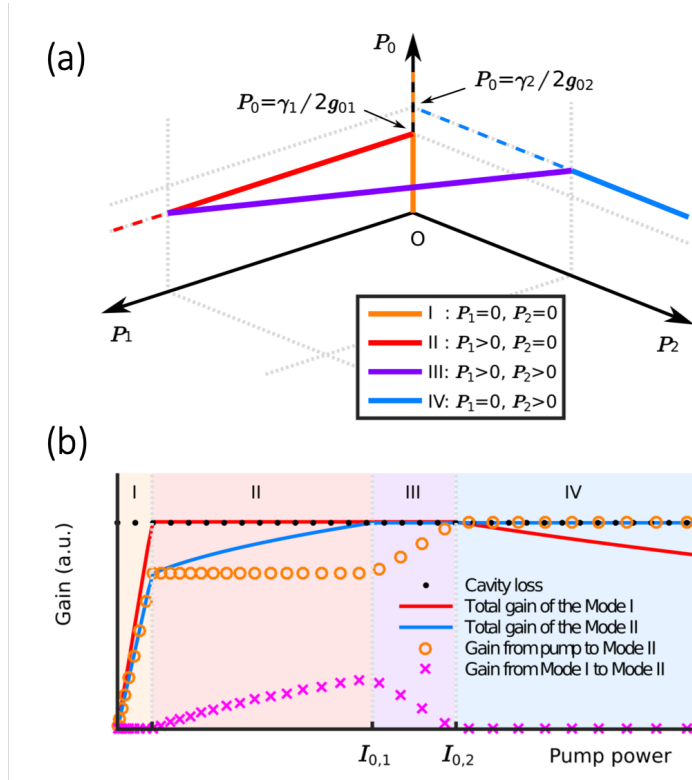


Figure 8.3: Simulation results based on Eq. (8.1) (see Appendix C for details). (a) P_0 , P_1 , and P_2 represent the intracavity powers of the pump, the first, and the second Raman fields. The external pump power is increased when detuning is set to 0. Solid lines represent the stable, steady state, while the dashed lines correspond to unstable cases. (b) The total gain of the two Raman modes and gain fraction from pump and Mode I to Mode II. The parameters used in (b) are $\gamma_j = 25.3 \mu\text{s}^{-1}$ and $\gamma_{ex,j} = 26.2 \mu\text{s}^{-1}$ for all $j = 0, 1, 2$; the angular frequencies are $\omega_0 = 2\pi \times 390.6$ THz, $\omega_1 = 2\pi \times 377$ THz and $\omega_2 = 2\pi \times 375.3$ THz; and the intracavity Raman gain coefficients are $g_{01} = 3.6 \times 10^{18} \text{ s}^{-1} \text{ J}^{-1}$, $g_{02} = 2.7 \times 10^{18} \text{ s}^{-1} \text{ J}^{-1}$ and $g_{12} = 0.5 \times 10^{18} \text{ s}^{-1} \text{ J}^{-1}$.

pump field to start lasing. However, as shown in Fig. 8.3(b), Mode I can also provide a gain mechanism for Mode II proportional to P_1 , the second mode can be excited and the system undergoes a transcritical bifurcation when

$$I_{0,1} = \frac{\gamma_1}{8\gamma_{ex,0}g_{01}} \left[\gamma_0 + \frac{1}{g_{12}} \frac{\omega_0}{\omega_1} (g_{01}\gamma_2 - g_{02}\gamma_1) \right]^2, \quad (8.5)$$

which can be obtained by taking $P_2 = 0$ and $-\gamma_2/2 + g_{02}P_0 + g_{12}P_1 = 0$ into Eqs. (8.2)-(8.4).

As a consequence of the appearance of Mode II (regime III), Mode I is gradually suppressed, since the former opens a loss path for the latter through SRS [104], with the loss being proportional to P_2 . When two Raman modes lase simultaneously, P_1 and P_2 are determined from a simple linear relationship

$$g_{01}P_1 + g_{02} \frac{\omega_1}{\omega_2} P_2 = \frac{(g_{01}\gamma_2 - g_{02}\gamma_1)}{2g_{12}}. \quad (8.6)$$

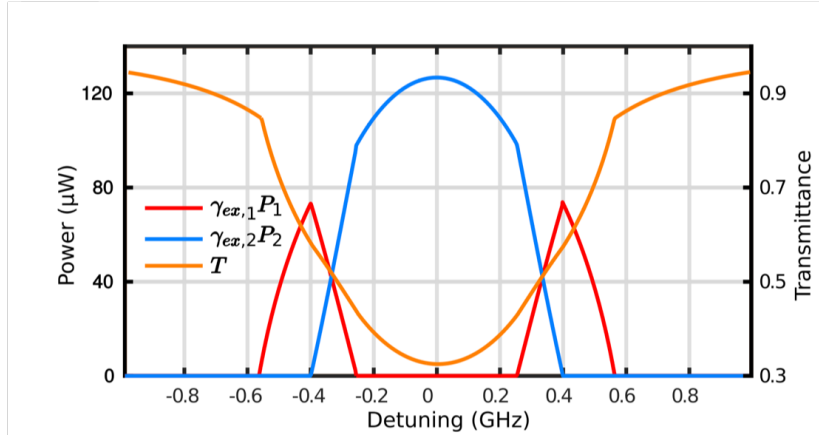


Figure 8.4: The output of two Raman lasers and the transmission spectrum (T) of the pump mode as it evolves with pump detuning. The input power is fixed at $I_0 = 0.6$ mW. Other parameters are the same as those in Fig. 8.3(b).

Clearly, both modes are still influenced by I_0 . In the two-mode lasing regime, the intracavity pump power, P_0 , increases with I_0 , while P_1 reduces with I_0 until²

$$I_{0,2} = \frac{\gamma_2}{8\gamma_{ex,0}g_{02}} \left[\gamma_0 + \frac{1}{g_{12}} \frac{\omega_0}{\omega_1} (g_{01}\gamma_2 - g_{02}\gamma_1) \right]^2, \quad (8.7)$$

where Mode I is completely switched off, see Figs. 8.3(a) and (b). Even with further increasing of the pump, Mode I cannot be turned on again and only Mode II remains on (regime IV). This counterintuitive phenomenon, can be explained by the fact that the existence of Mode II reduces the Q-factor of Mode I [188], and, as a result, the threshold of Mode I increases with P_2 and cannot be reached even if the pump power, I_0 , keeps increasing. This case has no correspondence with the conventional cascaded single-mode Raman laser. Therefore, the mode switching induced by CLS cannot be readily illustrated as an unidirectional energy transfer between two lasing modes, while in fact it implies that the weak mode interaction could modulate the lasing dynamics of multimode lasers dramatically.

It is worth mentioning that there is no hysteresis phenomenon when the pump power, I_0 , is ramped down; hence, it is possible to control the lasing modes simply by changing I_0 . It is convenient to control the intracavity power, P_0 , by changing the relative detuning of the pump and cavity modes; therefore, we perform the numerical calculations for the scanning pump case, as shown in Fig. 8.4(c). It turns out that the four regimes can be achieved by controlling the detuning. As the detuning decreases, Mode I is excited first. Further detuning simultaneously turns on Mode II and suppresses Mode I. When the system is operated close to resonance, Mode I is annihilated completely and Mode II keeps growing until maximum coupling is reached.

Generally, the emission pattern is not always identical to what has been considered above (see Fig. 8.2(d)). If we assume that the emission threshold of each mode is described by the gain coefficient, g_{ij} , which itself depends on the resonant frequency,

²Similar to Eq. (8.5), when the system is at the transition point, $P_1 = 0$ and $\frac{-\gamma_1}{2} + g_{01}P_0 - g_{12}\frac{\omega_1}{\omega_2}P_2 = 0$ should be satisfied.

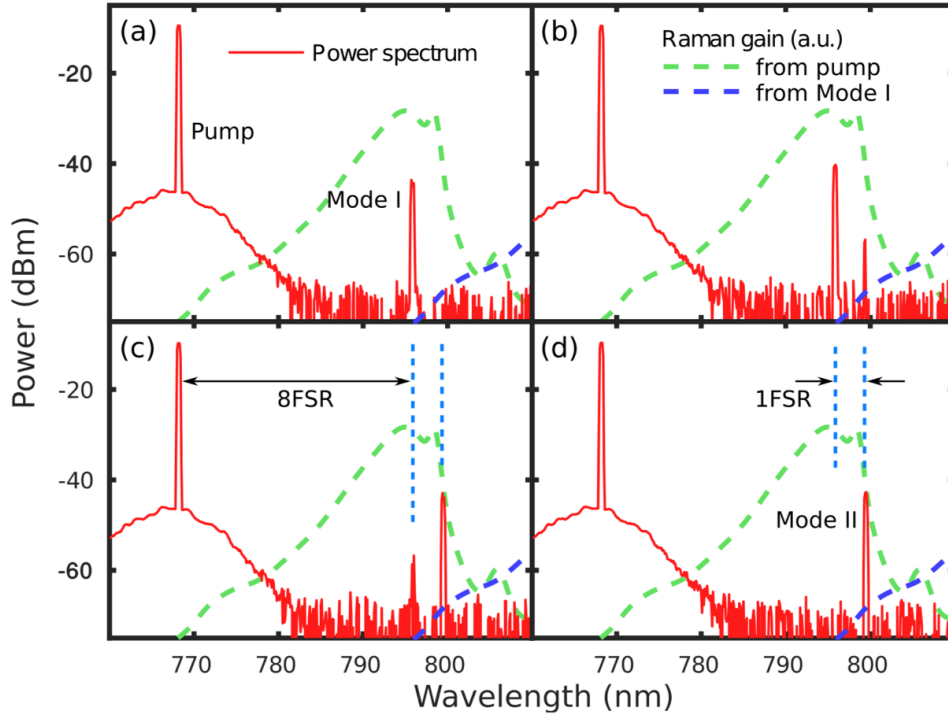


Figure 8.5: Switching process of the Raman lines is observed by scanning the pump laser in the blue-detuned region of a cavity mode at 768.1 nm. From (a) to (d), the detuning of the pump is approximately set at 20 MHz, 18 MHz, 15 MHz and 10 MHz, respectively. (a) The first Raman laser at 795.9 nm appears (Mode I). (b) The second Raman line (Mode II) at 799.4 nm appears. (c) Mode I is suppressed while Mode II becomes stronger. (d) Mode I is annihilated and only Mode II remains.

in principle, we can alter the emission pattern by engineering the resonant frequency. This can be achieved by using an MBR.

8.3 Experiment

To experimentally confirm the mode switching, we performed measurements using a silica microsphere with a diameter of around $41.5 \mu\text{m}$, fabricated from a standard optical fiber reflowed by a CO_2 laser [200]. A tapered optical fiber was used to couple the pump light into the cavity through evanescent coupling, see Fig. 8.1(b). The output laser was divided into two paths, one for observing the transmission spectrum of the WGM resonator and the other for observing the Raman lasing spectrum. The transmission spectrum was recorded using a photodiode connected to a digital oscilloscope, and was used for locking the pump to the WGM. The Raman lasing spectrum was measured by an optical spectrum analyzer (OSA). To avoid parametric oscillation and coherent anti-Stokes Raman scattering, the pump wavelength was set to 768.1 nm - this corresponds to the normal dispersion regime for silica [161, 201]. The input laser power was approximately $500 \mu\text{W}$, and the laser frequency was finely tuned and ther-

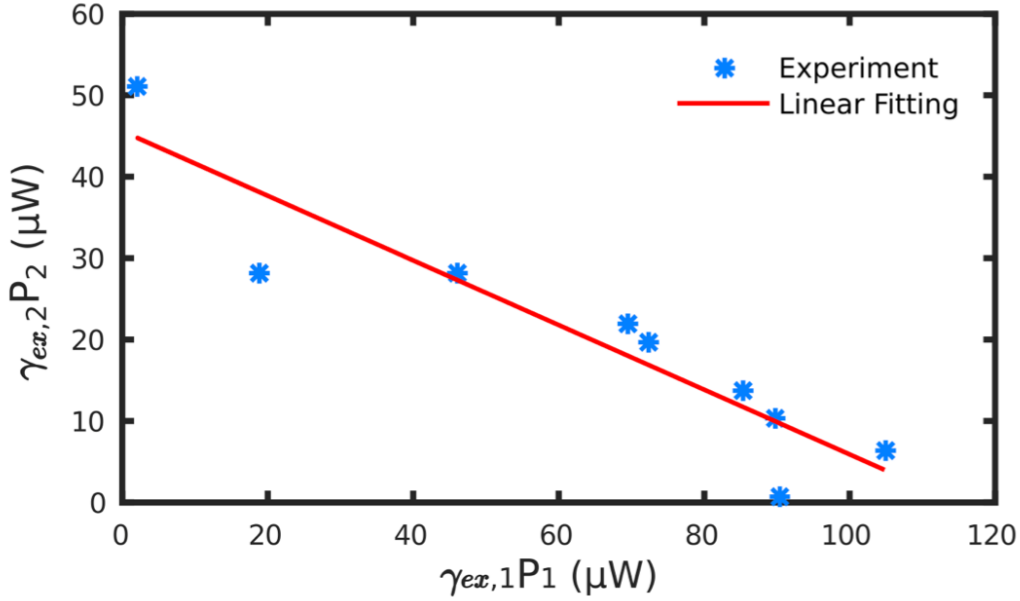


Figure 8.6: The output powers of Mode I and Mode II are negatively and linearly correlated with each other.

mally locked to a cavity mode [73] with a Q-factor of 9.7×10^7 . During the thermal locking process, both the pump and lasing modes were red shifted, thus their frequency intervals remain nearly unchanged, and the change of the Raman gain can be negligible as well.

The experimental results are presented in Fig. 8.5. As the laser frequency approaches resonance, the first Raman lasing mode (Mode I) at 795.9 nm is excited, with its power increasing as the detuning decreases until the second Raman lasing mode (Mode II) at 799.4 nm appears. With a further reduction of the detuning, power switching between the two Raman modes is observed, and, eventually, only Mode II remains on, as evidenced in Fig. 8.5(d). The output powers of both Mode I and Mode II during the switching process were measured and are plotted in Fig. 8.6.³

The powers of these two lasing modes are negatively and linearly correlated with each other during the switching process, in qualitative agreement with the theoretical model, see in Fig. 8.3(a) and Eq. (8.6). Note that the frequency spacings between the pump and two lasing modes are exactly integer numbers of the free spectral range (FSR), i.e., they belong to the same mode family and, therefore, have near unity mode overlap. Otherwise, overlap coefficients would need to be introduced into Eq. (8.1). The mode overlap is particularly important for a standing wave resonator in which the Raman gain saturation could intrinsically lead to stable, single-mode lasing at a high power [202]. This is because the CLS may be suppressed due to weak mode overlap as it may simply be too small to allow CLS to occur.

In these experiments, we selected resonators with a low number of high Q modes

³Note that we have only shown the switching process in the blue-detuned side. The symmetric switching process should also be observable in the red-detuned side, as shown in the simulation (see Fig. 8.4). However, this is difficult to measure experimentally due to the presence of thermal effects.

to avoid an overly complicated WGM spectrum and to reduce the chance of cascaded lasing beyond the first order. When we used an even higher pump power, or a smaller detuning, many high order cascaded lasing modes (up to at least 11 modes) were often observed. In some samples, we also observed the conventional cascaded lasing modes in single-mode fashion before the appearance of the second Raman lasing modes in the first order. This can be attributed to the differences in the Q-factors and the FSR for different resonators. There is an abundance of switching behaviors due to CLS when multiple lasing modes are involved; this is especially true when the phase-matching condition is satisfied and other nonlinear optical phenomena occur simultaneously. Further investigation into this process may be done using the MBR, since the FSR can be tuned by applying air pressure.

8.4 Conclusion

In conclusion, although a lot of interest has been garnered, and many applications have been demonstrated, few studies have focused on understanding the details of cascaded light scattering in Raman lasers. In addition to the switching process observed in the emission pattern, see Fig. 8.2(c), an MBR may be used to switch between different emission patterns. Recently, we have become aware of earlier works in a silica fiber [203] and in a silica rod WGM cavity [204] based on the same model. Here, we provide an detailed analytic method and insight for the model. In this work, we show that, aside from the application for extending the frequency range, naturally occurring CLS has a significant impact on the generation of Raman lasing and cannot be ignored when multiple modes are involved. Subsequently, it may have an impact on the realization of Kerr-frequency combs [147, 205–207], phase-locked Raman lasers [147, 208], and soliton generation [209–211]. Besides Raman lasers, this SRS interaction also exists in other lasers, such as rare-earth doped microlasers; thence, the mode switching induced by SRS could provide a strategy to achieve a wavelength-switchable laser via CLS in a variety of laser systems. Exploring this dynamically related phenomenon [212, 213] may find direct applications in all-optical, flip-flop memories [214], and switchable light sources.

Chapter 9

Conclusion

As we have shown in this dissertation, WGM optical resonators are useful tools for various applications and as test beds for fundamental physics. Light can be coupled into the WGM cavities through a tapered optical fiber and strong light-matter interactions with the cavity itself and its surroundings are obtainable. Sensing applications are possible, primarily due to the resonance condition change. Frequency generation and phase modulation effects are enhanced due to the material's nonlinear polarization in response to a resonant light field. In this thesis, the focus has been on using MBRs to develop sensing platforms and to study nonlinear optics phenomena.

We have discussed several ways of how MBRs can play a role in sensing. For example, they may be used as a platform for transient sensing. Until recently, transient sensing techniques have not been well developed. By assuming that a rectangular light pulse is coupled to a WGM resonator, we have proposed a theoretical model and solution when the Q-factor is high. The wave form transmittance in the time domain is composed of a sharp peak and a damped oscillation following the sharp peak. When the Q-factor is high, the sharp peak always exists and its height does not change significantly with dispersion and dissipation changes. In this case, we can evaluate the height of the less sharp peak for the purpose of sensing, i.e., the first peak of the damped oscillation region. By evaluating the less-sharp peak height, dispersive and dissipative transient sensing can be performed separately. When the Q-factor is low (i.e., $Q \sim 10^6$), the sharp peak height changes as a function of dissipative perturbations while the damped waveform followed by the sharp peak yields dispersive information. This give a possibility for sensing in a low Q condition and in the quasi-droplet regime with an MBR[24].

Alternatively, in a tapered fiber optically coupled system, sensitivity can depend on the coupling condition. Controlling the coupling condition by an optical force instead of mechanical stages, such as nanopositioners, would be preferable for practical applications. An optical force can be generated when two cavities share the same optical resonance and form a supermode. We reviewed supermodes and developed a theory to estimate the optical force obtainable. The MBR can play an important role for achieving excitation of supermodes in the coupled cavity system. An experimental result shows agreement with our theoretical prediction. However, the optical force attainable has not reached the level needed for a practical use with our existing WGM samples. Since the optical force is proportional to the Q-factor [85], it could be optimized by

using different materials, such as calcium fluoride crystals, where higher Q-factors than for silica resonators, can be achieved.

We have also presented sensing applications using an MBR-based microlaser. As the high sensitivity of the WGM cavity is due to the narrow linewidth of the resonant mode, retrieving information from a lasing mode can yield a higher sensitivity than the transmission dip through the coupling fiber. We demonstrated pressure sensing using an erbium ion doped MBR laser. However in principle, the sensing should not be limited to pressure. In particular, when an MBR is filled with liquid (i.e., its in quasi-droplet regime [24]), stable optical coupling could be maintained while the target inside the MBR is being detected. Different gain materials could also be used as dopants so the lasing could happen in a transparency window of the liquid.

Frequency generation is another major topic of study in the field of WGM cavities. We have generated a near visible frequency comb in an MBR resonator by engineering the geometrical dispersion of the cavity. The ZDW can be pushed to a shorter wavelength by reducing the wall thickness of the microbubble, therefore a visible frequency comb should be possible. With such a purpose in mind, high-quality microbubble reproducibility, pump power, and pump frequency could be optimized. The slope of dispersion near the ZDW is gentle when the MBR is large and this can widen the frequency band of the comb.

Recently, we have seen dark soliton-type frequency combs generated at a 480 nm wavelength in our laboratory. The generated dark solitons are not as unstable as previously predicted [132]. This may pave a way for practical use and steady development of dark soliton frequency combs.

Instead of broadening the possible frequency generation, the dynamics of the generated frequency are also an interesting topic to investigate. By assuming a simple model, where the pump laser is interacting with two lasing Raman modes, a switching process of cascaded Raman scattering has been predicted and studied both analytically and numerically. An experimental demonstration has verified the proposed switching process. The MBR should be a suitable platform for further investigation, particularly since different patterns of emission can be pressure tuned via internal air pressure in the MBR.

Finally, the frequency generation technique could be used in spectroscopy. The lasing condition needs to be further studied in order to retrieve detailed information in relation to this aspect. For example, in Eq. 8.6, the power of excited lasing modes depends on the Raman gain coefficient and damping rates of each mode. The Raman gain coefficients in whispering gallery modes depend on the resonant frequencies. Therefore, dispersive and dissipative information may be retrieved from the emission pattern. Once more, the MBR shows strong capability of supporting such applications.

Overall, this PhD work has covered many aspects behind whispering gallery mode resonators, with emphasis placed on using microbubble resonators. This has contributed significantly to the use of MBRs for both sensing applications and in nonlinear optics.

Appendix A

Appendix A: MATLAB Code for Field Distribution in a Microsphere

```
% Solving the resonant wavenumbers in a microsphere.
% This code can easily be extended to solve eigenmodes in microbubbles.
clear all
c = 3e8;
wavelength = 1.55*1e-6;
ref_Idex = 1.444;
r0 = 25e-6;
FSR = wavelength^2/(2*pi*ref_Idex*r0);
wlstep = 0.2*FSR;
WLStart = wavelength-5*FSR;
WLEnd = wavelength+5*FSR;
az_MNNum = round(2*pi*r0*ref_Idex/wavelength);
MNspan = 40;
AzMN = [az_MNNum-MNspan:az_MNNum+MNspan];
MNN = 2*MNspan+1;
k0 = 2*pi/wavelength;
stepkr = 0.01;
kStart = 2*pi/WLEnd;
kEnd = 2*pi/WLStart;
kstep = (kEnd-kStart)/100;
k = [kStart:kstep:kEnd];
nk = ref_Idex*k;
nkr0 = nk*r0;
coff = sqrt(pi./(2*nkr0));
% initialization
filter = round(length(k)/2);
accuracy = 10;
sphrBi = besselj(AzMN(1)+0.5,nkr0);
sphrBj = besselj(AzMN(2)+0.5,nkr0);
sphrBk = besselj(AzMN(3)+0.5,nkr0);
sphrHi = besselh(AzMN(1)+0.5,1,1i*nkr0);
```

```

sphrHj = besselh(AzMN(2)+0.5,1,li*nkr0);
sphrHk = besselh(AzMN(3)+0.5,1,li*nkr0);
dsphrBj = (nk.*(sphrBi-sphrBk)-sphrBj/r0)/2;
dsphrHj = (li*nk.*(sphrHi-sphrHk)-sphrHj/r0)/2;
optTEk = [];
optTMk = [];
TEAzMN = [];
TMAzMN = [];
diffTE = [];
diffTM = [];
TEBj = [];
TEdBj = [];
TEHj = [];
TEdHj = [];
TMBj = [];
TMdBj = [];
TMHj = [];
TMdHj = [];
for i = 1:MNN
kj = k;
BHdiffTE = log(dsphrBj.*sphrHj) - log(ref_Idex*dsphrHj.*sphrBj);
diffPlotTE = BHdiffTE;
absBHdiffTE = abs(BHdiffTE);
Threshold1 = max(absBHdiffTE)/100;
for j = 1:accuracy
sortmsmch = sort(absBHdiffTE);
msmchTH = sortmsmch(filter);
base = absBHdiffTE<msmchTH;
kj = relocX(kj,base); % kj with smaller 'absBHdiffTE' value is resolved and probed
if j == accuracy
if msmchTH<Threshold1
optTEk = [optTEk;kj];
TEAzMN = [TEAzMN;AzMN(i+1)];
diffTE = [diffTE;diffPlotTE];
TEBj = [TEBj;sphrBj];
TEdBj = [TEdBj;dsphrBj];
TEHj = [TEHj;sphrHj];
TEdHj = [TEdHj;dsphrHj];
end
break;
end
nkj = ref_Idex*kj;
nkjr0 = nkj*r0;
sphrBiTE = besselj(AzMN(i)+0.5,nkjr0);
sphrBjTE = besselj(AzMN(i+1)+0.5,nkjr0);
sphrBkTE = besselj(AzMN(i+2)+0.5,nkjr0);

```

```

sphrHiTE = besselh(AzMN(i)+0.5,1,1i*nkjr0);
sphrHjTE = besselh(AzMN(i+1)+0.5,1,1i*nkjr0);
sphrHkTE = besselh(AzMN(i+2)+0.5,1,1i*nkjr0);
dsphrBjTE = (nkj.*(sphrBiTE-sphrBkTE)-sphrBjTE/r0)/2;
dsphrHjTE = (1i*nkj.*(sphrHiTE-sphrHkTE)-sphrHjTE/r0)/2;
BHdiffTE = log(dsphrBjTE.*sphrHjTE) - log(ref_Idex*dsphrHjTE.*sphrBjTE);
absBHdiffTE = abs(BHdiffTE);
end
kj = k;
BHdiffTM = log(ref_Idex*dsphrBj.*sphrHj) - log(dsphrHj.*sphrBj);
diffPlotTM = BHdiffTM;
absBHdiffTM = abs(BHdiffTM);
Threshold1 = max(absBHdiffTM)/100;
for j = 1:accuracy
sortmsmch = sort(absBHdiffTM);
msmchTH = sortmsmch(filter);
base = absBHdiffTM<msmchTH;
kj = relocX(kj,base); % kj with smaller 'absBHdiffTM' value is resolved and probed
if j == accuracy
if msmchTH<Threshold1
optTMk = [optTMk;kj];
TMAzMN = [TMAzMN;AzMN(i+1)];
diffTM = [diffTM;diffPlotTM];
TMBj = [TMBj;sphrBj];
TMdBj = [TMdBj;dsphrBj];
TMHj = [TMHj;sphrHj];
TMdHj = [TMdHj;dsphrHj];
end
break;
end
nkj = ref_Idex*kj;
nkjr0 = nkj*r0;
sphrBiTM = besselj(AzMN(i)+0.5,nkjr0);
sphrBjTM = besselj(AzMN(i+1)+0.5,nkjr0);
sphrBkTM = besselj(AzMN(i+2)+0.5,nkjr0);
sphrHiTM = besselh(AzMN(i)+0.5,1,1i*nkjr0);
sphrHjTM = besselh(AzMN(i+1)+0.5,1,1i*nkjr0);
sphrHkTM = besselh(AzMN(i+2)+0.5,1,1i*nkjr0);
dsphrBjTM = (nkj.*(sphrBiTM-sphrBkTM)-sphrBjTM/r0)/2;
dsphrHjTM = (1i*nkj.*(sphrHiTM-sphrHkTM)-sphrHjTM/r0)/2;
BHdiffTM = log(ref_Idex*dsphrBjTM.*sphrHjTM)...
- log(dsphrHjTM.*sphrBjTM);
absBHdiffTM = abs(BHdiffTM);
end
if i>MNN-3
break;

```

```

end
% update function
sphrBi = sphrBj;
sphrBj = sphrBk;
sphrBk = besselj(AzMN(i+3)+0.5,nkr0);
sphrHi = sphrHj;
sphrHj = sphrHk;
sphrHk = besselh(AzMN(i+3)+0.5,1,1i*nkr0);
dsphrBj = (nk.*(sphrBi-sphrBk)-sphrBj/r0)/2;
dsphrHj = (1i*nk.*(sphrHi-sphrHk)-sphrHj/r0)/2;
end
dr = 0.001*r0;
rin = 0*r0:dr:r0;
rout = r0:dr:1.8*r0;
ll = 21;
nn = 10;
l = TEAzMN(ll);
TEk = optTEk(ll,nn);
% all element in optTEk are resonant k,
%many of them are overlap to each other though
RinTE = besselj(1+0.5,ref_Idex*TEk.*rin);
HoutTE = besselh(1+0.5,1,1i*ref_Idex*TEk.*rout);
RoutTE = RinTE(end)*abs(HoutTE)/abs(HoutTE(1));
%plot(rin,RinTE.^2); hold on; %plot(rout,RoutTE.^2);hold off;
TMk = optTMk(ll,nn);
% all element in optTMk are resonant k,
% many of them are overlap to each other though
RinTM = besselj(1+0.5,ref_Idex*TMk.*rin);
HoutTM = besselh(1+0.5,1,1i*ref_Idex*TMk.*rout);
RoutTM = RinTM(end)*abs(HoutTM)/abs(HoutTM(1));
%plot(rin,RinTM.^2);
%plot(rout,RoutTM.^2);hold off;
% legendre polynomials, matlab default 'legendre(l,X)' become NaN
% when l is too big
m1 = l;
m2 = l-1;
m3 = l-2;
theta = 0:0.001*pi:pi;
P = legendre(l,cos(theta),'norm');
Plm1 = P(m1+1,:); % +1 is because m=0 exist in the first row of P
Plm2 = P(m2+1,:);
Plm3 = P(m3+1,:);
plot(Plm1);
phi = -pi:0.001*pi:pi;
%%%%%%%%-plot-%%%%%%%%
figure(1)

```

```

plot(rin,RinTE.^2,'b','LineWidth',2); hold on;
plot(rout,RoutTE.^2,'r','LineWidth',2);hold off;
xlim([0.8*r0 1.05*r0]);
ylim([0,1.2*max(RinTE.^2)]);
set(gca,'xtick',[0 r0]);
set(gca,'xticklabels',[]);
set(gca,'ytick',[])
set(gca,'LineWidth',2);
grid on;
Xin = rin*sin(theta);
Xout = rout*sin(theta);
Zin = rin*cos(theta);
Zout = rout*cos(theta);
figure(2)
TEAin1xz = RinTE'*Plm1;
TEAout1xz = RoutTE'*Plm1;
maxA1xz = max(max(TEAin1xz));
sqTEAin1xz = (TEAin1xz/maxA1xz).^2;
sqTEAout1xz = (TEAout1xz/maxA1xz).^2;
plot3(r0*sin(theta),r0*cos(theta),theta<100,'w'); hold on;
Sin1xz = surf(Xin,Zin,sqTEAin1xz);
Sout1xz = surf(Xout,Zout,sqTEAout1xz); hold off;
set(Sin1xz,'EdgeColor','none');
set(Sout1xz,'EdgeColor','none');
ylim([-0.4*r0 0.4*r0]);
xlim([0.8*r0 1.04*r0]);
view(0,90);
daspect([1 1 1e5]);
set(gca,'xtick',[0 r0]);
set(gca,'xticklabels',[]);
set(gca,'ytick',[]);
figure(3)
TEAin2xz = RinTE'*Plm2;
TEAout2xz = RoutTE'*Plm2;
maxA2xz = max(max(TEAin2xz));
sqTEAin2xz = (TEAin2xz/maxA2xz).^2;
sqTEAout2xz = (TEAout2xz/maxA2xz).^2;
plot3(r0*sin(theta),r0*cos(theta),theta<100,'w'); hold on;
Sin2xz = surf(Xin,Zin,sqTEAin2xz);
Sout2xz = surf(Xout,Zout,sqTEAout2xz); hold off;
set(Sin2xz,'EdgeColor','none');
set(Sout2xz,'EdgeColor','none');
ylim([-0.4*r0 0.4*r0]);
xlim([0.8*r0 1.04*r0]);
view(0,90);
daspect([1 1 1e5]);

```

```

set(gca,'xtick',[0 r0]);
set(gca,'xticklabels',[]);
set(gca,'ytick',[]);
figure(4)
xin = rin'*cos(phi);
yin = rin'*sin(phi);
xout = rout'*cos(phi);
yout = rout'*sin(phi);
TEAin1xy = RinTE'*cos(m1*phi);
TEAout1xy = RoutTE'*cos(m1*phi);
maxA1xy = max(max(TEAin1xy));
sqTEAin1xy = (TEAin1xy/maxA1xy).^2;
sqTEAout1xy = (TEAout1xy/maxA1xy).^2;
plot3(r0*cos(phi),r0*sin(phi),phi<100,'w'); hold on;
Sin1xy = surf(xin,yin,sqTEAin1xy);
Sout1xy = surf(xout,yout,sqTEAout1xy); hold off;
set(Sin1xy,'EdgeColor','none');
set(Sout1xy,'EdgeColor','none');
xlim([-1.05*r0 1.05*r0]);
ylim([-1.05*r0 1.05*r0]);
view(0,90);
daspect([1 1 1e5]);
set(gca,'xtick',[]);
set(gca,'ytick',[]);

```

```

%%%%%%%%%%
%% filename = relocX.m %%
%%%%%%%%%%
function newX = relocX(X,base) % e.g. X = [0:10]; % 11 elements
% base = [0,0,1,1,0,0,1,1,1,0]; % 11 elements
% x(base>0) = [ 2,3, 7,8,9 ]
% newX = [ 1.5,2.0,2.5,3.0,3.5, 7.0,7.5,8.0,8.5,9.0,9.5 ]
%
% X must be equally spaced in each island: e.g. X = newX

```

```

n_sample = length(X);
Xgrid = min(diff(X));
XareaL = sum(base)*Xgrid;
newgrida = XareaL/(n_sample-1);
Xland = X(base>0);
dx = 0;
newX = [];
for i = 1:length(Xland)
Xstart = Xland(i)-0.5*Xgrid+dx;
Xend = Xland(i)+0.5*Xgrid;

```

```
x = [Xstart:newgrida:Xend];  
dx = newgrida-(Xend-x(end));  
newX = [newX,x];  
end  
if iscolumn(X)  
newX = newX';  
end  
end
```


Appendix B

Appendix B: MATLAB Code for Cavity Ring-Up Spectroscopy

```
%%%%%%%%%%
%% filename = CRUS. m %%
%%%%%%%%%%
function [t,Trans] = CRUS(tau,gamma_ex,detune,tr,maxt)
gamma = 2*pi/tau;
dt = tr/100;
t1 = [0:dt:tr]';
t2 = [0:dt:maxt*tr]';
A10 = 0;
ln2 = log(2);
%Runge Kutta A1 = zeros(size(t1));
A1(1) = A10;
for i = 1:length(t1)-1
k1 = -1i*detune*A1(i)-gamma/2*A1(i)...
    +sqrt(gamma_ex)*exp(-4*(t1(i)-tr)^2/(ln2*tr^2));
k2 = -1i*detune*(A1(i)+dt*k1/2)-gamma/2*(A1(i)+dt*k1/2)...
    +sqrt(gamma_ex)*exp(-4*(t1(i)+dt/2-tr)^2/(ln2*tr^2));
k3 = -1i*detune*(A1(i)+dt*k2/2)-gamma/2*(A1(i)+dt*k2/2)...
    +sqrt(gamma_ex)*exp(-4*(t1(i)+dt/2-tr)^2/(ln2*tr^2));
k4 = -1i*detune*(A1(i)+dt*k3)-gamma/2*(A1(i)+dt*k3)...
    +sqrt(gamma_ex)*exp(-4*(t1(i+1)-tr)^2/(ln2*tr^2));
A1(i+1) = A1(i)+dt*(k1+2*k2+2*k3+k4)/6;
end
A2 = zeros(size(t2));
A2(1) = A1(end);
for i = 1:length(t2)-1
k1 = -1i*detune*A2(i)-gamma/2*A2(i)+sqrt(gamma_ex);
k2 = -1i*detune*(A2(i)+dt*k1/2)-gamma/2*(A2(i)+dt*k1/2)+sqrt(gamma_ex);
k3 = -1i*detune*(A2(i)+dt*k2/2)-gamma/2*(A2(i)+dt*k2/2)+sqrt(gamma_ex);
k4 = -1i*detune*(A2(i)+dt*k3)-gamma/2*(A2(i)+dt*k3)+sqrt(gamma_ex);
A2(i+1) = A2(i)+dt*(k1+2*k2+2*k3+k4)/6;
```

```

end
S_in1 = exp(-4*(t1-tr).^2/(log(2)*tr^2));
S_in2 = t2==t2;
S_in = [S_in1;S_in2];
A = [A1;A2];
t = [t1;t2+t1(end)];
S_out = - S_in + sqrt(gamma_ex)*A;
Trans = abs(S_out).^2;
end

%%%%%%%%%%
%% Plots %%
%%%%%%%%%%
c = 3e+8;
wavelength = 1.55e-6;
tau = 250e-9;
gamma = 2*pi/tau;
tr = 1e-9;
figure(1)
maxt1 = 300;
gamma_ex = 0.5*gamma;
[ta1,Ta1] = CRUS(tau,gamma_ex,3*gamma,tr,maxt1);
[ta2,Ta2] = CRUS(tau,gamma_ex,6*gamma,tr,maxt1);
[ta3,Ta3] = CRUS(tau,gamma_ex,9*gamma,tr,maxt1);
plot(ta1/tr,Ta1,'k-','LineWidth',2);hold on;
plot(ta2/tr,Ta2,'r-','LineWidth',2);
plot(ta3/tr,Ta3,'b-.','LineWidth',2);
ylim([0.5 1.3]);
xlim([-10 maxt1]);
legend("","","Location','south');
legend('boxoff');
figure(2)
detuneratio = 2:25;
detune = detuneratio*gamma;
maxt2 = 100;
tr1 = 0.5e-9;
tr2 = 5e-9;
tr3 = 10e-9;
tb1 = [];
Tb1 = [];
tb2 = [];
Tb2 = [];
tb3 = [];
Tb3 = [];
peakHb1 = zeros(size(detune));

```

```

peakHb2 = zeros(size(detune));
peakHb3 = zeros(size(detune));
for i = 1:length(detune)
[t1,T1] = CRUS(tau,gamma_ex,detune(i),tr1,maxt2);
tb1 = [tb1,t1];
Tb1 = [Tb1,T1];
peakHb1(i) = max(T1);
[t2,T2] = CRUS(tau,gamma_ex,detune(i),tr2,maxt2);
tb2 = [tb2,t2];
Tb2 = [Tb2,T2];
peakHb2(i) = max(T2);
[t3,T3] = CRUS(tau,gamma_ex,detune(i),tr3,maxt2);
tb3 = [tb3,t3];
Tb3 = [Tb3,T3];
peakHb3(i) = max(T3);
end
plot(detune/gamma,peakHb1,'k-','LineWidth',2);hold on;
plot(detune/gamma,peakHb2,'r-','LineWidth',2);
plot(detune/gamma,peakHb3,'b-.','LineWidth',2);hold off;
xlim([5 25]);
legend('','','Location','north');
legend('boxoff');
figure(3)
maxt3 = 200;
gammaratio = 0.1:0.1:0.9;
gamma_ex = gammaratio*gamma;
tc1 = [];
Tc1 = [];
tc2 = [];
Tc2 = [];
tc3 = [];
Tc3 = [];
peakHc1 = zeros(size(gamma_ex));
peakHc2 = zeros(size(gamma_ex));
peakHc3 = zeros(size(gamma_ex));
for i = 1:length(gamma_ex)
[t1,T1] = CRUS(tau,gamma_ex(i),5*gamma,tr,maxt3);
tc1 = [tc1,t1];
Tc1 = [Tc1,T1];
peakHc1(i) = max(T1);
[t2,T2] = CRUS(tau,gamma_ex(i),10*gamma,tr,maxt3);
tc2 = [tc2,t2];
Tc2 = [Tc2,T2];
peakHc2(i) = max(T2);
[t3,T3] = CRUS(tau,gamma_ex(i),15*gamma,tr,maxt3);
tc3 = [tc3,t3];

```

```

Tc3 = [Tc3,T3];
peakHc3(i) = max(T3);
end
plot(gamma_ex/gamma,peakHc1,'k-','LineWidth',2);hold on;
plot(gamma_ex/gamma,peakHc2,'r-','LineWidth',2);
plot(gamma_ex/gamma,peakHc3,'b-','LineWidth',2);hold off;
xlim([0 1]);
ylim([1 1.3]);
legend("'",',','Location','northwest');
legend('boxoff');
figure(4)
taul = 10e-9;
maxt5 = 50;
gamma5 = 2*pi/taul;
Qfactor = 2*pi*c/wavelength./gamma5;
gamma_ex5 = 0.5*gamma5;
detune5 = [0.1,0.6,2]*gamma5;
[te1,Te1] = CRUS(taul,gamma_ex5,detune5(1),tr,maxt5);
[te2,Te2] = CRUS(taul,gamma_ex5,detune5(2),tr,maxt5);
[te3,Te3] = CRUS(taul,gamma_ex5,detune5(3),tr,maxt5);
plot(te1/tr,Te1,'k-','LineWidth',2);hold on;
plot(te2/tr,Te2,'r-','LineWidth',2);
plot(te3/tr,Te3,'b-','LineWidth',2);
figure(5)
taul = 3e-9;
maxt5 = 15;
gamma5 = 2*pi/taul;
Qfactor = 2*pi*c/wavelength2./gamma5;
gamma_ex5 = 0.5*gamma5;
detune5 = [0.1,0.5,2]*gamma5;
[te1,Te1] = CRUS(taul,gamma_ex5,detune5(1),tr,maxt5);
[te2,Te2] = CRUS(taul,gamma_ex5,detune5(2),tr,maxt5);
[te3,Te3] = CRUS(taul,gamma_ex5,detune5(3),tr,maxt5);
plot(te1/tr,Te1,'k-','LineWidth',2);hold on;
plot(te2/tr,Te2,'r-','LineWidth',2);
plot(te3/tr,Te3,'b-','LineWidth',2);
xlim([-5 maxt6]);
legend('Δω = 0.1γ','Δω = 0.6γ','Δω = 2γ,...','Location','southeast');
figure(6)
taul = 3e-9;
maxt6 = 15;
gamma6 = 2*pi/taul;
Qfactor = 2*pi*c/wavelength2./gamma6;
gamma_ex6 = [0.2, 0.5, 0.8]*gamma6;
detune6 = 0.5*gamma6;
[tf1,Tf1] = CRUS(taul,gamma_ex6(1),detune6,tr,maxt6);

```

```

[tf2,Tf2] = CRUS(taul,gamma_ex6(2),detune6,tr,maxt6);
[tf3,Tf3] = CRUS(taul,gamma_ex6(3),detune6,tr,maxt6);
plot(tf1/tr,Tf1,'k-','LineWidth',2);hold on;
plot(tf2/tr,Tf2,'r-','LineWidth',2);
plot(tf3/tr,Tf3,'b-','LineWidth',2);
xlim([-5 maxt6]);
legend('γex = 0.2γ', 'γex = 0.5γ', 'γex = 0.8γ', ...'Location','southeast');
figure(7)
detuneratio = 5:0.5:25;
detune = detuneratio*gamma;
gamma_ex = 0.5*gamma;
maxt7 = 200;
AnalTg = [];
tg = [];
Tg = [];
peakHgN = zeros(size(detune));
peakHgA = zeros(size(detune));
for i = 1:length(detune)
[t,T] = CRUS(tau,gamma_ex,detune(i),tr,maxt7);
tg = [tg;t'];
Tg = [Tg;T'];
peakHgN(i) = max(T);
Omegag = 1i*detune(i)+gamma/2;
Ig = 1 - Omegag*sqrt(pi/beta)+Omegag^2/(2*beta);
AnalSout = -1 + gamma_ex*(1-Ig*exp(-Omegag*(t)))/Omegag;
ATg = abs(AnalSout).^2;
AnalTg = [AnalTg;ATg'];
peakHgA(i) = max(ATg);
end
plot(detune/gamma,peakHgN,'k-','LineWidth',2);hold on;
plot(detune/gamma,peakHgA,'r-','LineWidth',2);hold off;
legend('','Location','north');
legend('boxoff');
figure(8)
detune8 = 10*gamma;
gamma_ex = [0.1:0.1:0.9]*gamma;
maxt8 = 100;
AnalTh = [];
th = [];
Th = [];
peakHhN = zeros(size(detune8));
peakHhA = zeros(size(detune8));
for i = 1:length(gamma_ex)
[t,T] = CRUS(tau,gamma_ex(i),detune8,tr,maxt8);
th = [th,t];
Th = [Th,T];

```

```

peakHhN(i) = max(T);
Omegag = li*detune8+gamma/2;
Ig = 1 - Omegag*sqrt(pi/beta)+Omegag^2/(2*beta);
AnalSout = -1 + gamma_ex(i)*(1-Ig*exp(-Omegag*(t)))/Omegag;
ATh = abs(AnalSout).^2;
AnalTh = [AnalTh;ATh];
peakHhA(i) = max(ATh);
end
plot(gamma_ex/gamma,peakHhN,'k-','LineWidth',2);hold on;
plot(gamma_ex/gamma,peakHhA,'r-','LineWidth',2);hold off;
xlim([0,1]);
legend("",'', 'Location', 'northwest');
legend('boxoff');
figure(9)
detune9 = [5:0.5:20]*gamma;
gamma_ex9 = [0.1:0.05:0.9]*gamma;
maxt8 = 100;
[D9,G9] = meshgrid(detune9,gamma_ex9);
peakHh9 = zeros(size(D9));
for i = 1:length(gamma_ex9)
for j = 1:length(detune9)
[t,T] = CRUS(tau,gamma_ex9(i),detune9(j),tr,maxt8);
peakHh9(i,j) = max(T);
end
end
surf9 = surf(D9/gamma,G9/gamma,peakHh9);
set(surf9,'EdgeColor','interp');
colorbar;
ylim([0.1 0.9]);

```

Appendix C

Appendix C: MATLAB code for Raman Switching Model

```
% ===== Define constant =====
clear all
c = 3e8;
speed_factor = 19;
lambda1 = 768.1*1e-9;
lambda2 = 795.9*1e-9;
lambda3 = 799.4*1e-9;
w10 = 2*pi*c/lambda1;
wp=w10;
wR1 = 2*pi*c/lambda2;
wR2 = 2*pi*c/lambda3;
R = 41.5e-6;
neff = 1.3;
Vp=pi*(1e-6)^2*2*pi*30e-6;
f=0.8;
df12 = (wR1-w10)/(2*pi)*1e-12;
df13 = (wR2-w10)/(2*pi)*1e-12;
df23 = df13 - df12;
g_R=RamanGain([df12 df13 df23]);
g=f*c^2*g_R/2/neff^2/Vp;
g12=g(1);
g13=g(2);
g23=g(3);
% ===== Initialization =====
gamma_1 = 2.494*1e7;
gamma_ex1 = 2.237*1e7;
gamma_in = gamma_1-gamma_ex1;
gamma_2 = gamma_1;
gamma_ex2 = gamma_ex1;
gamma_in2 = gamma_2-gamma_ex2;
gamma_3 = (g13*gamma_1+56*g12*g23*1e-6/gamma_ex2)/g12;
```

```

gamma_ex3 = (46*g13*wR1*gamma_ex2)/(112*g12*wR2);
gamma_in3 = gamma_3-gamma_ex3;
tc = 2*pi*neff*R/c;
yeta = sqrt(2*tc*gamma_ex1);
sqrttc = sqrt(tc);
w0_initial = 2*gamma_1;
Pin = 500e-6;
Ein = sqrt(Pin);
Vs = -85*6*10^6; experiment
Cp = 1e-7;
s=1e-4;
a=6e-6;
b=800*Cp*ones(3,1);
gamma_th=7e4*Cp;
theta=w10*5e-6;
Trange = 1400000e-6;
tstep0 = Trange*10^-8/3;
t = [0:tstep0:Trange];
Nstep = length(t);
tstep = diff(t);
y0 = [0.1;0;0;0;w10+w0_initial];
Ein0 = ones(length(tstep),1)*Ein;
Q1 = c*2*pi/((2.5*10^6+2.24*10^7)*780*10^-9);
index = 1:speed_factor:(Nstep+speed_factor);
G12in = g12*tc;
G13in = g13*tc;
G23in = g23;
G12out = wp/wR1*g12;
G13out = wp/wR2*g13;
G23out = wR1/wR2*g23;
Ain1 = -1i*yeta/tc*Ein;
Nin2 = -1i*yeta/tc;
Nin3 = -1i*yeta/tc;
j = 1; y=y0; Y=[]; dYdt=[]; time=[]; t_initial=cputime; T1 = []; T2=[];
for it = 1:length(tstep)
E_raman2=(rand()-0.5)*Ein*1e-10;
E_raman3=(rand()-0.5)*Ein*1e-10; if it<length(tstep)*ScanStop
Ain = [Ain1,Nin2*E_raman2,Nin3*E_raman3];
k1 = RamanSwitch4(t,y,gamma_1,gamma_2,gamma_3,...
Vs,Ain,w10,G12in,G13in,G23in,G12out,G13out,G23out);
k2 = RamanSwitch4(0,y+tstep(it)*k1/2,gamma_1,gamma_2,gamma_3,...
Vs,Ain,w10,G12in,G13in,G23in,G12out,G13out,G23out);
k3 = RamanSwitch4(0,y+tstep(it)*k2/2,gamma_1,gamma_2,gamma_3,...
Vs,Ain,w10,G12in,G13in,G23in,G12out,G13out,G23out);
k4 = RamanSwitch4(0,y+tstep(it)*k3,gamma_1,gamma_2,gamma_3,...
Vs,Ain,w10,G12in,G13in,G23in,G12out,G13out,G23out);

```

```

dy = (k1+2*k2+2*k3+k4)/6;
y = y + timestep(it)*dy;
if sum(isnan(y))== 3
break;
end
if it == 100*index(j)
Y(:,j) = y;
dYdt(:,j) = dy;
time(j) = t(it)*1e6;
Ein_t(j) = Ein0(it);
Tem(j) = y(4);
detuning(j)= y(5)-(w10-theta*y(4));
j = j+1;
end
if mod(it,100000)==0
sim_percentage = 100*it/Nstep
end
end
Transmission = abs((Ein_t(1:length(Y(1,:)))-li*yeta*Y(1,:))./max(Ein_t)).^2;
Transmission2 = abs(yeta*Y(2,:))./max(Ein_t).^2;
power1=gamma_ex2*abs(Y(2,:).^2);
power2=gamma_ex3*abs(Y(3,:).^2);
plotRange = [1:length(time)];
Xl = detuning(plotRange)/(2*pi);
Xr = detuning(plotRange)/(2*pi);
Yl1 = power1(plotRange)*1e6;
Yl2 = power2(plotRange)*1e6;
Yr = Transmission(plotRange);
[hAx,pP1,Trns] = plotyy(Xl,Yl1,Xr,Yr);hold on;
pP2 = plot(Xl,Yl2);
hold off;
set(pP1,'LineWidth',2,'Color','r');
set(pP2,'LineWidth',2,'Color',[0,0.5,1]);
set(Trns,'LineWidth',2,'Color',[1,0.5,0]);
ylabel(hAx(1),'');
ylabel(hAx(2),'');
xlabel('');
ylim(hAx(1),[0 140]);
ylim(hAx(2),[0.2999999 1]);
set(gca,'linewidth',2)
hAx(1).YColor = [0,0,0];
hAx(1).YTick = [0:40:140];
hAx(1).LineWidth = 2;
hAx(2).YColor = [0,0,0];
hAx(2).YTick = [0.3:0.2:1];
hAx(2).LineWidth = 2;

```

```

legend('\gamma_{ex,1}P_1', '\gamma_{ex,2}P_2', 'T', 'Location', 'west')
legend('boxoff')
grid on;

%%%%%%%%%%%%%%%%%%%%%%%%%%%%%%%%%%%%%%%%%%%%%%%%%%%%%%%%%%%%%%%%%%%%%%%%
%% filename = RamanGain. m %%
%%%%%%%%%%%%%%%%%%%%%%%%%%%%%%%%%%%%%%%%%%%%%%%%%%%%%%%%%%%%%%%%%%%%%%%%
function S = RamanGain(df)
c = 3*10^8;
domega = 2*pi*df*10^12;
if iscolumn(df)
domega = domega';
end
L = length(domega);
CompPos = [56.25;100;231.25;362.5;463;497;...
           611.5;691.67;793.67;835.5;930;1080;1215]*10^2;
omega_vi = 2*pi*c*CompPos;
Ai = [1;11.4;36.67;67.67;74;4.5;6.8;4.6;4.2;4.5;2.7;3.1;3];
GFWHM = [52.1;110.42;175;162.5;135.33;24.5;41.5;155;59.5;64.3;150;91;160]*10^2;
Gamma = pi*c*GFWHM;
sqGamma = Gamma.^2;
LFWHM = [17.37;38.81;58.33;54.17;45.11;8.17;...
         13.83;51.67;19.83;21.43;50;30.33;53.33]*10^2;
gamma = pi*c*LFWHM;
S_dOmega = zeros(13,L);
for i = 1:13
omega_p = omega_vi(i) + domega;
omega_m = omega_vi(i) - domega;
dt = 1/(10*max(omega_p));
tmax = 10/Gamma(i);
t = [0:dt:tmax]';
ts = ones(size(t));
T = repmat(t,size(domega));
Omega_p = ts*omega_p;
Omega_m = ts*omega_m;
S_dOmegaT = (cos(Omega_m.*T)-cos(Omega_p.*T))...
            .*exp(-sqGamma(i)*T.^2/4-gamma(i)*T);
S_dOmegaTD = [zeros(1,L);S_dOmegaT];
S_dOmegaTU = [S_dOmegaT;zeros(1,L)];
S_dOmega(i,:) = ts(1:end-1)'*(S_dOmegaTU(2:end-1,:))...
              +S_dOmegaTD(2:end-1,:))*dt/2;
end
s_omega = Ai*S_dOmega/2;
if iscolumn(df)
s_omega = s_omega';

```

```

end
maxs = max(s_omega);
S = s_omega/maxs*10^-13;
end

%%%%%%%%%%
%% filename = RamanSwitch4. m %%
%%%%%%%%%%
function dy = RamanSwitch4(t,y,gamma_1,gamma_2,gamma_3,...
    Vs,Ain,w10,G12in,G13in,G23in,G12out,G13out,G23out)
dy = zeros(5,1);
sqy = abs(y(1:3)).^2;
dy(1) = -(gamma_1 - 1i*(y(5)-w10)).*y(1)...
    -G12out*sqy(2).*y(1)-G13out*sqy(3).*y(1)+Ain(1);
dy(2) = -gamma_2*y(2) + G12in*sqy(1).*y(2)-G23out*sqy(3).*y(2)+Ain(2);
dy(3) = -gamma_3*y(3) + G13in*sqy(1).*y(3)+G23in*sqy(2).*y(3)+Ain(3);
dy(4) = 0;
dy(5) = Vs;

```


Bibliography

- [1] T. H. Maiman, *Nature* **187**, 493 (1960).
- [2] L. Rayleigh, *The London, Edinburgh, and Dublin Philosophical Magazine and Journal of Science* **20**, 1001–1004 (1910).
- [3] G. Rempe, R. J. Thompson, H. J. Kimble, and R. Lalezari, *Opt. Lett.* **17**, 363–365 (1992).
- [4] K. Srinivasan, P. Barclay, O. Painter, J. Chen, C. Cho, and C. Gmachl, *Appl. Phys. Lett.* **83**, 1915 (2003).
- [5] W. Bogaerts, P. D. Heyn, T. V. Vaerenbergh, K. D. Vos, S. K. Selvaraja, T. Claes, P. Dumon, P. Bienstman, D. V. Thourhout, and R. Baets, *Laser Photonics Rev.* **6**, 47–73 (2012).
- [6] M. L. Gorodetsky, A. A. Savchenkov, and V. S. Ilchenko, *Opt. Lett.* **21**, 453–455 (1996).
- [7] K. J. Vahala, *Nature* **424**, 839–846 (2003).
- [8] D. K. Armani, T. J. Kippenberg, S. M. Spillane, and K. J. Vahala, *Nature* **421**, 925–928 (2003).
- [9] B. Peng, S. K. Özdemir, F. Lei, F. Monifi, M. Gianfreda, G. L. Long, S. Fan, F. Nori, C. M. Bender, and L. Yang, *Nat. Phys.* **10**, 394–398 (2014).
- [10] M. Sumetsky, Y. Dulashko, and R. S. Windeler, *Opt. Lett.* **35**, 898–900 (2010).
- [11] A. Watkins, J. M. Ward, Y. Wu, and S. Nic Chormaic, *Opt. Lett.* **36**, 2113–5 (2011).
- [12] J. M. Ward, Y. Yang, and S. Nic Chormaic, *IEEE Photonics Technol. Lett.* **25**, 2350–2353 (2013).
- [13] Y. Yang, S. Saurabh, J. M. Ward, and S. Nic Chormaic, *Opt. Express* **24**, 294–299 (2016).
- [14] Y. Yang, S. K. F. Lei, L. Xu, J. Ward, L. Yang, and S. Nic Chormaic, *Opt. Express* **25**, 1308–1313 (2017).
- [15] M. Sumetsky, *Opt. Lett.* **29**, 893–895 (2004).

-
- [16] J. M. Ward, Y. Yang, and S. Nic Chormaic, *Sci. Rep.* **6**, 25152 (2016).
- [17] M. Asano, Y. Takeuchi, W. Chen, S. K. Ozdemir, R. Ikuta, N. Imoto, L. Yang, and T. Yamamoto, *Laser Photonics Rev.* **10**, 603–611 (2016).
- [18] Y. Yang, Y. Ooka, R. Thompson, J. Ward, and S. Nic Chormaic, *Opt. Lett.* **41**, 575 (2016).
- [19] P. Bianucci, *Sensors* **16**, 1841 (2016).
- [20] D. W. Vernooy, V. S. Ilchenko, H. Mabuchi, E. W. Streed, and H. J. Kimble, *Opt. Lett.* **23**, 247–249 (1998).
- [21] A. E. Shitikov, I. A. Bilenko, N. M. Kondratiev, V. E. Lobanov, A. Markosyan, and M. L. Gorodetsky, *Optica* **5**, 1525–1528 (2018).
- [22] T. J. Kippenberg, S. M. Spillane, and K. J. Vahala, *Appl. Phys. Lett.* **85**, 6113 (2004).
- [23] V. S. Ilchenko, M. L. Gorodetsky, X. S. Yao, and L. Maleki, *Opt. Lett.* **26**, 256–258 (2001).
- [24] Y. Yang, J. Ward, and S. Nic Chormaic, *Opt. Express* **22**, 6881–6898 (2014).
- [25] R. Symes, R. M. Sayera, and J. P. Reid, *Phys. Chem. Chem. Phys.* **6**, 474–487 (2004).
- [26] S. K. Y. Tang, R. Derda, Q. Quan, M. Loncar, and G. M. Whitesides, *Opt. Express* **19**, 2204–2215 (2011).
- [27] H. B. Lin and A. J. Campillo, *Phys. Rev. Lett.* **73**, 2440–2443 (1994).
- [28] S.-X. Qian and R. K. Chang, *Phys. Rev. Lett.* **56**, 926–929 (1986).
- [29] J. B. Snow, S.-X. Qian, and R. K. Chang, *Opt. Lett.* **10**, 37–39 (1985).
- [30] H. Lin, L. Li, Y. Zou, S. Danto, J. D. Musgraves, K. Richardson, S. Kozacik, M. Murakowski, D. Prather, P. T. Lin, V. Singh, A. Agarwal, L. C. Kimerling, and J. Hu, *Opt. Lett.* **38**, 1470–1472 (2013).
- [31] V. S. Ilchenko, A. A. Savchenkov, A. B. Matsko, and L. Maleki, *Phys. Rev. Lett.* **92**, 043903 (2004).
- [32] J. U. Furst, D. V. Strekalov, D. Elser, A. Aiello, U. L. Andersen, C. Marquardt, and G. Leuchs, *Phys. Rev. Lett.* **106**, 113901 (2011).
- [33] M. Fortsch, J. U. Furst, C. Wittmann, D. Strekalov, A. Aiello, M. V. Chekhova, C. Silberhorn, G. Leuchs, and C. Marquardt, *Nat. Commun.* **4**, 1818 (2013).
- [34] M. Fortsch, G. Schunk, J. U. Furst, D. Strekalov, T. Gerrits, M. J. Stevens, F. Sedlmeir, H. G. L. Schwefel, S. W. Nam, and G. L. C. Marquardt, *Phys. Rev. A* **91**, 023812 (2015).

-
- [35] A. A. Savchenkov, V. S. Ilchenko, A. B. Matsko, and L. Maleki, *Phys. Rev. A* **70**, 051804 (2004).
- [36] V. S. Ilchenko, A. B. Matsko, A. A. Savchenkov, and L. Maleki, *J. Opt. Soc. Am.* **20**, 1304–1308 (2003).
- [37] D. Farnesi, A. Barucci, G. Righini, S. Berneschi, S. Soria, and G. N. Conti, *Phys. Rev. Lett.* **112**, 093901 (2014).
- [38] Y. Wu, J. M. Ward, and S. Nic Chormaic, *J. Appl. Phys.* **107**, 033103 (2014).
- [39] F. Vollmer, S. Arnold, and D. Keng, *Proc. Natl. Acad. Sci. U.S.A.* **105**, 20701–20704 (2008).
- [40] F. Vollmer and L. Yang, *Nanoscale* **1**, 267–291 (2012).
- [41] J. M. Ward, N. Dhasmana, and S. Nic Chormaic, *Eur. Phys. J. Spec. Top.* **223**, 1917–1935 (2014).
- [42] W. Lee, Q. Chen, X. Fan, and D. K. Yoon, *Lab Chip* **16**, 4770 (2016).
- [43] W. Yoshiki and T. Tanabe, *Opt. Express* **22**, 24332 (2014).
- [44] P. Wang, R. Madugani, H. Zhao, W. Yang, J. M. Ward, Y. Yang, G. Farrell, G. Brambilla, and S. Nic Chormaic, *IEEE Photonics Technol. Lett.* **28**, 2277 (2016).
- [45] T. J. Kippenberg and K. J. Vahala, *Science* **321**, 1172 (2008).
- [46] M. Aspelmeyer, T. J. Kippenberg, and F. Marquardt, *Rev. Mod. Phys.* **86**, 1391–1452 (2014).
- [47] Y. Li, J. Millen, and P. F. Barker, *Opt. Express* **24**, 1392 (2016).
- [48] F. Monifi, J. Zhang, S. K. Ozdemir, B. Peng, Y. Liu, F. Bo, F. Nori, and L. Yang, *Nat. Photonics* **10**, 399 (2016).
- [49] Y. Chen, *J. Phys. B: At. Mol. Opt. Phys.* **46**, 104001 (2013).
- [50] S. Kasumie, Y. Yang, J. M. Ward, and S. Nic Chormaic, *Rev. Las. Engin.* **46**, 92 (2018).
- [51] A. D. Kersey, *Opt. Fiber Technol.* **2**, 291–317 (1996).
- [52] N. M. Hanumegowda, C. J. Stica, B. C. Patel, I. White, and X. Fan, *Appl. Phys. Lett.* **87**, 201107 (2005).
- [53] Y. Hu, L. Shao, S. Arnold, Y.-C. Liu, C.-Y. Ma, and Y.-F. Xiao, *Phys. Rev. A* **90**, 043847 (2014).
- [54] L. He, S. K. Ozdemir, J. Zhu, W. Kim, and L. Yang, *Nat. Nanotechnol.* **6**, 428–432 (2011).

- [55] F. Vollmer, D. Braun, and A. Libchaber, *Appl. Phys. Lett.* **80**, 4057 (2002).
- [56] B.-B. Li, W. R. Clements, X.-C. Yu, K. Shi, Q. Gong, and Y.-F. Xiao, *Proc. Natl. Acad. Sci. U.S.A.* **111**, 14657–14662 (2014).
- [57] S. K. Özdemir, J. Zhu, X. Yang, B. Peng, H. Yilmaz, L. He, F. Monifi, S. H. Huang, G. L. Long, and L. Yang, *Proc. Natl. Acad. Sci. U.S.A.* **111**, E3836–E3844 (2014).
- [58] M. R. Foreman, J. D. Swaim, and F. Vollmer, *Adv. Opt. Photonics* **7**, 168 (2015).
- [59] R. M. Hawk, M. V. Chistiakova, and A. M. Armani, *Opt. Lett.* **38**, 20–28 (4690–4693).
- [60] H. Ghali, H. Chibli, J. L. Nadeau, P. Bianucci, and Y.-A. Peter, *Biosensors* **6**, 20 (2016).
- [61] I. M. White, H. Oveys, and X. Fan, *Opt. Lett.* **31**, 1319 (2006).
- [62] C.-H. Dong, L. He, Y.-F. Xiao, V. R. Gaddam, S. K. Ozdemir, Z.-F. Han, G.-C. Guo, and L. Yang, *Appl. Phys. Lett.* **94**, 231119 (2009).
- [63] Y.-Z. Yan, C.-L. Zou, S.-B. Yan, F.-W. Sun, Z. Ji, J. Liu, Y.-G. Zhang, L. Wang, C.-Y. Xue, W.-D. Zhang, Z.-F. Han, and J.-J. Xiong, *Opt. Express* **19**, 5753–5759 (2011).
- [64] R. Henze, T. Seifert, J. M. Ward, and O. Benson, *Opt. Lett.* **36**, 4536–8 (2011).
- [65] Y. Yang, S. Saurabh, J. M. Ward, and S. Nic Chormaic, *Opt. Express* **24**, 294 (2016).
- [66] M. Sumetsky, Y. Dulashko, and R. S. Windeler, *Opt. Lett.* **35**, 1866–1868 (2010).
- [67] R. Madugani, Y. Yang, J. M. Ward, J. D. Riordan, S. Coppola, V. Vespini, S. Grilli, S. Finizio, P. Ferraro, and S. Nic Chormaic, *Opt. Lett.* **37**, 4762 (2012).
- [68] L. Stern, I. Goykhman, B. Desiatov, and U. Levy, *Opt. Lett.* **37**, 1313–1315 (2012).
- [69] S. Rosenblum, Y. Lovsky, L. Arazi, F. Vollmer, and B. Dayan, *Nat. Commun.* **6**, 6788 (2015).
- [70] F.-J. Shu, C.-L. Zou, S. K. Özdemir, L. Yang, and G.-C. Guo, *Opt. Express* **23**, 30067–30078 (2015).
- [71] C. Dong, C. Zou, J. Cui, Y. Yang, Z. Han, and G. Guo, *Chin. Opt. Lett.* **7**, 299–301 (2009).
- [72] A. Rasoloniaina, V. Huet, T. K. N. Nguyên, E. Le Cren, M. Mortier, L. Michely, Y. Dumeige, and P. Féron, *Sci. Rep.* **4**, 4023 (2014).
- [73] T. Carmon, L. Yang, and K. J. Vahala, *Opt. Express* **12**, 4742 (2004).

-
- [74] A. Krushelnitsky and D. Reichert, *Prog. Nucl. Magn. Reson. Spectrosc.*, **1** (2005).
- [75] S. Khodadadi, J. E. Curtis, and A. P. Sokolov, *J. Phys. Chem. B* **115**, 6222 (2011).
- [76] M.-Y. Ye, M.-X. Shen, and X.-M. Lin, *Sci. Rep.* **6**, 19597 (2016).
- [77] Y. Yang, R. Madugani, S. Kasumie, J. Ward, and S. Nic Chormaic, *Appl. Phys. B* **122**, 291 (2016).
- [78] P. T. Rakich, M. A. Popovic, M. Soljacic, and E. P. Ippen, *Nat. Photonics* **1**, 658–665 (2007).
- [79] F. Riboli, A. Recati, M. Antezza, and I. Carusotto, *Eur. Phys. J. D* **1**, 157–164 (2008).
- [80] A. Mizrahi and L. Schachter, *Opt. Lett.* **32**, 692–694 (2007).
- [81] K. Hayata, H. Yénaka, and M. Koshiba, *Opt. Lett.* **18**, 1385–1387 (1993).
- [82] H. Miyazaki and Y. Jimba, *Phys. Rev. B* **62**, 7976–7997 (2000).
- [83] B. Peng, S. K. Ozdemir, W. Chen, F. Nori, and L. Yang, *Nat. Commun.* **5**, 5082 (2014).
- [84] M. L. Povinelli, S. G. Johnson, M. Loncar, M. Ibanescu, E. J. Smythe, F. Capasso, and J. D. Joannopoulos, *Opt. Express* **13**, 8286–8295 (2005).
- [85] J. M. Ward, Y. Wu, V. G. Minogin, and S. Nic Chormaic, *Phys. Rev. A* **79**, 053839 (2009).
- [86] R. Madugani, Y. Yang, J. M. Ward, V. H. Le, and S. Nic Chormaic, *Appl. Phys. Lett.* **106**, 241101 (2015).
- [87] A. L. Schawlow and C. H. Townes, *Phys. Rev.* **112**, 1940–1949 (1958).
- [88] L. Yang, T. Lu, T. Carmon, B. Min, and K. J. Vahala. *A 4-Hz Fundamental Linewidth on-chip Microlaser*. In *2007 Conference on Lasers and Electro-Optics (CLEO)*, pages 1–2, (2007).
- [89] V. Sandoghdar, F. Treussart, J. Hare, V. Lefèvre-Seguin, J.-M. Raimond, and S. Haroche, *Phys. Rev. A* **54**, R1777–R1780 (1996).
- [90] Z. P. Cai, H. Y. Xu, G. M. Stéphan, P. Féron, and M. Mortier, *Opt. Commun.* **229**, 311–315 (2004).
- [91] J. M. Ward and S. Nic Chormaic, *Appl. Phys. B* **100**, 847 (2010).
- [92] L. He, S. K. Özdemir, and L. Yang, *Laser Photonics Rev.* **7**, 60–82 (2013).
- [93] L. Yang and K. J. Vahala, *Opt. Lett.* **28**, 592 (2003).

-
- [94] M. Ferrari, A. Chiasera, E. Moser, Y. Jestin, C. G. Nunzi, S. Berneschi, G. C. Righini, S. Soria, M. Brenci, F. Cosi, C. Armellini, A. Chiappini, L. Ghisa, S. Trebaol, Y. Dumeige, S. Pelli, and P. Féron, *Adv. Sci. Technol.* **55**, 46–55 (2009).
- [95] L. Yang, T. Carmon, B. Min, S. M. Spillane, and K. J. Vahala, *Appl. Phys. Lett.* **86**, 091114 (2005).
- [96] F. Lei, B. Peng, S. K. Özdemir, G. L. Long, and L. Yang, *Appl. Phys. Lett.* **105**, 101112 (2014).
- [97] X. F. Jiang, C.-L. Zou, L. Wang, Q. Gong, and Y.-F. Xiao, *Laser Photonics Rev.* **10**, 40–61 (2016).
- [98] B. Li, Y. Xiao, M. Yan, W. R. Clements, and Q. Gong, *Opt. Lett.* **38**, 1802 (2013).
- [99] G. Bahl, K. H. Kim, W. Lee, J. J. Liu, X. Fan, and T. Carmon, *Nat. Commun.* **4**, 1994 (2013).
- [100] W. Lee, Y. Sun, H. Li, K. Reddy, M. Sumetsky, and X. Fan, *Appl. Phys. Lett.* **99**, 091102 (2011).
- [101] Y.-C. Chen, Q. Chen, and X. Fan, *Optica* **3**, 809–815 (2016).
- [102] X. Fan and S.-H. Yun, *Nat. Methods* **11**, 141–147 (2014).
- [103] S. K. Ozdemir, J. Zhua, X. Yangb, B. Penga, H. Yilmaza, L. Hea, F. Monifia, S. H. Huanga, G. L. Longb, and L. Yang, *Proc. Natl. Acad. Sci. U. S. A.* **111**, E3836 (2014).
- [104] R. W. Boyd, *Nonlinear Optics*, Elsevier (2003).
- [105] A. Andronico, I. Favero, and G. Leo, *Opt. Lett.* **33**, 2026–2028 (2008).
- [106] D. V. Strekalov, A. S. Kowligy, Y.-P. Huang, and P. Kumar, *New J. Phys.* **16**, 053025 (2014).
- [107] I. Breunig, *Las. Photo. Rev.* **10**, 569–587 (2016).
- [108] T. Udem, R. Holzwarth, and T. W. Hänsch, *Nature* **416**, 233–237 (2002).
- [109] T. J. Kippenberg, R. Holzwarth, and S. A. Diddams, *Science* **332**, 555–559 (2011).
- [110] A. F. Fercher, W. Drexler, C. K. Hitzenberger, and T. Lasser, *Rep. Prog. Phys.* **66**, 239–303 (2003).
- [111] S. T. Cundiff and J. Ye, *Rev. Mod. Phys.* **75**, 325 (2003).
- [112] U. Keller, *Nature* **424**, 831–838 (2003).

-
- [113] I. H. Agha, Y. Okawachi, and A. L. Gaeta, *Opt. Express* **17**, 16209 (2009).
- [114] P. Del’Haye, A. Schliesser, O. Arcizet, T. Wilken, R. Holzwarth, and T. J. Kippenberg, *Nature* **450**, 1214–1217 (2007).
- [115] P. Del’Haye, T. Herr, E. Gavartin, M. L. Gorodetsky, R. Holzwarth, and T. J. Kippenberg, *Phys. Rev. Lett.* **107**, 063901 (2011).
- [116] Y. Okawachi, K. Saha, J. S. Levy, Y. H. Wen, M. Lipson, and A. L. Gaeta, *Opt. Lett.* **36**, 3398–3400 (2011).
- [117] A. A. Savchenkov, A. B. Matsko, V. S. Ilchenko, I. Solomatine, D. Seidel, and L. Maleki, *Phys. Rev. Lett.* **101**, 093902 (2008).
- [118] I. S. Grudinin, N. Yu, and L. Maleki, *Opt. Lett.* **34**, 878–880 (2009).
- [119] M. Li, X. Wu, L. Liu, and L. Xu, *Opt. Express* **21**, 16908–13 (2013).
- [120] Y. Yang, Y. Ooka, R. M. Thompson, J. M. Ward, and S. Nic Chormaic, *Opt. Lett.* **41**, 575–578 (2016).
- [121] Q. Lu, S. Liu, X. Wu, L. Liu, and L. Xu, *Opt. Lett.* **41**, 1736–1739 (2016).
- [122] I. H. Agha, Y. Okawachi, M. A. Foster, J. E. Sharping, and A. L. Gaeta, *Phys. Rev. A* **76**, 043837 (2007).
- [123] G. Lin and Y. K. Chembo, *Opt. Express* **23**, 1594–1604 (2015).
- [124] N. Riesen, S. A. V., A. François, and T. M. Monro, *Opt. Express* **23**, 14784–14795 (2015).
- [125] C. Y. Wang, T. Herr, P. Del’Haye, A. Schliesser, J. Hofer, R. Holzwarth, T. W. Hänsch, N. Picqué, and T. J. Kippenberg, *Nat. Commun.* **4**, 1345 (2013).
- [126] K. Luke, Y. Okawachi, M. R. E. Lamont, A. L. Gaeta, and M. Lipson, *Opt. Lett.* **40**, 4823–4826 (2015).
- [127] A. A. Savchenkov, V. S. Ilchenko, F. D. Teodoro, P. M. Belden, W. T. Lotshaw, A. B. Matsko, and L. Maleki, *Opt. Lett.* **40**, 3468–3471 (2015).
- [128] J. Vanier, *Appl. Phys. B* **81**, 421–442 (2005).
- [129] E. A. Swanson, D. Huang, M. R. Hee, C. P. L. J. G. Fujimoto, and C. A. Puliafito, *Opt. Lett.* **17**, 151–153 (1992).
- [130] T. Bajraszewski, M. Wojtkowski, M. Szkulmowski, A. Szkulmowska, R. Huber, and A. Kowalczyk, *Opt. Express* **16**, 4163–4176 (2008).
- [131] S. Miller, K. Luke, Y. Okawachi, J. Cardenas, A. L. Gaeta, and M. Lipson, *Opt. Express* **22**, 26517–26525 (2014).
- [132] A. B. Matsko, A. A. Savchenkov, and L. Maleki, *Opt. Lett.* **37**, 43–45 (2012).

-
- [133] X. Xue, Y. Xuan, Y. Liu, P.-H. Wang, S. Chen, J. Wang, D. E. Leaird, M. Qi, and A. M. Weiner, *Nat. Photonics* **9**, 594–600 (2015).
- [134] A. A. Savchenkov, A. B. Matsko, W. Liang, V. S. Ilchenko, D. Seidel, and L. Maleki, *Nat. Photonics* **5**, 293–296 (2011).
- [135] K. Y. Yang, K. Beha, D. C. Cole, X. Yi, P. Del’Haye, H. Lee, J. Li, D. Y. Oh, S. A. Diddams, S. B. Papp, and K. J. Vahala, *Nat. Photonics* **10**, 316–320 (2016).
- [136] D. Farnesi, A. Barucci, G. C. Righini, G. N. Conti, and S. Soria, *Opt. Lett.* **40**, 4508–4511 (2015).
- [137] N. Riesen, W. Q. Zhang, and T. M. Monro, *Opt. Lett.* **41**, 1257–1260 (2016).
- [138] I. S. Grudinin, A. B. Matsko, and L. Maleki, *Phys. Rev. Lett.* **102**, 043902 (2009).
- [139] M. Tomes and T. Carmon, *Phys. Rev. Lett.* **102**, 113601 (2009).
- [140] I. S. Grudinin and L. Maleki, *Opt. Lett.* **32**, 166 (2007).
- [141] A. A. Savchenkov, A. B. Matsko, M. Mohageg, and L. Maleki, *Opt. Lett.* **32**, 497–499 (2007).
- [142] S. M. Spillane, T. J. Kippenberg, and K. J. Vahala, *Nature* **415**, 621 (2002).
- [143] B. Min, T. J. Kippenberg, and K. J. Vahala, *Opt. Lett.* **28**, 1507 (2003).
- [144] T. J. Kippenberg, S. M. Spillane, D. K. Armani, and K. J. Vahala, *Opt. Lett.* **29**, 1224–1226 (2004).
- [145] F. Vanier, M. Rochette, N. Godbout, and Y.-A. Peter, *Opt. Lett.* **38**, 4966–4969 (2013).
- [146] B.-B. Li, Y.-F. Xiao, M.-Y. Yan, W. R. Clements, and Q. Gong, *Opt. Lett.* **38**, 1802–1804 (2013).
- [147] W. Liang, V. S. Ilchenko, A. A. Savchenkov, A. B. Matsko, D. Seidel, and L. Maleki, *Phys. Rev. Lett.* **105**, 143903 (2010).
- [148] L. Yang. *Fabrication and characterization of microlasers by the sol-gel method*. PhD thesis, California Institute of Technology, (2005).
- [149] B. E. Little, J.-P. Laine, and H. A. Haus, *J. Light. Technol.* **17**, 704–715 (1999).
- [150] T. J. Kippenberg. *Nonlinear optics in ultra-high-Q whispering-gallery optical microcavities*. PhD thesis, California Institute of Technology, (2004).
- [151] H. A. Haus, *Waves and Fields in Optoelectronics*, Prentice-Hall, Englewood Cliffs, NJ (1984).
- [152] S. Schiller, *Appl. Opt.* **32**, 2181–2185 (1993).

-
- [153] Y. Zhi, J. Valenta, and A. Meldrum, *J. Opt. Soc. Am. B* **30**, 3079–3085 (2013).
- [154] Y. Minowa, Y. Oguni, and M. Ashida, *Opt. Express* **25**, 10449–10455 (2017).
- [155] M. Wang, X. Jin, F. Li, B. Cai, and K. Wang, *Opt. Commun.* **427**, 70–78 (2018).
- [156] A. Meldrum and F. Marsiglio, *Rev. Nanosci. Nanotechnol.* **3**, 193–209 (2014).
- [157] V. B. Braginsky, M. L. Gorodetsky, and V. S. Ilchenko, *Phys. Lett. A* **137**, 393–397 (1989).
- [158] N. Dubreuil, J. C. Knight, D. K. Leventhal, V. Sandoghdar, J. Hare, and V. Lefevre, *Opt. Lett.* **20**, 813–815 (1995).
- [159] G. Griffel, S. Arnold, D. Taskent, A. Serpengüzel, J. Connolly, and N. Morris, *Opt. Lett.* **21**, 695–697 (1996).
- [160] J. C. Knight, G. Cheung, F. Jacques, and T. A. Birks, *Opt. Lett.* **22**, 1129–1131 (1997).
- [161] I. H. Agha, Y. Okawachi, M. A. Foster, J. E. Sharping, and A. L. Gaeta, *Phys. Rev. A* **76**, 043837 (2007).
- [162] J. M. Ward, A. Maimaiti, V. H. Le, and S. Nic Chormaic, *Rev. Sci. Instrum.* **85**, 111501 (2014).
- [163] T. A. Birks and Y. W. Li, *J. Light. Technol.* **10**, 432–438 (1992).
- [164] T. J. Kippenberg, S. M. Spillane, and K. J. Vahala, *Phys. Rev. Lett.* **93**, 083904 (2004).
- [165] Y. Yang, R. Madugani, S. Kasumie, J. M. Ward, and S. Nic Chormaic. *Cavity Ring-Up Spectroscopy for Dissipative and Dispersive Sensing in a Whispering Gallery Mode Resonator*, pages 629–646. Springer International Publishing, Cham, (2018).
- [166] M. L. Gorodetsky and V. S. Ilchenko, *J. Opt. Soc. Am. B* **16**, 147 (1999).
- [167] C.-L. Zou, Y. Yang, C.-H. Dong, Y.-F. Xiao, X.-W. Wu, Z.-F. Han, and G.-C. Guo, *J. Opt. Soc. Am. B* **25**, 1895 (2008).
- [168] T. J. Kippenberg, S. M. Spillane, and K. J. Vahala, *Opt. Lett.* **27**, 1669 (2002).
- [169] K. Srinivasan and O. Painter, *Phys. Rev. A* **75**, 023814 (2007).
- [170] R. Madugani. *Whispering Gallery Mode Microcavities: From Fabrication to Applications*. PhD thesis, National University of Ireland, Cork, (2016).
- [171] R. Madugani, Y. Yang, V. H. Le, J. M. Ward, and S. Nic Chormaic, *IEEE Photonics Technol. Lett.* **28**, 1134–1137 (2016).
- [172] P. Phatharacorn, S. Chiangga, and P. Yupapin, *Appl. Opt.* **55**, 9504–9513 (2016).

- [173] Y. Yang, X. Jiang, S. Kasumie, G. Zhao, L. Xu, J. M. Ward, L. Yang, and S. Nic Chormaic, *Opt. Lett.* **41**, 5266–5269 (2016).
- [174] N. Riesen, W. Q. Zhang, and T. M. Monro, *Opt. Express* **24**, 8832–8847 (2016).
- [175] T. Herr, K. Hartinger, J. Riemensberger, C. Y. Wang, E. Gavartin, R. Holzwarth, M. L. Gorodetsky, and T. J. Kippenberg, *Nat. Photonics* **6**, 480–487 (2012).
- [176] P. Wang, J. Ward, Y. Yang, X. Feng, G. Brambilla, G. Farrell, and S. Nic Chormaic, *Appl. Phys. Lett.* **106**, 061101 (2015).
- [177] S. Kasumie, F. Lei, J. M. Ward, X.-F. Jiang, L. Yang, and S. Nic Chormaic, arXiv e-prints , arXiv:1902.02487 (2019).
- [178] G. Lin, A. Coillet, and Y. K. Chembo, *Adv. Opt. Photonics* **9**, 828–890 (2017).
- [179] O. Boyraz and B. Jalali, *Opt. Express* **12**, 5269–5273 (2004).
- [180] H. Rong, A. Liu, R. Jones, O. Cohen, D. Hak, R. Nicolaescu, A. Fang, and M. Paniccia, *Nature* **433**, 292 (2005).
- [181] J. Li, H. Lee, and K. J. Vahala, *Nat. Commun.* **4**, 2097 (2013).
- [182] J. Li, M.-G. Suh, and K. J. Vahala, *Optica* **4**, 346–348 (2017).
- [183] X.-F. Jiang, Y.-F. Xiao, Q.-F. Yang, L. Shao, W. R. Clements, and Q. Gong, *Appl. Phys. Lett.* **103**, 101102 (2013).
- [184] G. Zhao, Ş. K. Özdemir, T. Wang, L. Xu, E. King, G.-L. Long, and L. Yang, *Sci. Bull.* **62**, 875–878 (2017).
- [185] B.-B. Li, W. R. Clements, X.-C. Yu, K. Shi, Q. Gong, and Y.-F. Xiao, *Proc. Natl. Acad. Sci. U.S.A* **111**, 14657–14662 (2014).
- [186] Y. Chen, Z.-H. Zhou, C.-L. Zou, Z. Shen, G.-C. Guo, and C.-H. Dong, *Opt. Express* **25**, 16879–16887 (2017).
- [187] X. Yang, Ş. K. Özdemir, B. Peng, H. Yilmaz, F.-C. Lei, G.-L. Long, and L. Yang, *Opt. Express* **23**, 29573–29583 (2015).
- [188] Y. H. Wen, O. Kuzucu, M. Fridman, A. L. Gaeta, L.-W. Luo, and M. Lipson, *Phys. Rev. Lett.* **108**, 223907 (2012).
- [189] T. J. Kippenberg, S. M. Spillane, B. Min, and K. J. Vahala, *IEEE J. Sel. Top. Quantum Electron.* **10**, 1219–1228 (2004).
- [190] H. Rong, S. Xu, O. Cohen, O. Raday, M. Lee, V. Sih, and M. Paniccia, *Nat. Photonics* **2**, 170 (2008).
- [191] G. Lin, S. Diallo, K. Saleh, R. Martinenghi, J.-C. Beugnot, T. Sylvestre, and Y. K. Chembo, *Appl. Phys. Lett.* **105**, 231103 (2014).

-
- [192] L. Ge, D. Liu, A. Cerjan, S. Rotter, H. Cao, S. G. Johnson, H. E. Türeci, and A. D. Stone, *Opt. Express* **24**, 41–54 (2016).
- [193] H. E. M. Leymann, D. Vorberg, T. Lettau, C. Hopfmann, C. Schneider, M. Kamp, S. Höfling, R. Ketzmerick, J. Wiersig, S. Reitzenstein, et al., *Phys. Rev. X* **7**, 021045 (2017).
- [194] J. Ward and O. Benson, *Laser Photon. Rev.* **5**, 553–570 (2011).
- [195] J. T. Verdeyen, *Laser Electronics*, Prentice-Hall, Englewood Cliffs, NJ (1989).
- [196] D. Hollenbeck and C. D. Cantrell, *J. Opt. Soc. Am. B* **19**, 2886 (2002).
- [197] K. Uchinokura, T. Sekine, and E. Matsuura, *Solid State Commun.* **11**, 47–49 (1972).
- [198] P. J. Colwell and M. V. Klein, *Phys. Rev. B* **6**, 498–515 (1972).
- [199] A. B. Matsko, A. A. Savchenkov, R. J. Letargat, V. S. Ilchenko, and L. Maleki, *J. Opt. B: Quantum and Semiclass. Opt.* **5**, 272 (2003).
- [200] R. M. J. Murphy, F. Lei, J. M. Ward, Y. Yang, and S. Nic Chormaic, *Opt. Express* **25**, 13101–13106 (2017).
- [201] D. Farnesi, F. Cosi, C. Trono, G. C. Righini, G. N. Conti, and S. Soria, *Opt. Lett.* **39**, 5993–5996 (2014).
- [202] O. Lux, S. Sarang, O. Kitzler, D. J. Spence, and R. P. Mildren, *Optica* **3**, 876–881 (2016).
- [203] R. H. Stolen, C. Lee, and R. K. Jain, *J. Opt. Soc. Am. B* **1**, 652–657 (1984).
- [204] R. Suzuki, A. Kubota, A. Hori, S. Fujii, and T. Tanabe, *J. Opt. Soc. Am. B* **35**, 933 (2018).
- [205] Y. Okawachi, M. Yu, V. Venkataraman, P. M. Latawiec, A. G. Griffith, M. Lipson, M. Lončar, and A. L. Gaeta, *Opt. Lett.* **42**, 2786–2789 (2017).
- [206] T. Kato, A. Hori, R. Suzuki, S. Fujii, T. Kobatake, and T. Tanabe, *Opt. Express* **25**, 857–866 (2017).
- [207] A. V. Cherenkov, N. M. Kondratiev, V. E. Lobanov, A. E. Shitikov, D. V. Skryabin, and M. L. Gorodetsky, *Opt. Express* **25**, 31148–31158 (2017).
- [208] G. Lin and Y. K. Chembo, *Opt. Lett.* **41**, 3718–3721 (2016).
- [209] T. Herr, V. Brasch, J. D. Jost, C. Y. Wang, N. M. Kondratiev, M. L. Gorodetsky, and T. J. Kippenberg, *Nat. Photonics* **8**, 145 (2014).
- [210] M. Karpov, H. Guo, A. Kordts, V. Brasch, M. H. P. Pfeiffer, M. Zervas, M. Geiselmann, and T. J. Kippenberg, *Phys. Rev. Lett.* **116**, 103902 (2016).

- [211] Q.-F. Yang, X. Yi, K. Y. Yang, and K. J. Vahala, *Nat. Phys.* **13**, 53 (2017).
- [212] S. V. Zhukovsky, D. N. Chigrin, A. V. Lavrinenko, and J. Kroha, *Phys. Rev. Lett.* **99**, 073902 (2007).
- [213] F. Lei, Y. Yang, J. W. M, and S. Nic Chormaic, *Opt. Express* **25**, 24679–24689 (2017).
- [214] L. Liu, R. Kumar, K. Huybrechts, T. Spuesens, G. Roelkens, E.-J. Geluk, V. T. De, P. Regreny, T. D. Van, R. Baets, et al., *Nat. Photonics* **4**, 182 (2010).